Characterisation and Optimisation of Electrochemically Addressable Templated Polyaniline Structures

by

Brian Gorey B.Sc.

Thesis Submitted for the Degree of Doctor of Philosophy

Supervisors:

Prof. Malcolm Smyth

Dr. Aoife Morrin

&

Dr. Blánaid White

Dublin City University **June 2014**

Declaration:

I hereby certify that this material, which I now submit for assessment on the programme of study leading to the award of PhD, is entirely my own work, that I have exercised reasonable care to ensure that the work is original, and does not to the best of my knowledge breach any law of copyright, and has not been taken from the work of others save and to the extent that such work has been cited and acknowledged within the text of my work.

Signed: _____

(Candidate) ID No.: _____

Date: _____

TABLE OF CONTENTS

Chapter 4

Chemical Polymerisation of Homogenous 3D Ordered Conducting Polymer-Polystyrene Opal Structures in μfluidic Channels

Chapter 5

Controllable Hydrophobicity of PANI Films through Dopant Variation

Chapter 6

Conclusions & Future Work

Abstract

The application of intrinsically conducting polymers (ICPs) for lab-on-chip applications has shown recent success with many research groups reporting novel methods to incorporate and control ICP materials in lab-on-chip platforms. Chemical and electrochemical polymerisation have been used to successfully incorporate ICP materials within microfluidic platforms. However, fabrication of 3D ordered flow-through ICP structures has remained a limitation in this research area to date. This work describes how fabricating a reproducible ICP templating method within the confines of a microfluidic channel consisting of a polystyrene (PS) sphere colloidal crystal (CC) provides a viable solution to this issue. The capillary force packing method developed as part of this thesis offers for the first time a quick and reliable method for the uniform fabrication of unimodal and bimodal CC templates in channel. This is in contrast to other methods such as drop casting, spin coating and dip-drawing which were designed for CC fabrication on planar substrates. Here, 3D ordered CC structures were fabricated exclusively within the μchannel which were ordered along the length, width and depth of the cuboid channel and CC thickness was dictated solely by μchannel depth. This is in contrast to other CC fabrication methods were volume fraction ($VF_{S/L}$) dictates CC thickness.

Subsequently, the CCs were utilised to template ICP materials, namely polyaniline (PANI), in a microfluidic channel, where PANI was grown via electrochemical polymerisation. It was shown that control of the electrochemical polymerisation time was critical not only to the depth of the resulting inverse opal PANI, but also to the intrinsic morphology and flow-through nature of the material. This research demonstrated the fabrication of significantly deeper PANI inverse opal structures

than had been previously reported, due to the new CC templating method employed which could be achieve over a wide range of channel depths (*e.g.* 50 – 180 µm).

Although, this increased channel depth resulted in an inherent inhomogeneity through the depth of the final electrochemically polymerised inverse opal structure due to a current density gradient. To overcome this inhomogenity, an investigation of chemical polymerisation of PANI was undertaken. Prior to CC template formation, aniline monomer was adsorbed onto the PS spheres in solution and subsequently packed in channel. After CC formation of aniline coated PS spheres, chemical polymerisation of the surface-confined aniline was carried out and templated PANI/PS opal structures were achieved. This chemical polymerisation method resulted in a 3D ordered, flow-through PANI/PS opal structures with homogeneous PANI coverage housed within a sealed microfluidic channel. By incorporation of a working electrode along the µchannel, the PANI structure was also electrochemically addressable maintaining the potential for lab-on-chip applications such sensing or separation.

Finally the effect of dopant type on hydrophobicity of PANI films was investigated. Fabrication of PANI films was achieved on gold-sputtered working electrodes using HCl or Sodium dodecyl sulphate (SDS) as dopant. The PANI films were characterised by comparison of their water contact angle (WCA), morphology and surface roughness. It was found that SDS-doped PANI films displayed an ultra-hydrophobic WCA when doped, which upon dedoping became hydrophilic. In contrast, HCl-doped PANI films displayed hydrophilic surface chemistry with little variation upon doping/dedoping. When comparing surface roughness, SDS-doped PANI films displayed an order of magnitude higher roughness to that of the HCl-doped films, likely due to the soft templating effect of SDS during polymerisation.

In summary this thesis presents new research into ICP structures that can be utilised to develop new applications in miniaturised platforms such as lab-on-chip. The benefits of the methods developed are the flow through nature and electrochemical addressability of the final ICP materials. In conjunction the templating method developed in this thesis offers a fabrication route for homogeneous 3D ordered ICP materials which are reproducibly templated in channel. The CC fabricated in this thesis offer a unique and versatile template for microfluidic applications where increased order or surface area is a requirement such as sensing and separation.

Abbreviations:

2D	two-dimensionally
3D	three-dimensionally
3-DOM	three-dimensionally ordered macro-porous
AA	amino acid
Ag/AgCl	silver/silverchloride electrode
AMP	adenosine monophosphate
APS	ammonium persulfate
APTS	8-amino-1,3,6-pyrenetrisulphonic acid
ATP	adenosine triphosphate
bCC	binary colloidal crystal
BSA	bovine serum albumin
CC	colloidal crystal
CP	conducting polymer
CV	cyclic voltammogram
d	particle diameter
D.I.	deionised
DAA	dansyl amino acid
DBS	dodecylbenexe sulfonate

DBSA	dodecylbenzensulfonic acid
DCM	dichloromethane
DDS	drug delivery systems
D_L	diameter of macro-spheres
D_S	diameter of nano-spheres
$D_{S/L}$	diameter size ratio macro/nano-sphere
EB	emeraldine base
EICSA	evaporation-induced co-operative hierarchical self-assembly
EM	emeraldine
ES	emeraldine salt
fcc	face centred cubic
H_2SO_4	sulphuric acid
HCl	hydrochloric acid
$HClO_4$	perchloric acid
hcp	hexagonal close packing
HCSA	(+)-cam-phor-10-sulfonic acid
HF	hydrofluoric acid
ICP	intrinsically conducting polymer
i_p	peak current

ITO	indium tin oxide
j_e	evaporation flux
j_p	particle flux
j_w	water flux
k	number of layers
L	macro-sized spheres
LB	Langmuir-blodgett
LB	leucoemeraldine base
LOC	lab-on-chip
LS	large sphere to small sphere number
LS_n	macro/nano-sphere number ratio
NaDBS	sodium dodecylbenzene sulfonate
n-doped	negatively doped
OSPPY	over oxidised sulfonated polypyrrole
OSPPY	overoxidised sulfonated PPY
PANI	polyaniline
PB	pernigraniline base
PDMS	polydimethysiloxane
p-doped	positively doped

PFOS	perfluorootanesulfonate
PFSEA	perfluorosebacic acid
PMPY	poly(N-methylpyrrole)
PPY	polypyrrole
PS	polystyrene
PSf	polysulfonate
Pt	platinum electrode
PT	polythionphene
PVDF	polyvinilidene fluride
RVC	reticulated vitreous carbon
S	nano-sized sphere
SA	salicylic acid
SDS	sodium dodecyl sulfate
SEM	scanning electron microscopy
SSA	sulfosalicylic acid
t_{60}	60 s after water drop placement
TEOS	tetraethyl orthosilicate
TLC	thin layer chromatography
t_o	time zero

uCC	unimodal colloidal crystal
UV	ultra violet
VF	volume fraction
$VF_{S/L}$	volume fraction macro/nano-sphere % w/v
Vis	visible
WCA	water contact angle
WE	working electrode
β	ratio between velocity of a particle in solution and fluid velocity
Γ’	water volume flux between particles

Acknowledgments:

Firstly I would like to thank my supervisors Dr. Aoife Morrin, Dr. Blanaid White and Prof. Malcolm Smyth for the support, encouragement and guidance that they have given me throughout my project and for the many opportunities they have afforded me.

Secondly I would like to thank the DCU Technical Staff, who were always available to help. A special thank you to Veronica Dobbyn and Dr. Brendan Twamley for the support given and time spent passing on invaluable SEM knowledge.

To Aoife, Nicky and all of the members of the Sensors and Separations group who have passed through during my time and helped me on my way, thank you.

I would also like to thank my Mam and Dad, Rachel and Kevin who were always incredibly supportive and encouraging and Stephen for his computer knowledge which has got me out of more than one bind. Finally, thank you Lisa for your support and patience.

Dedication:

For my parents Breda and Joe

Chapter 1

Towards Lab-On-Chip Applications of Intrinsically Conducting Polymers

1.1 Introduction

In recent times interest in intrinsically conducting polymers (ICPs) has grown due to the demonstrable use of ICPs in a broad range of analytical applications. ICPs uniquely display the electrical, magnetic and optical properties associated with metals [1-3] as well as the processability of polymers. These highly desirable properties have resulted in ICP application in numerous fields such as sensing [4], separations including extractions [5] and controlled drug release [6]. Examples of common ICPs include polypyrrole (PPY) polythiophene (PT) and polyaniline (PANI). PANI and PPY have seen more widespread use in recent times due to easily controlled doping/dedoping, processability, pH sensitivity of PANI and the stability of PPY.

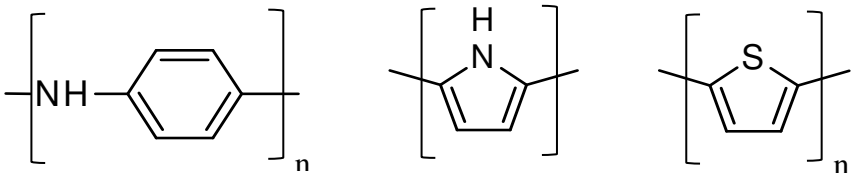

A) PANI B) PPY C) PT

Figure 1.1: Chemical structures of PANI, PPY and PT.

The conjugated backbone of these polymers is what affords them high conductivity. Conductivity is highest along the backbone due to $\pi - \pi$ overlap between monomer units [7]. Broadly speaking, conducting polymers can be separated into two types, those with a degenerate ground state, *e.g.* polyacetylene (PA), where the double and single bonds are interchangeable with no change in energy [8] and those in which the ground state is non-degenerate, *e.g.* PANI. The doping process of PANI results in either the benzoid (lower energy form) or the quinoid (higher energy form). When electrons are removed from the PANI backbone by chemical or electrochemical

oxidations, cation radicals are produced, called polarons. Charged carriers, X^-, are induced close to the polymer chains to counteract the charge on the polymer backbone. The doping mechanism of PANI is shown in Figure 1.2. The Emeraldine Base (EB) form of PANI is doped using an acid to produce Emeraldine Salt (ES). If, for example, HCl is used, the Cl^- ion is the dopant which is incorporated along the polymer backbone as illustrated by X^- in Figure 1.2.

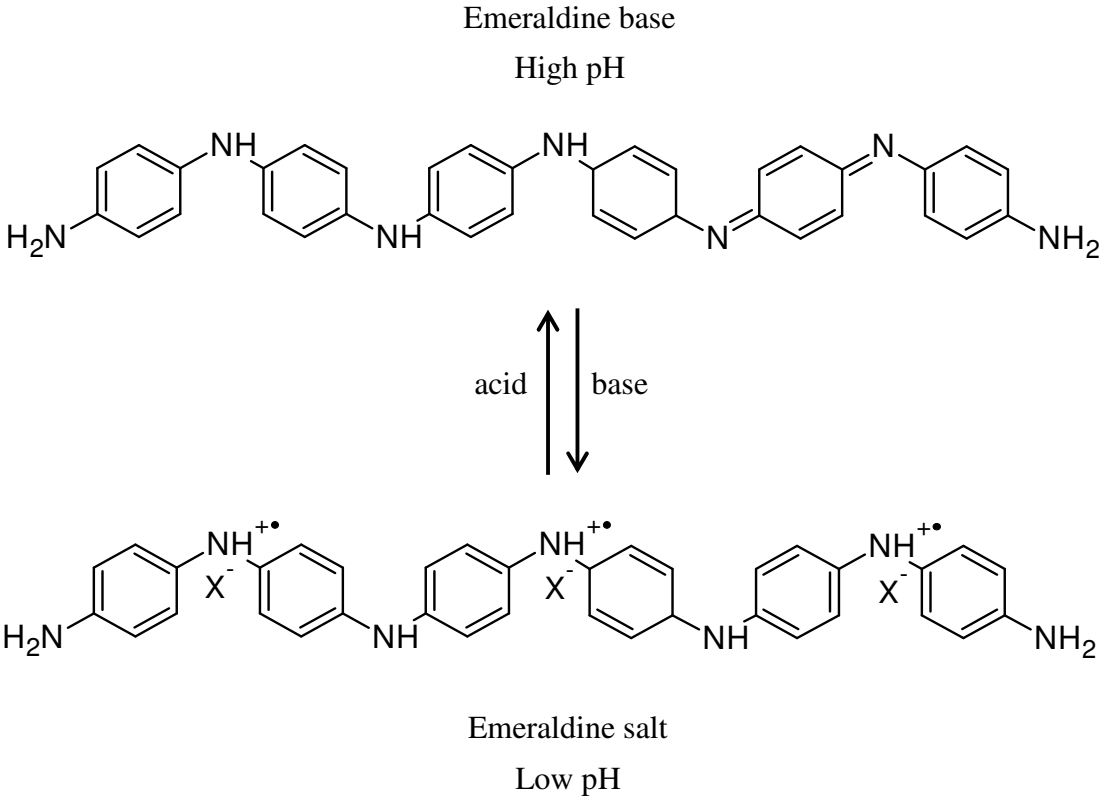

Figure 1.2: Schematic diagram of the doping mechanism of PANI in the Emeraldine oxidation state. At a low/acidic pH, ES is formed. At higher/basic pH, EB is formed.

Leucoemeraldine Base

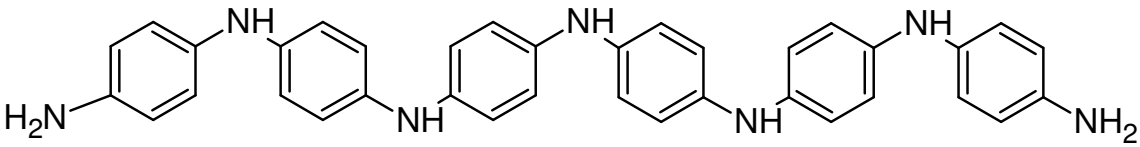

Emeraldine Base

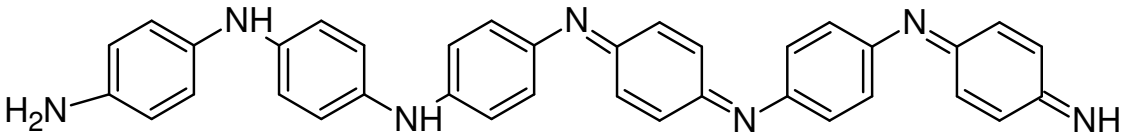

Pernigraniline Base

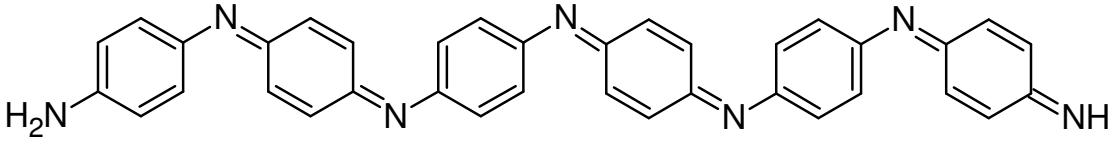

Figure 1.3: Schematic diagram of base oxidation states of polyaniline.

ICPs can exist in a range of oxidised forms, *e.g.* PANI exists in three oxidation states Leucoemeraldine, Emeraldine and Pernigraniline as shown in Figure 1.3. Emeraldine Base is the most useful form of PANI due to its high stability at room temperature and the fact that, upon doping with acid, the resulting ES is highly conducting. Leucoemeraldine and Pernigraniline are poor conductors, even when doped with an acid. The salt/base forms of each oxidation state can be achieved through variations in pH, Figure 1.2 [9].

1.2 Applications of ICPs

The combination of traditional polymer properties and electrically conductive properties [10] make ICP materials applicable in many areas of research, including analytical applications such as sensing [3, 11] and separations [12-14], energy storage [15-17] and drug delivery systems (DDS) [18-21]. Sensors and control release applications will be discussed before a detailed literature review of separation applications is explored.

1.2.1 Sensors

ICP sensing materials have seen extensive research with applications in areas such as: chemical sensing such as detection of ammonia using PANI films [22-24], optical sensing due to optical switching of PANI films in response to alcohol [4] and optical switching of PPY films in response to ammonia [25] and bio-sensing which can incorporate enzymes into ICP films such as glucose oxidase in PPY [26]. Chemical sensing includes gas [27] and pH sensors which are based on the doping/dedoping of polymer films [28]. ICPs are also often used in bio-sensing, which is based on the exploitation of a biochemical reaction. For example, glucose concentration can be monitored via its catalytic breakdown by glucose oxidase enzyme. Glucose can be broken down into gluconic acid and hydrogen peroxide by this oxidase enzyme. The production of these species can potentially be monitored using an ICP that has been tailored to be catalytic towards hydrogen peroxide [29]. Depending on the ICP material being used, this can be done optically or electrochemically. Other biosensor applications include cholesterol [30, 31] and hydrogen peroxide [32, 33] detection. Biosensors for food and environmental monitoring are also numerous with reviews available detailing applications [34-37].

A recent example published by Zhang *et al.* [38] demonstrated, through measured increase/decreases in resistance, that electro-spun PANI fibres doped with (+)-camphor-10-sulfonic acid (HCSA) were successful in gas sensing applications. Doped PANI fibres displayed sensitivity to ammonia between 10 – 700 ppm with quick response time (45 s). The fibres, upon purging with nitrogen, were shown to recover quickly. The undoped PANI fibres were also tested for their response to nitrogen dioxide. Again the fibres showed a rapid response (50 s) and recovery (70 s) within a 1 – 50 ppm range. Palod *et al.* [39] reported the electrochemical growth of

PPY nanotubes for an enzymatic glucose bio-sensing application. They [39] incorporated the enzyme (glucose oxidase) into the porous PPY film by physical adsorption allowing oxidisation of glucose to gluconic acid, with hydrogen peroxide (a by-product of the reaction) decomposition giving a current proportional to the glucose concentration. Polymerisation time, and hence polymer thickness, was varied between 10 – 100 s with 40 s observed to be optimum polymerisation time. 40 s was optimum due to deposition of PPY with discrete pores separating nanotubes on the working electrode surface. Longer polymerisation times resulted in lower porosity, reducing glucose oxidase adsorption. The enzyme immobilisation of glucose oxidase via physical adsorption resulted in an operating range between 0.25 – 20 mM with the lowest detection limit of 0.25 mM glucose recorded at the optimum polymerisation time of 40 s. ICP materials were also used by Tavoli [25] for an optical gas sensor based on ammonia vapour sensing utilising nano-structured dye-doped PPY films. The PPY film was doped with eriochrome cyanine R (ERC). With the addition of the ERC dye a change in optical absorption in the presence of ammonia was used to quantify ammonia concentrations. The PPY-ERC gas sensor had low detection limits, 5 µg/L, over a range of concentrations between 15 – 260 µg/L and fast response time (50 s).

1.2.2 Controlled release

ICPs can undergo highly controllable and reversible redox reactions. With controlled changes in the redox state of an ICP, changes in charge, conductivity and volume of the polymer can occur. Therefore through variation in the polymer state, drug release from ICPs is possible. However, before drug release, incorporation of drug molecules into the material must be achieved. Incorporation of drug molecules can occur: i) during the polymer synthesis [40] or ii) after polymer synthesis [41].

Types of drugs which can be incorporated include anionic such as naproxen, salicylate and tosylate [42, 43]. Anionic drug molecules can be incorporated as dopants upon the formation of polarons along the polymer backbone, where their incorporation will balance the overall charge in the polymer network. These can then be released upon dedoping. Cationic drugs such as chlorpromazin have the opposite charge associated, which requires alternative optimisation of the polymer system before incorporation can occur [41]. In this case, incorporation of large negatively charged dopants during polymerisation is undertaken, so that the charge will be balanced by incorporation of the positively charged cationic drugs. The large dopants become immobilised in the polymer network and are not expelled upon dedoping. The cationic drugs can then be incorporated successfully [41] to balance the remaining charge, through electrostatic forces [44]. Finally, there is the incorporation of neutral drugs which can be achieved through encapsulation [45] and binding [46]. Controlled drug release can be achieved through methods including electrostatic interactions [47] and electrochemical release [6, 48] from a polymer network as shown by Svirskis *et al.* who demonstrated the controlled release of Risperidone from a PPY film through application of an electrochemical potential [49].

Early work by Miller *et al.* [50] showed one of the first examples of drug loading and delivery using an ICP. Here PPY was observed to incorporate dopamine upon reduction at -0.4 V vs. saturated calomel electrode (SCE) in an aqueous solution containing dopamine. Following switching of the applied potential to +0.5 V vs. SCE the bound dopamine could then be released. This early work showed the huge potential for ICP controlled release. More recently, PPY scaffolds with high surface area and an inverse opal structure were fabricated with tuneable drug delivery by Sharma *et al.* [51] Over a period of 1 hour the inverse opal PPY films released 40%

more drug when electrically stimulated (169 µg) compared with no electrical stimulation (119.8 µg). Of importance too, these concentrations of drugs released from the structured film were approx. four times higher than the corresponding bulk films, where only 42.5 µg was released when electrically stimulated and 31.3 µg was released without electrical stimulation. Similarly Alizadeh *et al.* [52] demonstrated a nanostructured PPY film for drug loading and release, where drug loading of 24.5 mg/g was reported for methotrexate. PPY films were first pre-electrochemically polymerised in HCl before polymerisation in methotrexate and cetylpyridinium; in this instance the cationic cetylpyridinium interacted with the anionic methotrexate to increase drug doping. After polymerisation the PPY films were doped with methotrexate and cetylpyridinium, with the films then dedoped to create cavities for drug loading and release studies. Rate of release was increased through application of more negative potentials, *e.g.* -0.9 V vs. Ag/Cl and higher temperatures.

1.2.3 Separations

Over the past two decades, extensive work has been achieved utilising ICP materials as a stationary phase material. ICPs are potentially useful as stationary phases due to their anion and cation, doping/dedoping (or exchange) ability, controllable permeability, high surface areas, processability, low cost and redox active properties which could allow for electro-modulated control over separations [53]. Types of separations include liquid chromatography, gas separations, ultrafiltration (UF) and micro-extraction utilising ICPs.

1.2.3.1 Liquid chromatography

Early work in the field by Ge *et al.* [12] detailed the use of PPY coated reticulated vitreous carbon (RVC) as a stationary phase. PPY was electrochemically grown onto RVC at a fixed potential and the PPY coated RVC particles were subsequently

packed in a column and the chromatographic performance investigated. Separation and retention of polar and non-polar compounds was achieved on the PPY coated stationary phase with higher retention for non-polar anthracene noted in comparison to commercially available columns. This was attributed to π-π electronic interaction between PPY and anthracene. Similarly the retention of acidic samples was higher than for basic samples reported due to increased ion exchange interactions for acid samples. An example of the HPLC column used by Ge *et al.* is shown in Figure 1.4. The experimental set up is complex with a multi-step process to coat the stationary phase with PPY and subsequently pack the particles to create a homogeneous column bed whilst ensuring a consistent electrochemical connection.

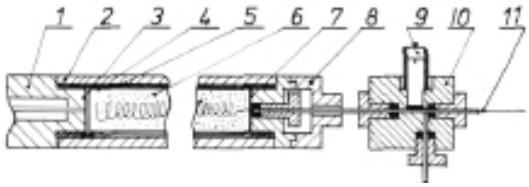

Figure 1.4: Schematic of the HPLC column used by Ge et al. for EMLC where 1) stainless steel fitting, 2) Teflon column tube, 3) filter, 4) membrane, 5) counter electrode (carbon fibre), 6) conducting stationary phase 7) filter, 8) fitting, 9) reference electrode, 10) Teflon fitting and 11) Tantalum coil reproduced from Reference [12].

In the early 1990s interesting work was reported utilising ICP coatings in particulate-based chromatographic stationary phases. Work by Deinhammer *et al.* [13] using a PPY coated glassy carbon (GC) stationary phase was employed which demonstrated the potential of ICPs in separations. In this work a 0.03 µm thick PPY film was electrochemically polymerised onto a GC stationary phase. Through variation in the applied potential the neutral or oxidised form of the polymer could be achieved. In this work more highly charged (triply charged) adenosine triphosphate (ATP) and

less highly charged (singly charged) adenosine monophosphate (AMP) were shown to compete for binding sites on the PPY coated stationary phase at more positive potentials. Upon moving to more negative potentials the retention of AMP and ATP could be controlled by gradually reducing the number of exchange sites through application of a voltage step. This voltage step resulted in elution of the singly charged AMP first with the triply charged ATP eluting last. An example of the chromatograms achieved through application of a voltage step in this work is shown in Figure 1.5. It was also noted that with more negative initial applied potentials, retention was significantly reduced of both AMP and ATP due to a reduction in exchange sites for binding. Figure 1.6 details the custom housing used by Deinhammer *et al.* during this work. Incorporation of PPY coated particles within the custom housing was again multi-step and time-consuming to ensure a consistent connection to the electrodes as well as homogeneous coverage of PPY during polymerisation.

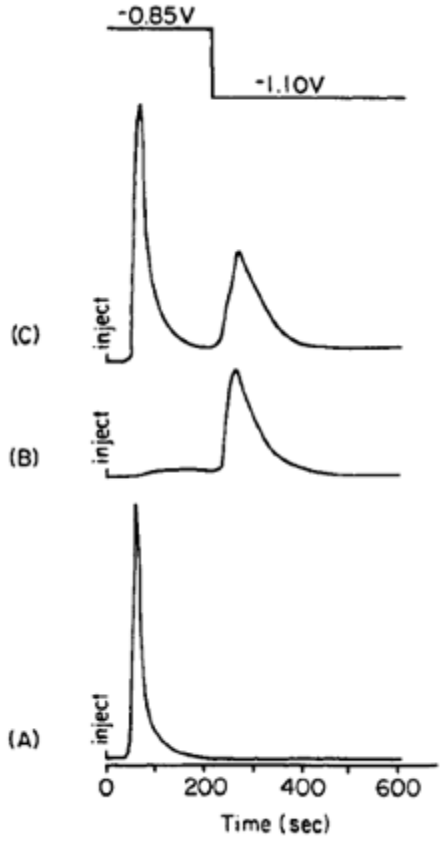

Figure 1.5: Chromatograms of AMP and ATP obtained by applying a voltage step to polypyrrole-coated stationary phase at an initial applied voltage of -0.85 V: (A) AMP; (B) ATP; (C) AMP + ATP. The voltage was stepped to -1.10 V 220s after injection. Injection volumes equalled 0.5 μL of a 10 mM solution for each chromatogram. The mobile phase electrolyte was 10 mM $LiClO_4$ with UV-Vis detection, reproduced from [13].

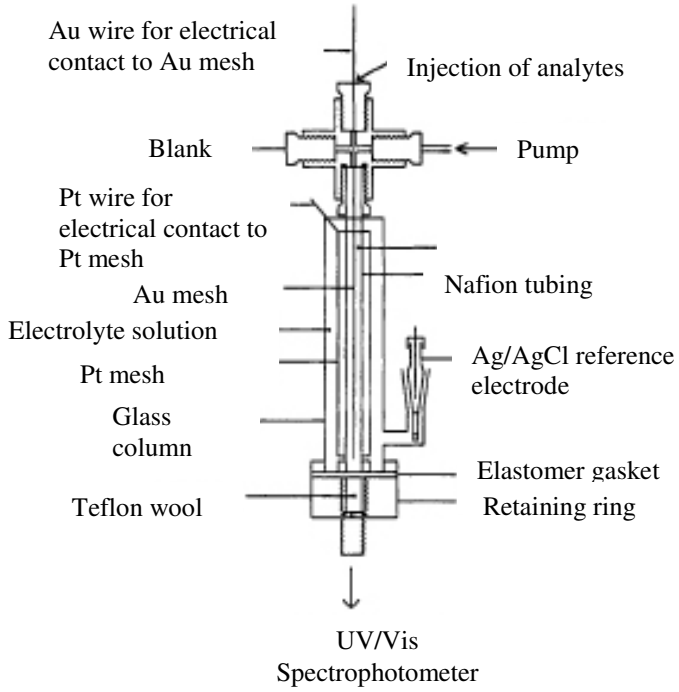

Figure 1.6: Schematic of custom HPLC column housing used by Deinhammer et al. during EMLC reproduced from reference [13].

Porters group [53] reported the formation of a stationary phase through electro-polymerisation of a thin film of PPY onto glassy carbon particles, with an Ag wire used as reference electrode. The switching potential of PPY between its reduced and oxidised form through changes in E_{app} resulted in the improved separation of dansyl amino acids (DAA). Here the ICP coated stationary phase was housed within Nafion tubing in custom column housing.

Teasdale subsequently reported the study of interactions and retention of amino acids on PANI, in thin film format. Preparation of the PANI films was achieved through electrochemical deposition. Retention of amino acids (AA) and change in retention with changes in the pH of the mobile phase was investigated for both PANI and PPY using inverse thin layer chromatography (TLC) [54]. Strong anion exchange

interactions were observed for PANI as the negatively charged AAs were retained most strongly on the stationary phase. The effect of mobile phase pH was also studied. At low pH, acidic AAs had higher retention due to higher anion exchange interactions. Upon moving to pH 5.6, higher retention was still noted for acidic AA with an overall increase in all AA retentions. Finally at pH 7.5 - 9.1, retention of all AAs reduced due to a reduction in anion exchange interactions of the PANI structure. It was concluded in this paper that both PANI and PPY were found to behave predominantly as anion-exchange materials. Polyaniline was also found to interact with neutral polar species more than non-polar or positively charged species.

The separation of bioactive peptides was subsequently demonstrated by Bossi *et al.* [55]. In this work separation was achieved in a fused-silica capillary electrophoresis column. The walls of the column were modified with a thin film of PANI through chemical polymerisation. Under acidic conditions hydrophobic interactions between the ICP film and three peptides m-enkephalin, I-enkephalin and β-casomorphin resulted in more controlled separations in comparison to silica based capillaries and traditional capillary zone electrophoresis where separation was difficult due to similarity between the molecules. In unmodified silica columns two of the peptides, I-enkephalin and β-casomorphin co-eluted in a single peak, the PANI modified column resulted in increased separation control. Importantly the PANI coatings also showed good stability over 50 – 70 runs. Similarly Robb *et al.* [56] fabricated PANI coatings for fused-silica. The PANI coating was a complex fabricated with polyacrylic acid and methacrylate to form a double-strand polymer film. The electro-active and hydrophobic characteristics of the ICP film enhanced the separation of

theobromine, theophylline and caffeine. The PANI double-strand polymer reduced the electro-osmotic flow resulting in increased resolution during analyte separation.

In general, the redox and acid/base properties of ICPs have shown some advantages in separations, with changes in E_{app} and pH allowing for more control over separations. Manipulations in retention due to E_{app} and pH variations of both acidic and basic samples were attributed to increasing and decreasing anion/cation exchange sites of ICP materials. In this way, ICP-coated stationary phases offer advantages over conventional stationary phases which utilise a stationary phase with a fixed composition. In these traditional separations, optimisation during separations is limited to alterations in composition and flow rate of the mobile phase. For this reason, the addition of electro-modulation offers another avenue in optimisation of separations. To date EMLC has not seen widespread use, likely due to the complex experimental set up and the difficulties associated with integration of electrodes within current HPLC columns. Microfluidic platforms could potentially offer a solution to the issues here, offering a novel avenue for integration of electrodes in purpose-built housings. Microfluidic platforms offer increased control by combining the electro-modulated capabilities of ICP materials with the cheap, easily produced custom microfluidic platforms with integrated electrochemical cells [57-59].

Table 1.1: Examples of ICP, polymerisation method and the detection method used in liquid chromatography applications as discussed in Section 1.2.3.1.

Reference	Conducting polymer	Polymerisation method	Detection
Ge et al. [12]	Polypyrrole	Electrochemical	UV-Vis
Deinhammer et al. [13]	Polypyrrole	Electrochemical	UV-Vis
Deinhammer et al. [53]	Polypyrrole	Electrochemical	UV-Vis
Bossi et al. [55]	Polyaniline	Chemical	UV-Vis

1.2.3.2 ICPs in gas separations

The use of ICPs in gas separation applications [60] for separation of gases such as O_2 N_2 and H_2 [61] has been of interest due to the controllable doping/deoping process of ICP polymers which can help control gas separation. It has been reported that through selectively doping with different counter ions it is possible to control the resulting gas permeability [62]. This is as a result of a reduction in free space within the ICP network, therefore a decrease in permeability is noted with an increase in separation. A schematic example of a typical gas separation set up is shown in Figure 1.7 illustrating the membrane and support, vacuum and gas feed.

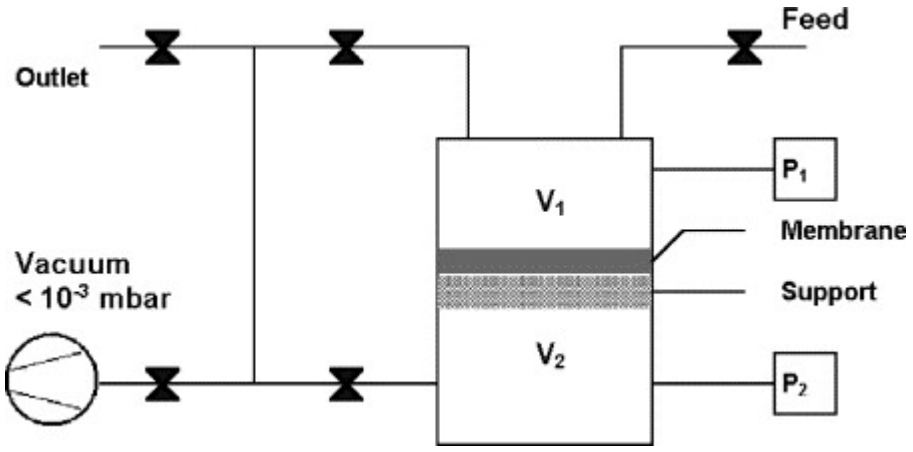

Figure 1.7: Schematic of the gas separation cell used by Illing et al. reproduced from reference [63].

This was shown by Anderson *et al.* [64] where an increase in separation efficiency of PANI films was achieved through doping, dedoping and subsequent selective re-doping of PANI coatings. The redoping of ICP films was achieved by increase/decreasing the concentration of HCl during re-doping. In conjunction with re-doping, dopant size was also investigated and was shown to produce films with different permeability based on dopant size. This unique quality of ICPs has led to controllable gas separations using fully dense ICP films [65, 66]. Selectivity for different gases is based on permeability through a thin ICP film, and is dependent on

the fabrication of fully dense, non-porous ICP films [67, 68]. In essence this limits the use of many ICPs due to their typically fibrillar morphology which results in non-dense films. An example of a dense PANI film is shown in Figure 1.8, which was fabricated through solvent casting of Emeraldine Base (EB) suspensions in NMP. Using this film, Illing *et al.* demonstrated separation of O_2 CO_2 N_2 and H_2 through the dense PANI thin film. [63]

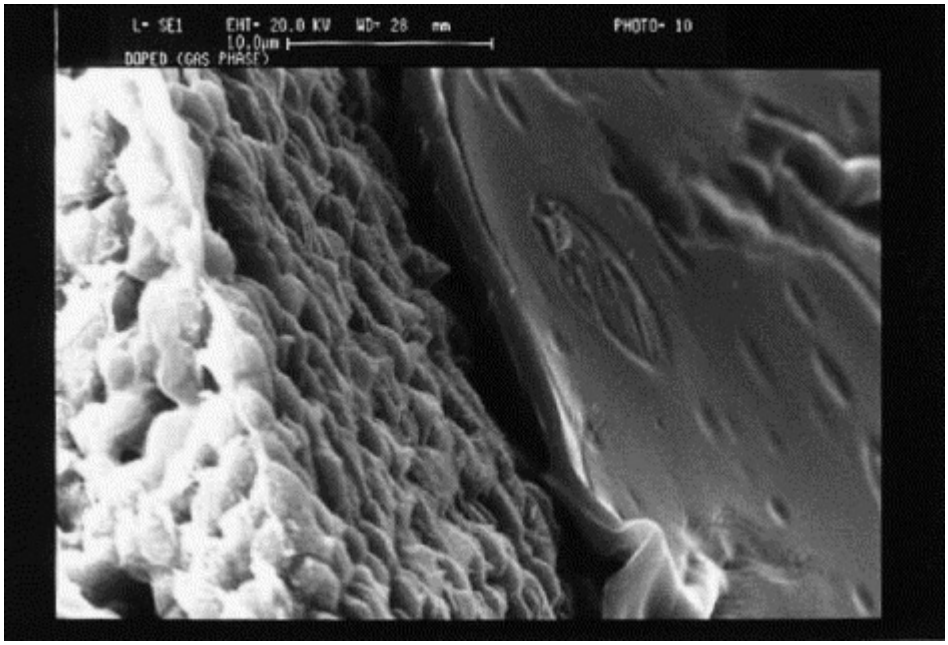

Figure 1.8: SEM image showing a dense, thin film of PANI on a porous PVDF support fabricated by Illing et al. reproduced from reference [63].

It is possible to obtain PANI films with dense morphologies using a number of methods. One example is by dissolution in its EB oxidation state in organic solvent and casting of the solution to remove solvent. Chang *et al.* [61] reported the tailoring of PANI after film formation through doping/de-doping process. N-methyl-pyrrolidine (NMP) solutions of PANI were prepared with constant stirring. The solutions were then cast to form flexible PANI membrane films. It was noted that doping affected the permeability of gases with lower diffusion of gases in doped

films. A summary of the results found by Chang *et al*. are shown in Table 1.2. Doping primarily was shown to decrease diffusivity.

Table 1.2: Summary of gas permeability through doped (HCl) and dedoped PANI films with permeability shown to reduce for doped films, reproduced from[61].

	Permeability (Bar)	
Gas	**Doped**	**Dedoped**
He	0.319	3.66
H_2	0.121	3.14
CO_2	0.0034	0.771
O_2	0.0016	0.135
NH_2	0.005	0.01
CH_4	0.005	-

It was observed that as the permeability of membranes increased their ability to separate gases efficiently was reduced [61, 62]. Extensive applications of gas separation using PANI films are available in the literature. [69-71]

In contrast to PANI film fabrication, polypyrrole (PPY) is insoluble in most organic solvents; therefore the preparation of PPY membranes must be achieved through electrochemical polymerisation onto an electrode or through growth of the polymer chemically onto an existing membrane substrate. Due to this the use of PPY membranes for gas separation has been limited. Nonetheless, deposition of a thin film onto an alumina support membrane was reported by Liang and Martin, [72] although the porosity of the doped film was high which reduced selectivity. Subsequently, the preparation of poly(N-methylpyrrole) (PMPY) onto an alumina support membrane was achieved, as illustrated in the schematic showing the experimental set-up in Figure 1.9. The porosity was seen to decrease and the

selectivity was shown to increase for the doped polymer films. Selectivity for O_2/N_2 of 8.0 was reported matching poly(p-hydroxystyrene) films.

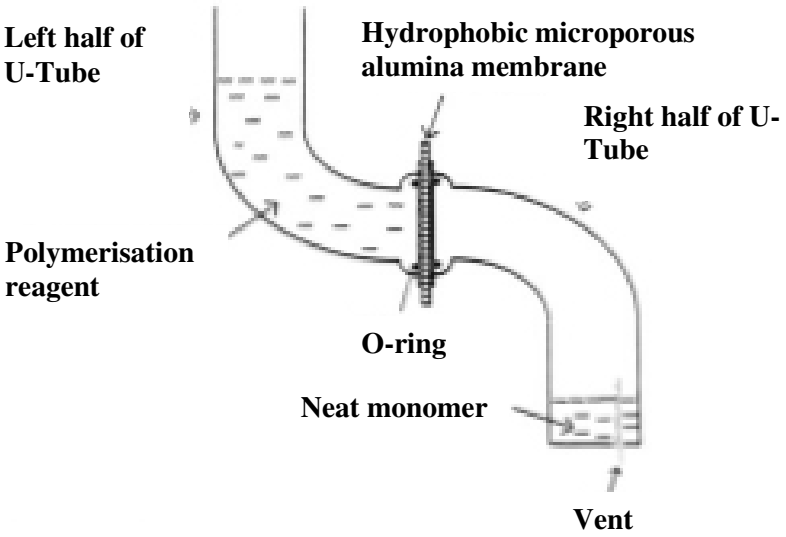

Figure 1.9: Schematic diagram of cell used to conduct interfacial polymerisation of a thin conductive polymer film onto the surface of a microporous support fabricated by Liang et al. reproduced from reference [72].

Parthasarathy *et al.* [73] also demonstrated gas transport in PPY films. Here the undoped polymer was thought to be more desirable due to its combination of high selectivity and relatively quick separation. However, decreased selectivity was attributed to the micro-porous morphology of PPY membranes obtained. When the polymerisation rate was decreased, PPY membranes with more dense morphology were achieved. With the more dense morphology, selectivity coefficients of 18 were obtained for O_2/N_2, which was one of the highest reported. However, a further increase was also achieved for O_2/N_2 giving a selectivity coefficient of 92 for N_2 which was the highest by far reported for polymeric materials at the time.

The insolubility of PPY in many organic solvents has meant the need for novel membrane formation methods. The use of chemical oxidation is widely reported for

PPY membrane formation [74, 75]. While PPY membranes have shown high selectivity in gas separations in the literature, limitations in achieving dense membranes and reliable supports [74] has limited the use and application of PPY membranes. PANI films have seen more interest due to ease of preparation through casting of dense films in appropriate solvents [61] which offers a straightforward fabrication method in comparison to PPY membranes fabrication. However, selectivity for both PANI and PPY is similar throughout the literature, with applications found for both [60, 75-77].

1.2.3.3 ICP's in ultrafiltration (UF)

The unique properties of ICPs such as ease of production, porosity, tuneable hydrophobicity/hydrophilicity and electrochemical control make ICP materials interesting candidates for research as membrane coatings for UF applications [78]. Polysulfone (PSf) membranes are currently used for UF membranes but have limitations including pore-clogging low permeability [77]. The low permeability comes as a result of the hydrophobic nature of UF membranes. The inclusion of ICPs in the formation of PSf UF membranes forming composite membranes has shown increased permeability and a decrease in pore clogging.

The use of PANI in UF membranes was first reported by Guillen [77]. Here the preparation of pure PANI UF membranes was reported for the first time by non-solvent induced phase inversion through chemical oxidative polymerisation. A comparison of the pure PANI to PANI/PSf composites and pure PSf membrane was demonstrated. It was shown that pure PANI membranes achieved an order of magnitude higher water permeability due to higher porosity with similar particle rejection to that of the composite and pure PSf membranes.

Recent research [79, 80] has used bovine serum albumin (BSA) filtration for determining the effectiveness of UF membranes with variation in preparation methods and the ICP used. Examples include composite membranes of PPY and polyvinilidene fluride (PVDF) used as a support [81], fabricated by chemical polymerisation of pyrrole, which displayed higher rejection of BSA from the ICP coated UF membranes - an increase from 75% to 90% over 75 min. The increase in rejection was due to clogging of pores on the surface of the membrane as a result of electrostatic repulsion of the BSA from the membrane surface. In comparison the non-conductive membrane showed rejection increase of 55% to 78% over 75 min. This was attributed to clogging of pores within the membrane as well as on the membrane surface [81]. Similarly, Madaeni *et al.* [79] showed a PPY composite UF membrane again for the removal of protein BSA fabricated by chemical polymerisation. Here, higher rejection and control of separation was achieved utilising the PPY coated UF membrane. The increased activity of the ICP UF membrane was again due to the electrostatic interaction of BSA with the PPY resulting in higher rejection. Fan *et al.* [80] by filtration of aqueous PANI nano-fibres through a PSf membrane achieved an ICP coating on the surface of the UF membrane. The nano-coating of PANI resulted in increased permeability due to the increase in hydrophilicity with no loss in rejection performance. During BSA filtration again the ICP coating of PANI was shown to improve performance due to rejection based on charge.

The addition of ICPs therefore shows an increase in rejection properties through electrostatic repulsion and an increase in hydrophilicity in comparison to commercially available UF membranes. This resulted in less pore clogging within the membrane and in the cases where pore clogging occurs it can be more reversible

due to clogging mainly on the surface of pure ICP and ICP/composite UF membranes rather than within the pore structure as is the case in commercially available membranes. ICP coatings and fabrication of pure ICP UF membranes show significant advantages in UF membrane preparation.

1.2.3.4 Micro-extraction

Micro-extraction is a selective sample purification/separation or detection method. In micro-extraction or solid phase micro-extraction (SPME) methods a fibre is coated with an extracting phase which is utilised to extract a chosen analyte from liquid or gas phase by sorption and desorption [82]. Advantages of micro-extraction over traditional sample preparation methods include: speed and simplicity such as that shown by Liu *et al.* [83] where PPY was electrochemically polymerised onto a Pt wire using a three-electrode electrochemical cell. The Pt wire acted as anode, a stainless steel wire was used as cathode with a saturated calomel electrode (SCE) reference electrode. Electrochemical polymerisation ensured electrochemical addressability of ICP films for micro-extraction applications giving electro-modulated extraction and desorption capabilities [83]. Typically stationary phases of this type are three dimensional electrodes covered with an ICP layer *e.g.* PPY. The potential difference applied can cause the properties to change and therefore the analyte retention capabilities can be manipulated and selectivity controlled [84]. The electrochemical control of the extraction process has been shown to offer increased performance and distinct advantages over neutral separations. Composites employing ICPs are also used in many cases to increase tensile strength and life span of ICPs during micro-extractions [83, 85].

Early work by Wu *et al.* [86] demonstrated the fabrication of high surface area porous PPY and poly-N-phenylpyrrole (PPPY) SPME fibres. The prepared fibre demonstrated controllable interactions with PPPY interacting more strongly with aromatic compounds such as benzene and toluene with PPY films displaying higher sensitivity to polar gaseous compounds. PPY and PPPY were prepared on conducting wires by electrochemical technique as well as on the inner surface of capillary tubes via chemical polymerisation. Wu *et al.* [86] also demonstrated automated in-tube SPME coupled with HPLC with increased sensitivity to naphthalene, diethyl phthalate, dimethyl phthalate and toluene in comparison to a non-coated silica capillary with UV detection utilised.

More recent examples reported the fabrication of over-oxidised PPY films for micro-extraction via electrochemical polymerisation on a Pt wire. Here PPY films were templated with salicylate (SA). SPME of SA resulted in an increase in selectivity through templating [87]. In this instance by controlling E_{app}, the uptake and release of ions could be controlled more selectively with uptake at more positive potentials and release at more negative potentials. At more basic pH, the ionic form of SA was more prominent in solution resulting in increased uptake, but upon moving to lower more acidic pH the ionic form was decreased in solution resulting in lower affinity but increased release. [87] Similarly Sahin *et al.* reported a method for anion and cation extraction using PPy and overoxidised sulfonated PPY (OSPPY). The controlled uptake and release of anions and cations using controlled potentials was examined with the PPY film acting as an anion-exchanger and the OSPPY acting as a cation-exchanger [88]. The preparation of PPY films was again illustrated on a Pt wire through electrochemical deposition. Tap water samples were tested and extraction of anions and cations was achieved.

As detailed above, the ease of fabrication as well as the switchable/tuneable properties of ICP's, in particular PPY, have been shown to be ideal for SPME applications. The properties of ICP's can be manipulated via changes in pH, electrochemical switching and templating to increase porosity/selectivity for chosen analytes. This has resulted in extraction phases with increased selectivity and numerous extraction applications from aromatic compounds to simple anion and cation exchange.

1.2.4 ICPs in microfluidics

The unique attributes of ICP's, namely electrochemical modulation, easily controllable doping/dedoping processes, low cost and processability have fuelled many analytical applications. Moving forward coupling these highly desirable properties with microfluidic platforms is an exciting avenue for future analytical applications. The benefits of microfluidic platforms are uniquely placed to overcome the limitations associated with current methods which include multi-step experimental set-up and integration of electrodes. To overcome these limitations a move to microfluidic housings can be considered. This section will highlight recent literature emerging on ICP integration into lab-on-chip platforms and their applications. The combination of ICP materials and microfluidic platforms is still in its infancy, with optimisation and integration of ICP materials and electrodes an on-going process.

ICP-modified electrodes within microfluidic housings have received attention for sensing and separation applications due to the reduced sample consumption with volume used normally on the scale of nano-litres and increased sensitivity as a result of reduced signal to noise ratios [89, 90]. In a communication by Henderson *et al.* [91] the fabrication and characterisation of patterned chemically polymerised PANI-

modified electrodes within a microfluidic device for electrophoretic separations and detection was discussed. The microchip design was used for the electrophoretic separation of Li^+, Na^+ and K^+ with comparable separation to a conventional C^4D detector for the PANI-modified electrodes. An example of the chromatograms achieved in this work as well as the microfluidic housing utilised are shown in Figure 1.10. Earlier work by Henderson [92] discussed initial steps towards a completely polymeric microfluidic device where chemically polymerised PANI was drop-cast onto an acrylic substrate. The PANI film was then patterned using flash welding and the patterned PANI-modified electrode system was used for electrophoretic separations. 8-amino-1,3,6-pyrenetrisulphonic acid (APTS) labelled sugars glucose, lactose and maltose were successfully separated after 30 s with a comparable electrophoretic separation using Pt electrodes. The work by Henderson *et al.* highlights the potential of PANI-modified electrode material within microfluidic devices.

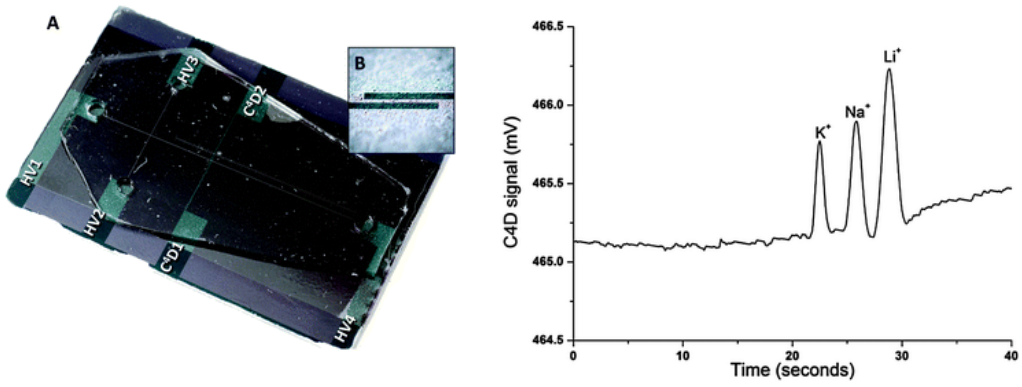

Figure 1.10: Left; photograph of polymeric LOC device. Polymer electrodes were patterned in PANI by laser-welding, where the conducting non-welded areas have kept their green colour. DFR coverage physically isolates the detection electrodes for C^4D with holes to enable direct contact between the PANI HV electrodes and the fluid in the reservoirs. A reversibly bound PDMS substrate contains the microfluidic structure and reservoirs. (B) Close up view of the C^4D electrodes, 200 µm wide with a 100 µm gap. Right; electropherogram of the separation of 100 ppm Li^+, Na^+ and K^+ performed using an electrophoresis chip 45 mM MES/55 mM His as background electrode. Sample was injected for 10 s during application of a potential, reproduced from [91].

Wang *et al.* [93] demonstrated the fabrication of ICP polymer wires of PANI integrated within a microfluidic platform. Here, nano-wires were polymerised over the exposed electrode area (10 x 100 µm) in channel over a 40-minute period. This timescale was a significant reduction in comparison to bulk polymerisation which took 6 h to completely cover the exposed electrode area. After fabrication, the sensing capabilities of the ICP material were investigated. The nano-wires were shown to have rapid response times (several seconds) and high sensitivity to pH change. The nano-wire morphology, fast detection and reduced polymerisation time

were credited to the microfluidic platform employed. The microfluidic housing used is detailed in Figure 1.11 below as well as electrode orientation and schematic of ICP incorporation.

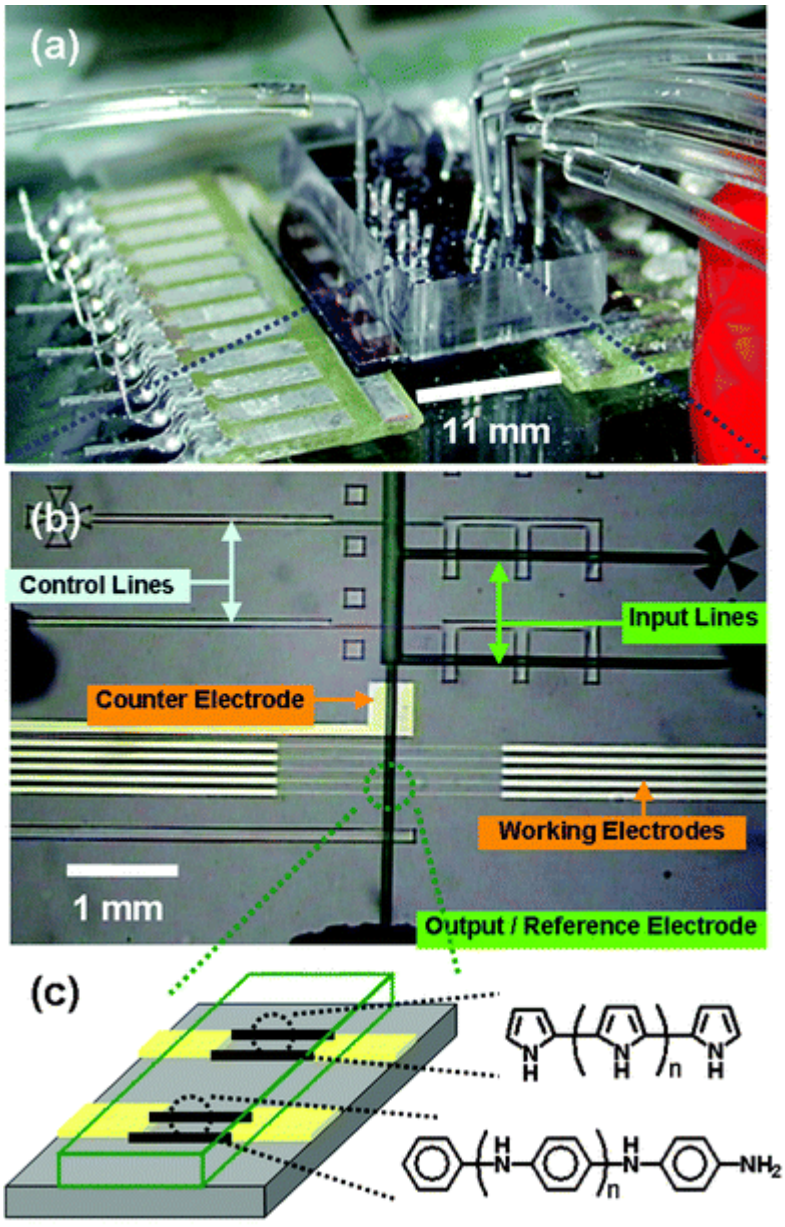

Figure 1.11: A) Actual view of the micro-fabricated and assembled integrated microfluidic device. B) Optical micrograph of the integrated microfluidic device showing microfluidic channels 16 µm high and 100 µm wide. Each of the five pairs of electrode junctions is separated by a 2.0 µm-wide gap; the width and height of each electrode are 10 µm and 50 nm, respectively. C) Schematic illustration of the

electrochemical fabrication of conducting polymer nano-wires (CPNWs) in the microfluidic channel, reproduced from [93].

Florea *et al.* [94] demonstrated a PANI based optical sensor within a micro-capillary housing. The nano-fibres of PANI were shown to operate in a wide range (0.2 – 2000 ppm) for the detection of aqueous ammonia in real time. Very fast response times (less than 5 s) were achieved using the micro-capillary housing. Here, PANI was chemically polymerised to the walls of a transparent capillary column (100 µm internal diameter) housing and was successfully demonstrated as an integrated optical detection method for aqueous ammonia. Figure 1.12 below details a schematic of the experimental set up used by Florea *et al.*

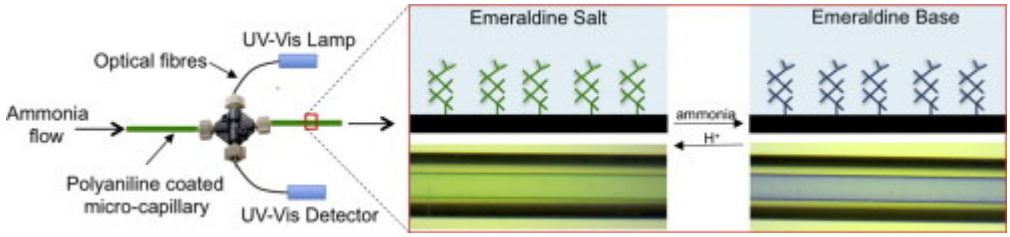

Figure 1.12: Schematic showing the flow of ammonia into the PANI coated micro-capillary and UV-detection upon variation in oxidation state due to dedoping between Emeraldine Salt and Base forms, reproduced from [94].

Similarly, the benefits of microchip analysis incorporating ICP materials were presented by Power *et al*. [57] who demonstrated the fabrication of a thin layer flow cell which incorporated a PANI-modified electrode (5 x 0.110 x 0.180 mm) as a sensing material. A schematic of the electrode integration within the PDMS microfluidic housing is shown below in Figure 1.13. Reference and counter electrodes were housed within the microfluidic channel outlet. The sensor, housed within the channel had a sensitivity of 15.70 µA mM^{-1} cm^{-1} for ascorbic acid at flow

rate of 1 µL min^{-1} [57], which was greater than a batch cell comparison [95] showing a benefit of microfluidic-based analysis.

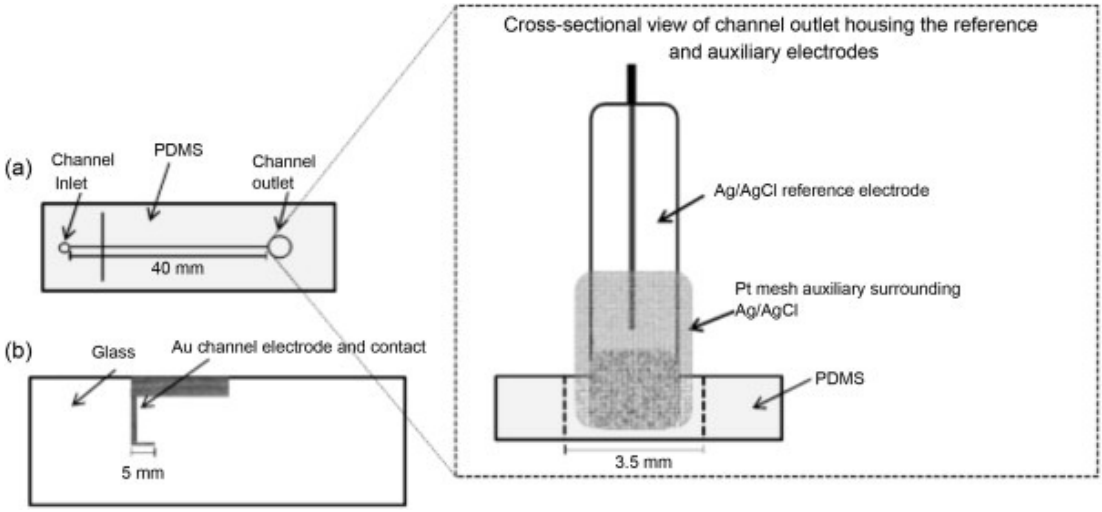

Figure 1.13: Microfluidic chip schematic showing the (a) PDMS channel (40 mm x 220 µm x 35/60/110/180 µm) and the inlet and outlet ports and (b) glass base. The channel working electrode (5 mm x 110 µm) was sputtered onto the glass base substrate. A cross-sectional view of the PDMS channel outlet (3.5 mm) housing the Ag/AgCl reference electrode surrounded by the Pt mesh auxiliary electrode is given in the inset (drawing not to scale), reproduced from [57].

ICPs have also been demonstrated as having a potential application in microfluidic controlled release platforms. Ge *et al.* [96] showed the fabrication of a microchip device with multiple gold electrodes (300 x 300 µm) onto which PPY was electrochemically polymerised. During polymerisation PPY films were doped with two drugs; sulfosalicylic acid (SSA) or adenosine triphosphate (ATP) in an aqueous solution with pyrrole monomer. Initially drug-doped PPY was polymerised and subsequently washed. A second layer of Cl^- doped PPY was then polymerised over the PPY-SSA layer, examples of PPY-ATP, PPY-SSA and bare gold electrodes used by Ge *et al.* are shown in Figure 1.14. This helped to prevent any drug release at

open circuit potential. It was noted that by increasing or decreasing the thickness of the Cl^- doped PPY layer (0.5 – 2 µm) and varying $E_{app,}$ the release rate could be regulated. The electrodes could then be independently controlled via application of an electrical potential for selective controlled release. The microchip design was appealing due to its small size, good biocompatibility and selective release [96]. The benefit of µchips, like that demonstrated by Ge *et al.,* offer potential applications in the area of implantable devices for clinical applications.

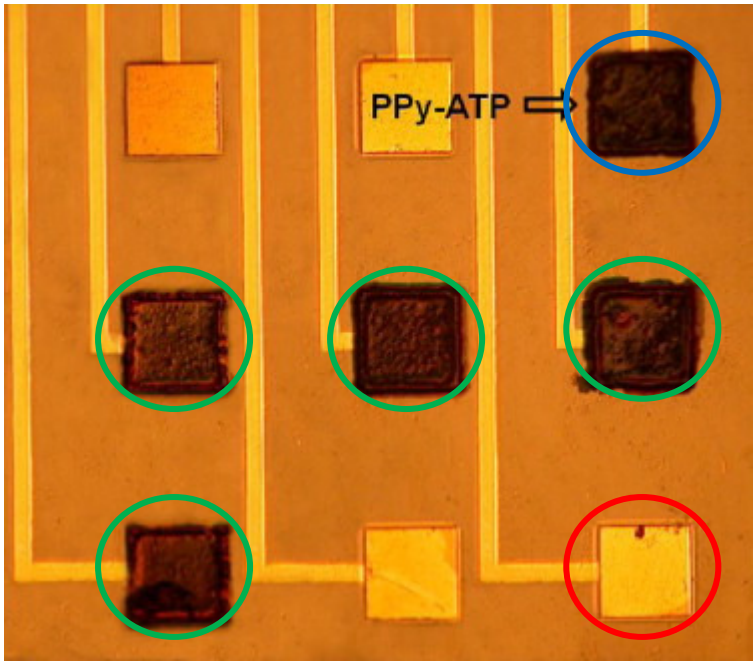

Figure 1.14: Metallurgical microscope image of microchip design used by Ge et al. exhibiting four microelectrodes doped by SSA (circled in green) and one doped by ATP (circled in blue). An example of a bare gold working electrodes is also shown circled in red. Reproduced from Reference [96].

Microfluidic platforms have also been exploited as a vessel for the synthesis of ICP materials yielding controlled morphologies. For example, Beesabathuni *et al.* [97] demonstrated the fabrication of porous PANI microspheres using droplet microfluidics. The microspheres were prepared via a one-step synthesis method. The

conductivity of the spheres could be tailored based on acid concentration during polymerisation. The hollow microspheres have high potential for controlled release applications due to biocompatibility, conductive nature and porosity, Figure 1.15 below details the microfluidic housing used for PANI microsphere fabrication.

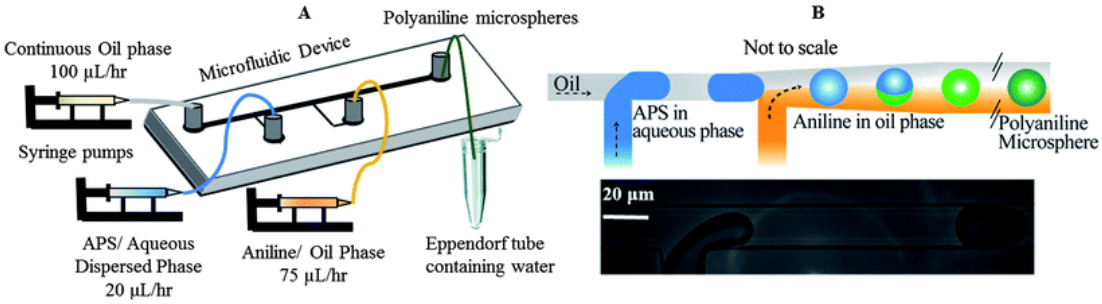

Figure 1.15 shows an example for of experimental set up by Beesabathuni et al. where PANI microspheres were produced in a T-junction microfluidic device containing aniline in oil medium as the continuous phase and APS in aqueous medium as the dispersed phase. The polymerised aniline microspheres were transported off-chip through an outlet, reproduced from Reference [97].

Another interesting property of ICP materials for microfluidic platforms is their ability to facilitate actuation. Actuation of ICPs has been shown to control fluid flow in a stop/start manner as well as regulating flow rate *e.g.* ICP-based pumps. Due to the versatility and switchability of ICP materials in conjunction with the small volumes required for microfluidics, ICPs in this format are particularly amenable for actuation. Causley *et al.* [98] demonstrated the actuation within a polydimethylsiloxane (PDMS) µchannel 700 µm in width, which was coated with a 700 nm thick PPY film doped with dodecylbenzene sulfonate (DBS), as shown in Figure 1.16. Upon application of a negative potential where reduction of the PPY film was expected, fluid flow into the µchannel was initiated. When the film was oxidised at more positive potentials, fluid flow was stopped. The actuation of flow

was based on the switching of the PPY between doped and dedoped state. Incorporation of DBS as dopant resulted in a hydrophobic surface due to orientation of the hydrophobic tail out of the polymer network, and the charged hydrophilic head group incorporated as a counter ion when doped. Upon dedoping the surface became more hydrophilic due to orientation of the hydrophilic head group out of the polymer network.

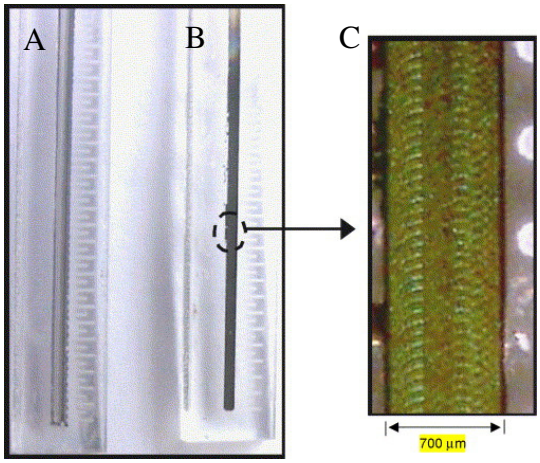

Figure 1.16: Shows a photograph of A) a platinised channel and B) a PPY-DBS coated channel with C) showing a close up image of the PPY-DBS coated channel, reproduced from [98].

More recently, Kim *et al.* [99] showed the incorporation of a similar PPY actuator system into a microfluidic platform for use as an integrated micro-pump system. The PPY micro-pump used actuation of two separate PPY films. Through application of opposite potentials, flow could be manipulated as a result of the push/pull effect of actuation. The ICP based micro-pump system was self-priming and had a maximum pump flow rate of 52 µL/min, an integrated PPY micro-pump system is shown in Figure 1.17.

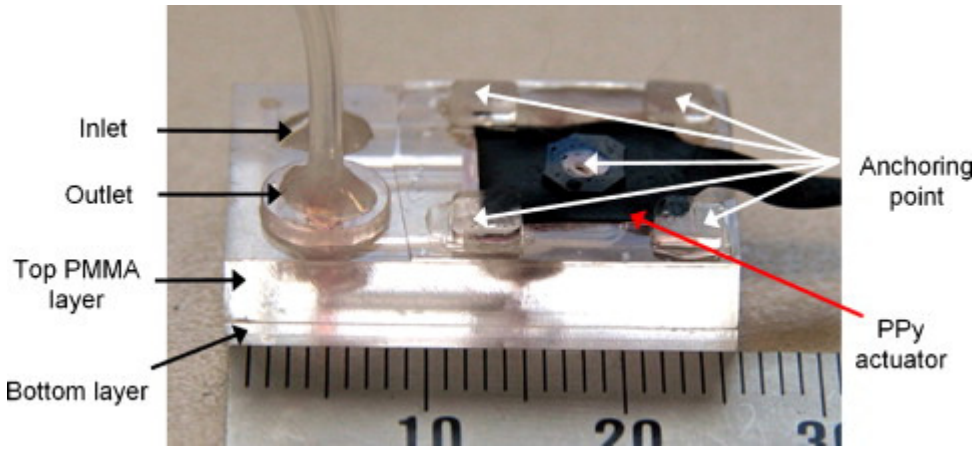

Figure 1.17: shows an image of the microfluidic pump fabricated by Kim et al. showing the inlet/outlet of the system and the housing for the PPY actuator illustrating the small size of the integrated system, reproduced from [99].

The benefit of coupling ICP materials with microfluidic platforms for sensing, separation, controlled release and actuation is clear with increased sensitivity, reduced size and reduced polymerisation time with increased control over ICP morphologies. The integration of stimuli-responsive ICP materials into microfluidic platforms therefore offers a unique analytical tool with low sample and reagent consumption, in addition to flow-through and real-time capabilities which can be multiplexed easily in this format. Recent advances have allowed the redox control of ICP materials to be done chemically or electrochemically in-situ on-chip, while transduction techniques can be optical or electrochemical. It is clear that the merger of intelligent materials such as ICPs with microfluidics is an emerging area still with many new potential application and advancements to be seen in coming years.

1.3 ICP morphology in Lab-On-Chip applications

A summary of the morphologies of ICP materials housed in microfluidic platforms as discussed above is detailed here with SEM images of typical morphology shown

in Figure 1.19. Chemical and electrochemical polymerisation methods have both been successfully employed to create ICP structures on-chip. Hard, soft and template free polymerisation methods have been demonstrated with the desired final application the deciding factor for many research groups.

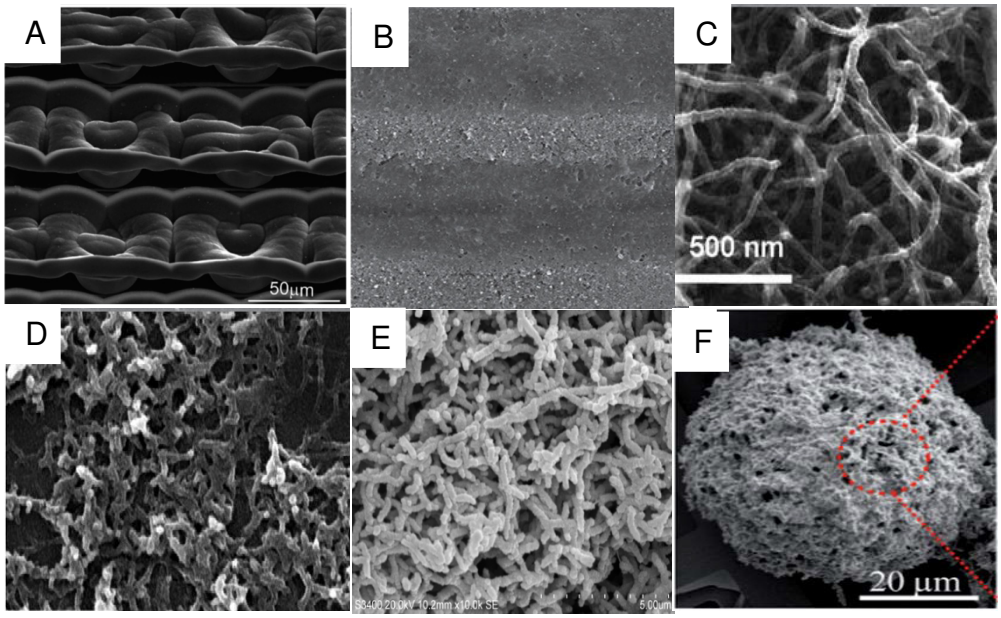

Figure 1.19: SEM images summarising ICP morphology fabricated within microfluidic housings. A) Electrochemically polymerised PPY 3D-cages, [89], B) chemically polymerised drop-cast PANI fibres [91], C) electrochemically polymerised PANI nano-wires [93], D) chemically polymerised 3D PANI fibre isles [94], E) electrochemically polymerised bulk fibrillar PANI [57] and F) chemically polymerised PANI microspheres [97].

For example, Perez-Gonzales *et al*. [89] electrochemically polymerised PPY through a hard template which directed the PPY into 3D post-like structures, Figure 1.19A. Photoresist was used to fabricate the hard template which upon UV exposure with an appropriate mask produced wells 25 µm in diameter and 24 µm in depth. Electrochemical polymerisation was performed for 22 min at 1 µm min^{-1} to grow the PPY 3D posts. Similarly, 3D cages were fabricated by firstly electrochemically

polymerising 3D posts as detailed above with a further electrochemical deposition step of 11 min to merge the posts. This hard template directed electrochemical polymerisation was very effective in fabricating controlled morphologies in-channel. However, the deposition was multi-step and time consuming. Removal of the photoresist was necessary which increased further fabrication time and complexity of ICP deposition. Henderson *et al.* [91] fabricated PANI films via drop-casting of chemically polymerised PANI nano-fibre suspensions in water onto a planar acrylic surface before isolating specific electrode areas. Upon drop-casting, the nano-fibres formed an interwoven fibrillar film. Flash welding was then employed to isolate sections of the PANI film. As a result of the drop-casting method the reproducibility of films is potentially a drawback. However, the fibrillar nature of the suspension results in high surface area PANI with the flash welding process reproducibly isolating fixed areas.

In a template-free method used by Wang *et al.* [93], PANI nano-wires were fabricated electrochemically within a sealed microfluidic platform. The resulting PANI nano-wires were 50 – 80 nm in diameter with well-defined wire morphologies. The nano-wires successfully covered the exposed area of the electrode after 40 min. This fabrication time was significantly reduced in comparison to open channel polymerisation where nano-wire polymerisation was achieved over 6 h. The resulting nano-wires after open channel polymerisation demonstrated less-defined wire morphologies when compared to nano-wires fabricated in μchannel, showing the control in morphology and reduced time associated with microfluidic analysis.

A chemical polymerisation of aniline performed in a sealed micro-capillary overnight resulted in 3D PANI isles consisting of nano-fibres ~200 nm in diameter and several microns in length were presented by Florea *et al.* [94]. The method

proved effective in fabricating an optical sensor for aqueous ammonia. During optical sensing flow was demonstrated over and not through PANI nano-fibres on the walls of the capillary. As a result only a small volume of the total solution came in contact with the PANI nano-fibres on the walls. Power *et al.* [57] electrochemically grew bulk PANI films voltammetrically within a sealed microfluidic channel for ascorbic acid detection. Polymerisation was achieved in both flow and stopped-flow formats. The resulting PANI morphology was bulk fibrillar. Polymerisation was seen to plateau upon reaching 50% of the channel depth likely due to displacement of the flowing monomer solution with PANI and hence an increase in solution velocity. As a result of this plateau effect, complete filling of the channel depth with PANI was not possible. Therefore, flow was again directed over the PANI-modified electrode, rather than through the deposited PANI network, via the path of least resistance. This reduced the available ICP surface area for sensing applications.

A novel polymerisation method presented by Beesabathuni *et al.* [97] demonstrated a chemical polymerisation method to fabricate PANI microspheres using droplet fluidics. Droplets of aniline monomer in oil were gradually pumped into a continuous flow of aqueous based initiator (APS). The resulting microspheres were porous structures, 50 µm in diameter consisting of fibrillar structures between 200 – 500 nm in diameter. The fibres were interwoven to form a microsphere structure with resulting pores on the surface between 300 nm – 1 µm. The porous/hollow nature of the microspheres is potentially useful for future controlled release applications. However, a drawback of this method was the need for drop-casting of the microspheres onto an electrode surface after fabrication.

Each of the methods described above illustrate the ease in which a discrete morphology, as well as depth and density can be fabricated, highlighting the ease at

which a variety of ICP forms are obtainable within microfluidic channels. The variety of morphologies discussed is not exhaustive, and it is anticipated that novel and innovative fabrication strategies will continue to emerge in the immediate future.

1.4 Fabrication and Characterisation Methods

Central to this thesis is the fabrication and characterisation of novel materials and material structures. The primary techniques which were utilised to achieve these goals are detailed in this section.

1.4.1 Scanning Electron Microscope (SEM)

Throughout this work characterisation of materials relied heavily on scanning electron microscopy (SEM). A Hitachi S-3400N SEM was used for all SEM analysis. The S-3400N is a thermionic system which utilises a tungsten filament as the electron source. Here, electrons are accelerated between 1 – 30 kV through a voltage difference towards a specimen. The working distance was relatively large (*e.g.* 10/15 mm) and therefore investigation of large samples was possible. A schematic of the S-3400N system is shown in Figure 1.20.

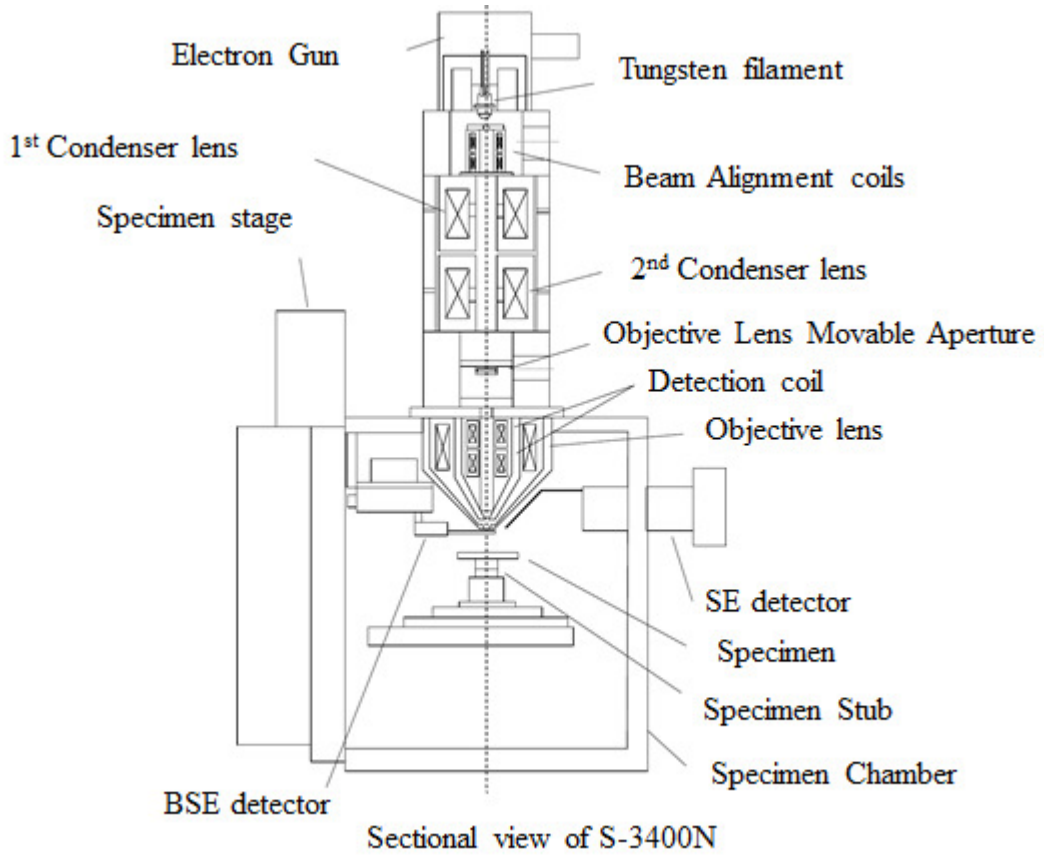

Figure 1.20: Schematic diagram of an S-3400N SEM system showing a sectional view, reproduced from Hitachi S-3400N User Manual page 62.

Two main electron-specimen interactions during analysis allow for image development, namely elastic and inelastic interactions [100]. Elastic and inelastic scattering combine to give insight into the topography, morphology and elemental composition of a specimen. Elastic scattering is a process which does not change the energy of the primary electron. Elastic scattering is as a result of Coulombic interactions which involve electrostatic charges between the specimen (nucleus and electrons) and primary electron. The likelihood of elastic scattering depends greatly on the atomic number of the specimen. Specimens with higher atomic number result in increased scattering. In contrast inelastic scattering causes the primary electron to

lose a detectable amount of energy. Inelastic scattering gives information on the specimen as a result of secondary effects such as secondary electrons (SE).

The types of signals which can be used for interpretation of a specimen include SE, backscattered electrons (BSE) and X-rays [101]. SE is the most widely used signal with the energy of SE low at 10 – 50 eV. To detect SE signals, SE are accelerated onto a scintillator and the signal is recorded by a photomultiplier. SE have a low exit depth from the specimen (~1 – 10 nm) and offer information on the topography of the specimen. With BSE, in contrast to SE, signals move on straight trajectories and are not affected by electrostatic collection fields. The number of BSE are dependent on the atomic number (higher atomic number increases beam/specimen interaction) of the species being analysed and offers 3D information on the specimen during analysis [100]. Finally, X-rays are formed as a result of bombardment of the material with high energy electrons and subsequent emission of characteristic X-rays with wavelengths dependent on the atoms of the specimen. X-rays therefore offer a method for elemental analysis [100].

When preparing a specimen for SEM analysis the composition of the specimen must be considered. When an electron beam interacts with a specimen there are electrons leaving the sample as BSE and SE and there is a continuous beam of electrons hitting the sample. To ensure a consistent, high resolution image the rate of electrons leaving the sample must be equal to the rate of electrons hitting the sample [101]. However, for most specimens the operating current would have to be very low for this to be possible and generally out of the normal operating range of SEM systems. As a result there is a build-up of surplus electrons on the surface of the specimen which over time build-up to a large enough negative charge to repel incoming electrons resulting in a distorted image due to “charging”. The issue of charging

presents itself for non-conducting samples such as polymers and biological samples, for which there is a greater build-up of surplus electrons. Due to the conductivity of metals a metal coating can be placed onto biological/polymer specimens through sputtering to increase conductivity and reduce charging. Biological and polymeric samples may also degrade with higher beam currants due to heating of the specimen as well as degradation due to volatility of specimen in a vacuum. As a result fully dehydrated and sputtered samples are regularly used. During this work sample preparation included dehydration of PS suspensions and polymer coatings before a thin film of gold (~20 – 25 nm thick) was sputtered onto the surface immediately prior to SEM analysis. Following this preparation method high beam currents (20 kV) could be used to obtain high resolution SEM images of polymeric specimens.

1.4.2 Electrochemical polymerisation and characterisation

Throughout this work the electrochemical techniques used for polymerisation and characterisation of polymer films were cyclic voltammetry (CV) and chronoamperometry. Both electrochemical techniques used a three electrode cell with a gold sputtered working electrode (WE), a Ag/AgCl reference electrode and a counter electrode of platinum mesh.

1.4.2.1 Cyclic Voltammetry

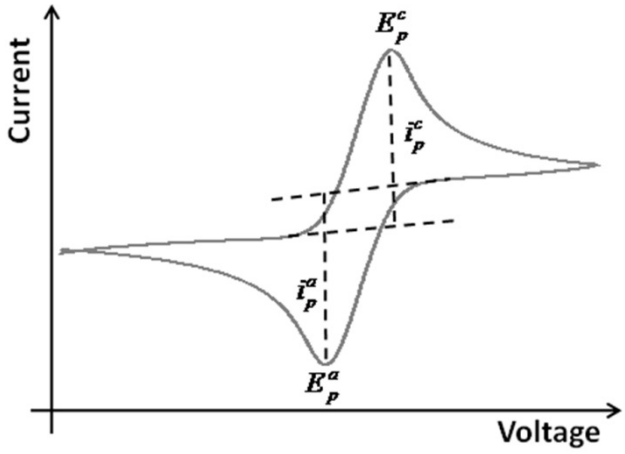

Figure 1.21: Schematic illustrating a CV of a reversible reaction where E_p is the peak potential and i_p is the peak current (a, anodic and c, cathodic) reproduced from [102].

CV utilises a potential scan whereupon reaching a maximum potential the sweep direction is inverted and the sample is scanned in the opposite direction to a minimum potential. As sweep rate is increased the time for the system to reach equilibrium is reduced at the electrode surface therefore changes in reactions can occur with increasing scan rates (i.e. reversible system at slow sweep rates/quasi reversible system at high sweep rates) [103]. The shape of a CV rises upon reaching a potential where an electrode reaction begins. This results in a concentration gradient as electro active species are consumed and a maximum is reached (peak current). Upon reaching this maximum, the supply of electro active species begins to fall and the current therefore falls. An example of a CV is shown in Figure 1.21, where the symmetric oxidation and reduction peaks, comparable peak areas and separation of peak maxima of 59 mV/n (where n = number of electrons transferred) illustrate a fully reversible electrochemical reaction. This CV results from the rapid

exchange of electrons between the oxidative and reductive species with the working electrode. For systems which display peaks which are not as symmetric as those shown in Figure 1.21 they are deemed quasi-reversible. Completely irreversible systems will display only one peak and no reverse peak will be noted [103].

1.4.2.2 Chronoamperometry

Chronoamperometry involves monitoring the change in current due to oxidation or reduction of a species at a fixed potential over time. The redox process results in flow of current between the working and counter electrodes. The current which is passed can then be used to determine concentration of redox active species [103].

During electrochemical experiments two types of processes occur at an electrode namely Faradaic and non-Faradaic. When electron transfer occurs causing a redox reaction these processes are called Faradaic processes. When no electron transfer occurs but adsorption and desorption occurs changes in the interface between the electrode/solution occur which are non-Faradaic processes. As a result during electrochemical experiments due to manipulation of redox reactions, Faradaic processes are of most interest. However, both Faradaic and non-Faradaic processes occur during electrochemical experiments [104].

1.4.2.2 Benefits of Microelectrodes

Microelectrodes are electrodes which have at least one dimension that is of the order of 0.1 – 50 μm. Microelectrodes offer advantages over macroelectrodes of larger dimensions due to increased current density due to radial and perpendicular diffusion, as shown in Figure 1.22, as well as greater mass transport. In conjunction microelectrodes demonstrate reduced capacitance giving the potential for an increased range of potential scan rates. These benefits in conjunction with the

reduced size and faster response of microelectrodes have led to applications within microfluidics [105].

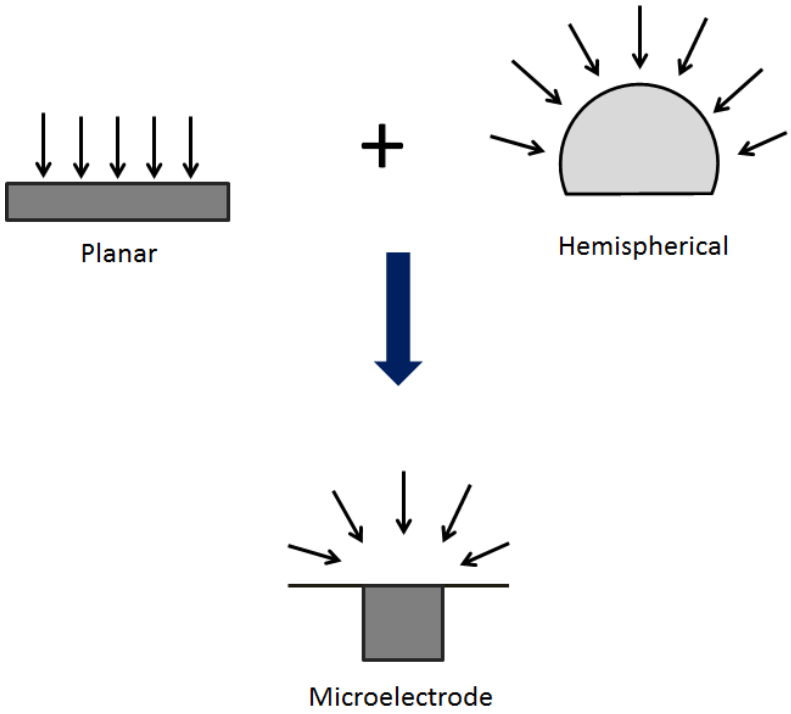

Figure 1.22: Schematic showing uniform current density at a planar and hemispherical electrodes and the non-uniform accessibility of a microelectrode reproduced from reference [103].

1.5 Conclusion

As detailed above the application of ICP's in lab-on-chip applications shows some success, with many research groups having found novel methods to incorporate and control ICPs within lab-on-chip platforms. Chemical and electrochemical polymerisation methods have both been successfully used within microfluidic platforms. However, fabrication of 3D flow-through ICP structures has not to date been studied.

Fabrication of high surface area flow-through ICP materials will be a main focus of this thesis. Firstly, the fabrication of a novel templating method within the confines of a μchannel must be accomplished. The aim is therefore to firstly fabricate a 3D ordered template within the confines of a μchannel, then the structural direct polymerisation of an ICP in a μchannel, and subsequently investigate the resulting 3D order and electrochemical control of the ICP material.

1.6 Thesis outline

The purpose of this work was to address the current limitations of microfluidic platforms including: fabrication of 3D order templating approach in channel. Initially the fabrication of high surface area flow through ICP materials will be a main focus. To address this current limitation the fabrication of a novel templating method within the confines of a μchannel must be accomplished.

Chapter two will report on the fabrication of a reproducible 3D ordered hard template housed within a μchannel. The fabrication of unimodal CC (uCC) and binary CC (bCC) was investigated. The growth mechanism of uCC and bCC structures in channel was explained and the optimised parameters detailed with analysis of resulting structures. The optimised facile fabrication method for uCC and bCC structures with 3D order was observed. The resulting structures offer a unique templating method for tuneable ICP surface areas within a microfluidic housing with resulting CC thickness over 35 – 220 μm.

The control over CC thickness detailed in Chapter 2 allowed for electrochemical polymerisation of 3D ordered ICP materials. The optimised uCC and bCC were used to structurally direct the polymerisation of the ICP, PANI within a microfluidic channel. Chapter 3 reports the optimisation of PANI inverse opals through electrochemical polymerisation. Variation in polymerisation time was investigated with the resulting PANI structures analysed. The growth of PANI in channel resulted in distinct morphologies based on polymerisation time.

Chapter 4 investigates the resulting homogeneity of PANI inverse opals reported in Chapter 3 which were electrochemically polymerised in channel. Electrochemical polymerisation, bulk chemical polymerisation and surface confined chemical

polymerisation methods were then explored to further optimise homogeneity throughout the depth of the μchannel. The electrochemical control of the homogenous 3D ordered PANI films was then characterised.

In Chapter 5 with a view to further control over PANI films, investigation of dopant type was undertaken. HCl-doped and SDS-doped PANI films were fabricated by electrochemical polymerisation and subsequently compared through water contact angle (WCA), morphology and surface roughness. Incorporation of SDS into the polymer backbone at a molar ratio of 0.02 aniline:SDS produced PANI films with controllable hydrophobicity via doping/dedoping. Conclusions and recommendations for future work arising from this thesis are given in Chapter 6.

Chapter 2

Fabrication of a 3-Dimensionally Ordered Binary Colloidal Crystal within a Confined μChannel

2.1 Introduction

3D ordered macro-porous (3-DOM) materials have potential applications in many diverse fields such as fuel cells [106, 107], catalysis [108] and chromatography [109]. Multiple strategies are available for the fabrication of 3-DOM materials [110]. The use of sacrificial polymeric particle templates is summarised here. Comprehensive reviews of other fabrication methods can be found elsewhere [111-113]. Unimodal and bimodal templates have seen extensive research in recent times due to the potential application in 3-DOM material fabrication. Common templates include silica spheres, which are removed by etching with hydrofluoric (HF) acid, and polystyrene (PS) spheres, which are removed by dissolution with an appropriate solvent or by calcination [114]. Literature details numerous fabrication methods for both unimodal [107, 115-117] and bimodal [118, 119] PS templates, as discussed below.

Unimodal templates can be formed reproducibly through well-understood methods such as dip-drawing [116] and drop-casting [120]. However, due to the coffee ring phenomenon areas of reduced reproducibility in the centre of the colloidal crystal (CC) are noted for drop-casting methods thus limiting their use as templates.

Other approaches to form 3-DOM materials employ nano-spheres (PS or silica) in combination with surfactants or co-polymers [121-124] to add bimodal porosity. The formation of reproducible macro-pores (i.e. pores resulting from the interconnected marco-spheres) using unimodal PS CC templates is well understood. Upon addition of a surfactant after CC fabrication, infiltration of the surfactant (or copolymer) in the interstitial voids between the spheres allows for the formation of macro-/meso-porous material after template removal by calcination or solvent extraction [125]. In

this method, while porosity of the final structures is reproducible, the fabrication of meso-pores with reproducible order and position is not achieved.

More recent examples have used macro-spheres in conjunction with nano-spheres of either PS or silica to form bCC improving uniformity. Formation of bCCs through self-assembly [126-130] and solvent evaporation [131] have been shown with nano-spheres present in interstitial voids of the macro-spheres. Uniformity in the resulting structures depends heavily on the volume fraction of nano (denoted small, S) to macro (denoted large, L) spheres ($VF_{S/L}$) and the diameter size ratio of PS spheres ($D_{S/L}$), in solution during bCC formation [132]. Boundary conditions for $VF_{S/L}$ and $D_{S/L}$ have been detailed extensively by Ozin *et al.* during fabrication of bCC monolayers by evaporation-induced self-assembly [133].

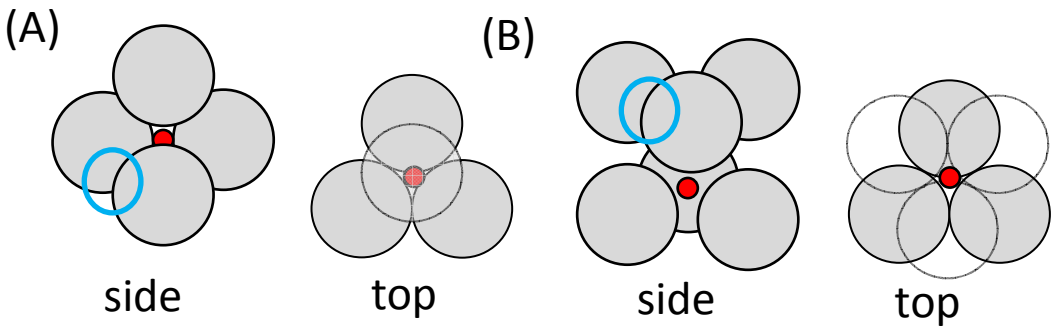

Schematic 1: diagram of (A) tetrahedral and (B) octahedral interstitial voids with macro-spheres denoted in grey and nano-spheres in red. Examples of channel voids are circled in blue [126, 130].

During co self-assembly of 3D PS or silica macro-sized spheres there are three sites available for nano-sized PS spheres packing; tetrahedral and octahedral interstitial voids and channel voids, as illustrated in Figure 2.1 [129, 134, 135]. In 3D face

centred cubic (fcc) formation, if the next layer results in a PS sphere sitting in the "dimple" created by the trigonal void of these three spheres, a tetrahedral void is created. If the second layer results in another trigonal void sitting above the first trigonal void, an octahedral void is created. The effect of size ratio and relative concentration of nano- and macro-sized spheres on filling of tetrahedral and octahedral voids during bCC fabrication by vertical lifting, where multiple layers are deposited simultaneously, has been explored in detail [129]. The octahedral void has a theoretical size limit of $D_{S/L}$= 0.4142 while the tetrahedral void has a theoretical size ratio limit of $D_{S/L}$= 0.225 [129, 130]. However, in practice, the size limit for these interstitial voids was found to be approx. $D_{S/L}$= 0.26; above this, loss of close-packed structures were observed [129, 136]. The second available void type is the channel void between two neighbouring macro-sized PS spheres, circled in blue in Figure 2.1. The channel void has an upper theoretical size ratio limit of $D_{S/L}$= 0.150 [126, 134]. Below a value of $D_{S/L}$= 0.150 nano-sized PS spheres are able to flow freely into the channel void and pack in the area between neighbouring macro-spheres. As a result this disrupts macro-sized sphere close packing during convective self-assembly.

To successfully pack nano-sized spheres exclusively within the tetrahedral and octahedral voids a theoretical particle size range between $0.150 \leq D_{S/L} \geq 0.225$ must be used. Between this range the nano-sized PS spheres will pack in the tetrahedral and octahedral voids only [129]. An increase in $VF_{S/L}$ can increase the number of nano-sized PS spheres packed within the interstitial void but $VF_{S/L}$ must be controlled to achieve an ordered structure. Order in bCC structures was noted at low $VF_{S/L}$ ($VF_{S/L}$ = 0.001), with disorder and loss of close packing of macro-sized spheres at higher $VF_{S/L}$ ($VF_{S/L}$ = 1) which result in an excessively high concentration

of nano-sized PS spheres during packing in this case. Yang *et al.* reported limits of $D_{S/L}$ and $VF_{S/L}$ where order was noted for $D_{S/L}$ = 0.207 between $VF_{S/L}$ values of 0.0178 (lower) and 0.0356 (upper). As expected disorder was confirmed outside these limits *e.g.* at $VF_{S/L}$ = 0.0713 for $D_{S/L}$ = 0.207. Upon reduction of the nano-sphere size, reducing the size ratio to $D_{S/L}$ = 0.122 below the channel void threshold of $D_{S/L}$ = 0.150, nano-sized PS spheres were observed as expected in both the tetrahedral/octahedral interstitial voids and channel voids. Order was noted at much lower $VF_{S/L}$ = 0.0036 in this case but upon increasing $VF_{S/L}$ beyond $VF_{S/L}$ = 0.0073, an increase in disorder was noted [128], which was consistent with previous work in this area [127, 134].

In this work the investigation of strategies for the fabrication of 3D PS bCC templates in defined μchannel dimensions initiated by capillary force packing is presented. To date much of the work fabricating ordered PS and silica bCCs has been achieved in monolayers through convective self-assembly at the water air interface [126, 132], or in multilayers through drop-cast convective self-assembly [130, 137] and dip-drawing methods [32]. Using convective self-assembly at the air water interface, highly intricate 2D mono-layer structures can be fabricated but formation of such bCCs in defined geometric areas such as fluidic μchannels would be extremely difficult, as a reproducible water air interface would need to be isolated solely across the confines of the μchannel [135]. In addition, multiple layers of crystal typically are not formed using this method except through layer by layer deposition of individually formed monolayers.

Alternatively, drop casting methods can allow for fabrication of CC over large substrate areas with high uniformity, quickly and simply [138]. However, cracks are common between ordered sections of CC as a result of drying. [139] Another issue to

consider when using drop-casting is the coffee ring phenomenon which directly affects the reproducibility of CC formed. [140, 141] This phenomenon causes an untemplated area in the mid-section of the resulting CC due to pinning and subsequently drying at the edge of droplets first before moving towards the centre over time [139, 140]. Dip drawing, which utilises the slow drawing of a substrate from an aqueous suspension of PS or silica spheres to form an ordered CC structure over a large substrate area has seen wide spread use due to the high order of the resulting CC. Optimisations of drawing speed and sphere % w/v concentration [142] as well as temperature [143] are essential for reproducible CC fabrication and control of the resulting CC thickness [144, 145]. With higher % w/v (*e.g.* 10 – 20% w/v suspensions), thicker CC can be achieved; however withdraw speed was shown to control the resulting order of the CC formed with increased reproducibility at slower withdrawal speeds (*e.g.* 1-0.1 μm/s) resulting in a very time-consuming fabrication method [146]. It must be noted that in using dip-drawing the CC is fabricated over the full substrate area placed in the PS/silica suspension which does not allow for CC fabrication within a confined geometric constraint limiting the application of this method to planar surfaces.

Spin coating has also been used successfully as a means to fabricate CC over very large areas with 2D and 3D order. [147] The method is fast and effect [148, 149] but does require optimisation of spin coating speed and suspension concentration for increased order [147, 150]. Due to the large area covered during fabrication the presence of cracks and defects of the spin coated CC are common [147]. Controlling CC fabrication within a confined geometric constraint such as a μchannel would not be possible utilising spin coating.

Other examples of CC fabrication methods include sedimentation and convection self-assembly at the water air interface [151, 152]. The fabrication of ordered CC has been observed for both methods, however sedimentation is time-consuming and control over the final structure formed is minimal. In the case of convective self-assembly CC can be fabricated but the drawback of such methods is the multistep process required to form the final CC structure [153].

Previous work on fabrication of CC within μchannels by Ozin *et al.* utilised a multistep self-assembly method with sonication and Xia *et al.* utilising directed evaporation-induced self-assembly have shown unimodal CC fabrication in confined areas with order noted [154, 155]. However, the fabrication of CC in these methods was multi-step and time consuming.

A summary of the benefits/limitations of current CC fabrication methods is summarised in Table 2.1 and compared to the work presented in this Chapter. The facile CC fabrication method developed in this work offers for the first time a quick and reliable method for uniform uCC and bCC template fabrication within the confines of a μchannel. In this method 3D bCC structures were fabricated exclusively within the μchannels within 12 h which were ordered along the length, width and depth of the cuboid channel it was formed within (albeit with some defects). The benefits of this method are the independence of CC thickness from $VF_{S/L}$, in this work thickness is dictated by μchannel depth only as well as ease of fabrication, high uniformity and 3D order of final PS templates. The capillary force packing method developed in this work offers for the first time a method to fabricate bCC reproducibly specifically within μchannel, unlike other methods such as drop casting, spin coating and dip-drawing which were designed for CC fabrication of planar substrates.

Table 2.1: Comparison of benefits and limitations of current CC fabrication methods

Method	Benefits	Limitations
Dip drawing	- High order - Reproducibility	- Time consuming - Cannot be fabricated in channel - Multi-step - CC thickness limited by $VF_{S/L}$
Drop-casting	- Quick - Fabricated over large area	- Coffee ring phenomenon/reduced order - Not reproducible in channel - Difficulty controlling CC thickness - CC thickness limited by $VF_{S/L}$
Sedimentation	- Simple fabrication method	- Time consuming - Little control over final structure
This Work	- High order & reproducibility - ***Can be fabricated in channel*** - Facile Fabrication method - ***CC thickness independent of $VF_{S/L}$***	- Not applicable to planar substrates

2.2 Experimental

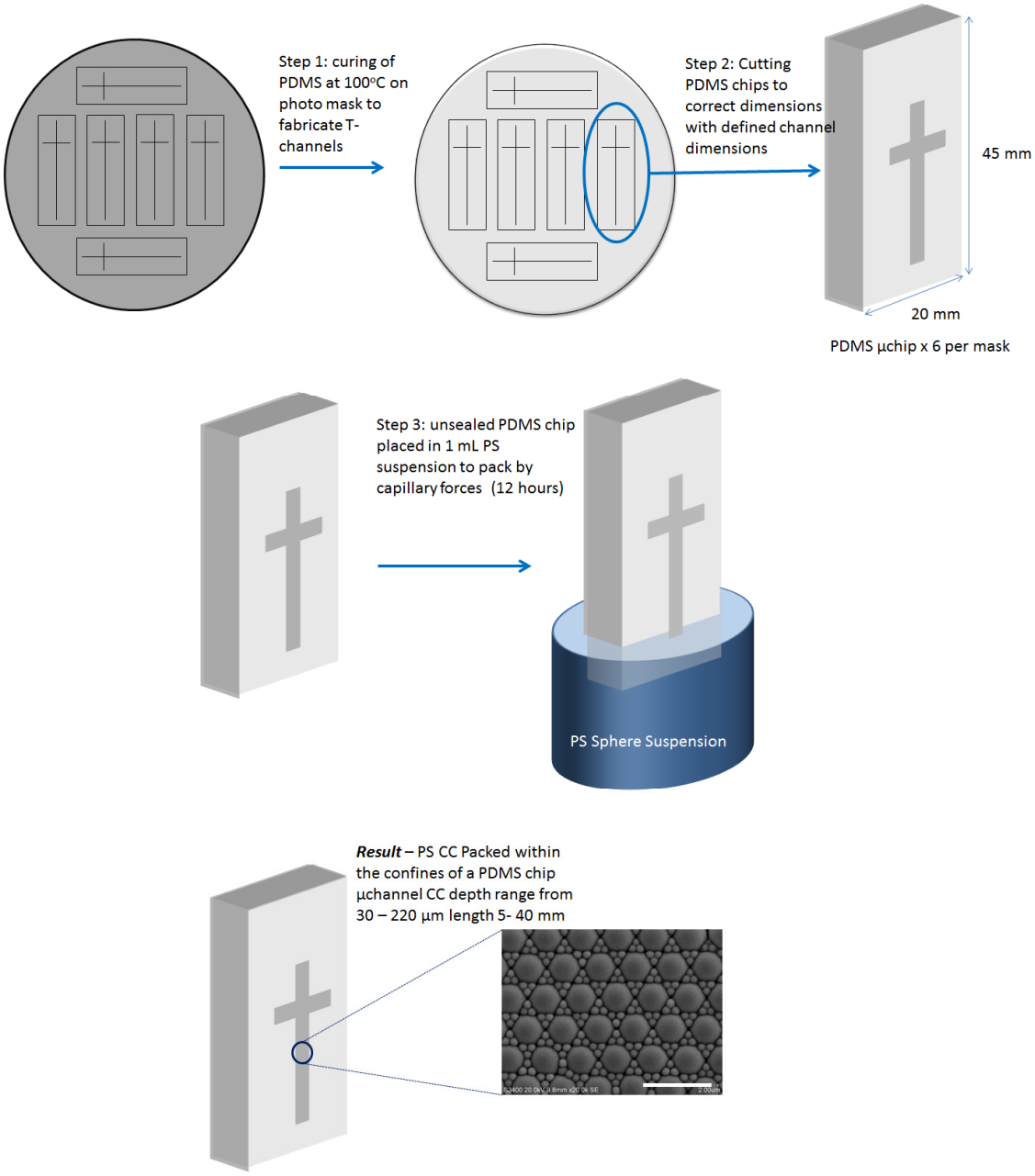

Schematic 2.1: Schematic illustrating the method of fabrication for PS uCC and bCC within the confines of a glass µchip.

2.2.1 Materials

PS spheres of diameter 200 nm (± 2.3 %) and 1 µm (± 3 %) were purchased from Duke Scientific (Palo Alto, California, USA). All PS sphere suspensions as received contained 0.1-0.5 % surfactant to inhibit agglomeration and promote stability.

Deionized water was purified using a MilliQ system to a specific resistance of greater than 18.2 MΩ-cm. Polydimethylsiloxane (PDMS) (101697) (Dow Corning 184 silicone elastomer), was purchased from Farnell (Ireland). Tetraethyl orthosilicate (TEOS) reagent plus >99 % purchased from Sigma-Aldrich (Dublin, Ireland). Hydrochloric acid ~ 37 % was purchased from Fisher Scientific UK Bishops Meadows Road, Loughborough. All other chemicals were purchased from Sigma-Aldrich (Dublin, Ireland) and were of analytical grade.

2.2.2 Instrumentation

SEM micrographs were obtained using a Hitachi S3400N scanning electron microscope (Hitachi, UK) at an acceleration voltage of 20 kV, probe current of 35 µA and working distance of 10 mm. All samples were gold-sputtered using a 750T sputter coater, Quorum Technologies, Lewes Road, Laughton, Lewes, East Sussex, BN8 6BN, UK. A Harrick plasma cleaner (PDC-002) was used for all oxygen plasma performed on PDMS chips. A Malvern nano-sizer ZS was used for all zeta potential measurements. An Ocean Optics UV-visible spectrophotometer was used for UV-Vis measurements with spectra suite software.

2.2.3 Methods

2.2.3.1 PS sphere preparation

Immediately prior to use to prevent agglomeration [156], anionic surfactant was removed from PS sphere stock suspensions. PS suspensions of 1 µm spheres were centrifuged and re-dispersed in deionized water three times at 5000 rpm for 7 min. PS suspensions of 200 nm spheres were centrifuged and re-dispersed in deionized water three times at 12,000 rpm for 45 min. Zeta potential measurements for 200 nm and 1 µm PS spheres were low to neutral with zeta potentials of 0.0997 mV for 200

nm and -2.84 mV for 1 µm PS spheres. 50 zeta runs were performed in triplicate in an aqueous medium at 25°C after removal of surfactant.

2.2.3.2 PDMS chip fabrication

Silicone elastomer and curing agent were mixed in a 1:10 w/v ratio, degassed for 45 – 60 min under vacuum, and poured onto a silicone mould prepared using photolithography. The resulting PDMS chip with cross channel of dimensions of 0.035 mm x 0.110 mm x 40 mm or 0.110 mm x 0.180 mm x 40 mm, was cured at 100°C on a hotplate for 45 min. PDMS chips were then cut to correct size, 45 mm x 20 mm, after curing.

2.2.3.3 Unimodal CC fabrication with variation in surfactant concentration

PS suspension of 1 µm spheres was treated as per Methods Section 2.2.3.1 and re-dispersed in varying concentrations of sodium dodecyl sulfate (SDS) surfactant from 0 – 0.1 % w/v. Oxygen plasma was performed on all µfluidic chips, to activate the surface of the PDMS before capillary force packing, for 5 min. Oxygen plasma was performed under an atmosphere of air using a Harrick plasma cleaner (PDC-002) before the chips were placed into the PS suspension ensuring the µchannel base was immersed in the suspension. This was then heated at 45°C for 12 h to allow PS spheres to form the unimodal CC in the µchannel.

2.2.3.4 3D binary colloidal crystal fabrication

During 3D bCC fabrication macro-sized PS spheres were seen to pack into a closed packed fcc (111) structure. The resulting closed packed structure can be affected by temperature during CC formation [157]. For example Cong *et al.* determined that lower temperatures can aid the formation of a square array [158]. Therefore a

temperature of 45ºC was employed throughout this work. Equal volumes of micron and nanometre sized PS sphere suspensions were premixed and homogenised through vigorous manual shaking. Oxygen plasma was performed on all µfluidic chips to activate the surface of the PDMS before capillary force packing for 5 min. Oxygen plasma was performed under an atmosphere of air using a Harrick plasma cleaner (PDC-002) before the chips were placed into the PS suspension ensuring the µchannel base was immersed in the suspension. This was then heated at 45ºC for 12 h to allow PS spheres to form the bCC in the µchannel.

2.2.3.5 Preparation of tetraethyl orthosilicate (TEOS) sol-gel inverse opal

After 3D bCC fabrication in the µchannel a TEOS sol-gel inverse opal was fabricated as follows: 3 mL ethanol, 6 mL TEOS, 3 mL D.I. water and 1 mL concentrated (~37 % w/v) HCl were mixed with constant stirring for 5 min. 1 mL was poured over the µfluidic chip containing the bCC in the µchannel and cured at 65ºC for 2 h. After curing the PS sphere bCC was removed by immersion of the chip in toluene and the TEOS sol-gel imaged using SEM analysis.

2.2.3.6 UV-visible spectroscopic analysis of 3D CC in PDMS micro-channels

UV-visible results were obtained using an Ocean Optics UV-visible spectrophotometer with spectra suite software. A 400 µm fibre beam width was used to measure each sample in triplicate. The PDMS micro-chip with micro-channel of dimensions 220 µm width x 60 µm depth containing no CC, uCC or bCC crystals were each 4 mm thick, 12 mm wide and 40 mm in length.

2.3 Results and Discussion

During preliminary unimodal PS CC packing of unmodified PS suspensions (i.e. used as received, without anionic surfactant removal); the presence of anionic surfactant had a dramatic effect on the final order of PS CC in the μchannel, resulting in increased disorder. To investigate the disorder observed, anionic surfactant was removed from the PS sphere suspension by centrifugation and PS suspensions were re-dispersed in varying concentrations of SDS from 0 – 0.1 % w/v. Capillary force packing was used to form CC in the confines of the μchannel over 12 h at 45ºC. A uniform CC was formed at 0 % w/v SDS as shown in Figure 2.1A. Utilising a PS suspension containing 0.01 % w/v SDS, a crystalline structure was again evident through the PS CC formed, although with a decrease in order evident at increased magnification (Figure 2.1B inset). SDS was observed to have crystallised within the μchannel during PS sphere packing, Figure 2.1B, with the disruption of the unimodal CC formation attributable to these SDS crystals. SDS concentration was increased further to 0.1 % w/v; the resulting PS CC template displayed a further increase in disorder. Once again crystallisation of SDS in the μchannel during capillary force packing occurred, Figure 2.1C with larger areas of disorder in CC structure noted in comparison to 0 % and 0.01 % w/v SDS, Figure 2.1C inset.

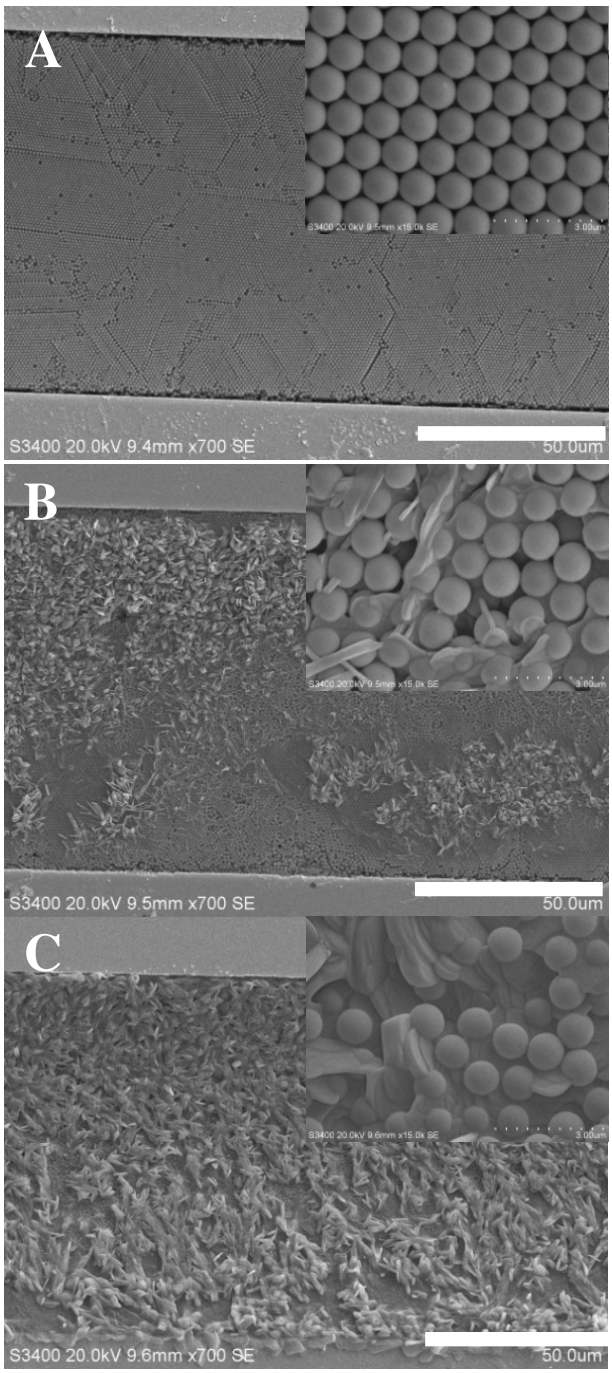

Figure 2.1: SEM image of PS sphere packing resulting from immersion in suspensions containing 1 µm PS spheres and SDS with concentrations ranging from A) 0 % w/v SDS, inset increased magnification of ordered PS packing; B) 0.01 % w/v SDS, inset increased magnification of disordered PS packing; C) 0.1 % w/v SDS, inset increased magnification of disordered PS packing. Mag. 700; scale bar: 50.0 µm. Inset Mag. 15.0 k; scale bar: 3.00 µm.

Each of the PS CC's was washed in D.I. water for 30 seconds to remove crystallised SDS from the μchannel. The resulting CC structures are illustrated in Figure 2.2. The PS CC containing no SDS remained uniform with no significant effect noted after washing in D.I. water. However, as SDS concentration was increased the washed PS CC showed increasingly more disorder, Figure 2.2B and C. Additionally, during washing, large sections of the CC collapsed as SDS was removed, presumably due to the removal of the SDS scaffold supporting the CC structures. Upon removal of SDS these CC areas collapsed, resulting in a further increase in observed disorder. An indicative section of collapsed CC is shown in Figure 2.2C circled in red.

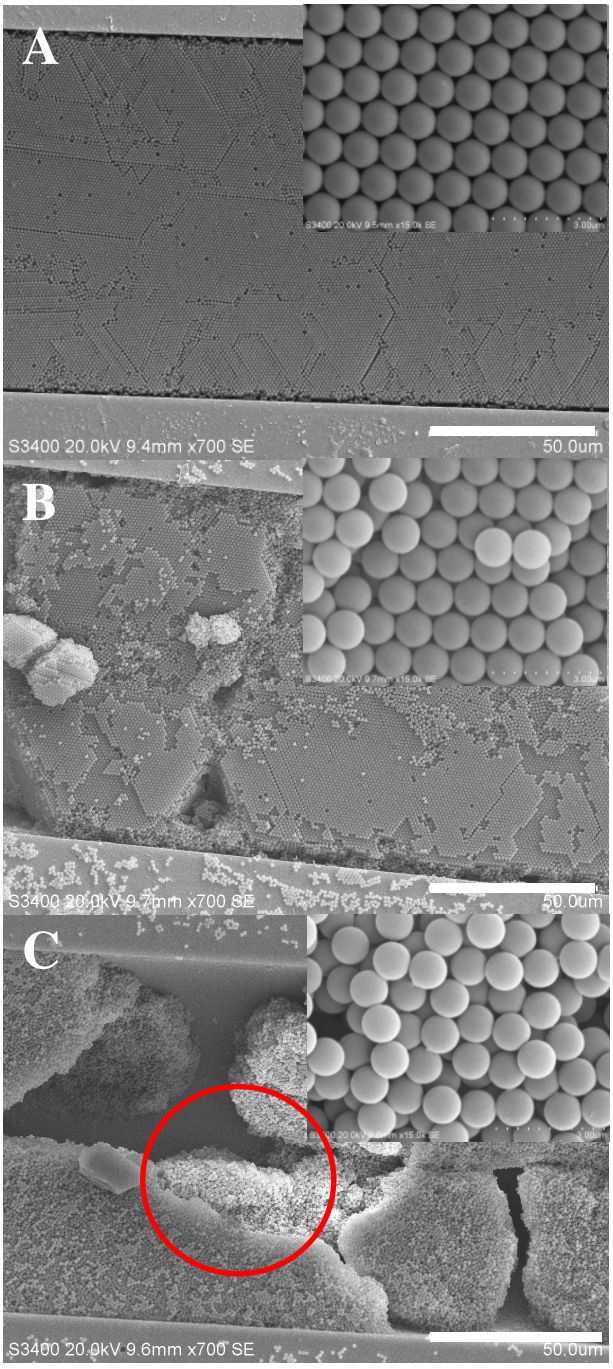

Figure 2.2: SEM image of PS sphere packing resulting from immersion in solutions containing 1 µm PS spheres and varying concentrations of SDS after washing in D.I. water. Initial SDS concentrations of A) 0 % w/v SDS, inset increased magnification of ordered PS packing; B) 0.01 % w/v SDS, inset increased magnification PS packing with increased disorder; C) 0.1 % w/v SDS, inset increased magnification of PS packing with high levels of disorder. Mag. 700; scale bar: 50.0 µm. Inset Mag. 15.0 k; scale bar: 3.00 µm.

As a result of the disorder noted with anionic surfactant present in PS suspensions, Figure 2.1, during 3D PS bCC templates fabrication, surfactant-free PS suspensions were exclusively used. Figure 2.3 shows a schematic representation of the mechanism of bCC formation. Figure 2.3A illustrates a typical µchip 20 mm x 45 mm, containing a µchannel of dimension 40 mm length x 0.110 mm width x 0.050 mm depth, immersed in a mixed PS sphere suspension so that the lowest (approx. 5 mm length) of the µchannel was submerged. This suspension comprised spheres of both 1 µm and 200 nm diameter, in varying $VF_{S/L}$ ratios, as discussed below.

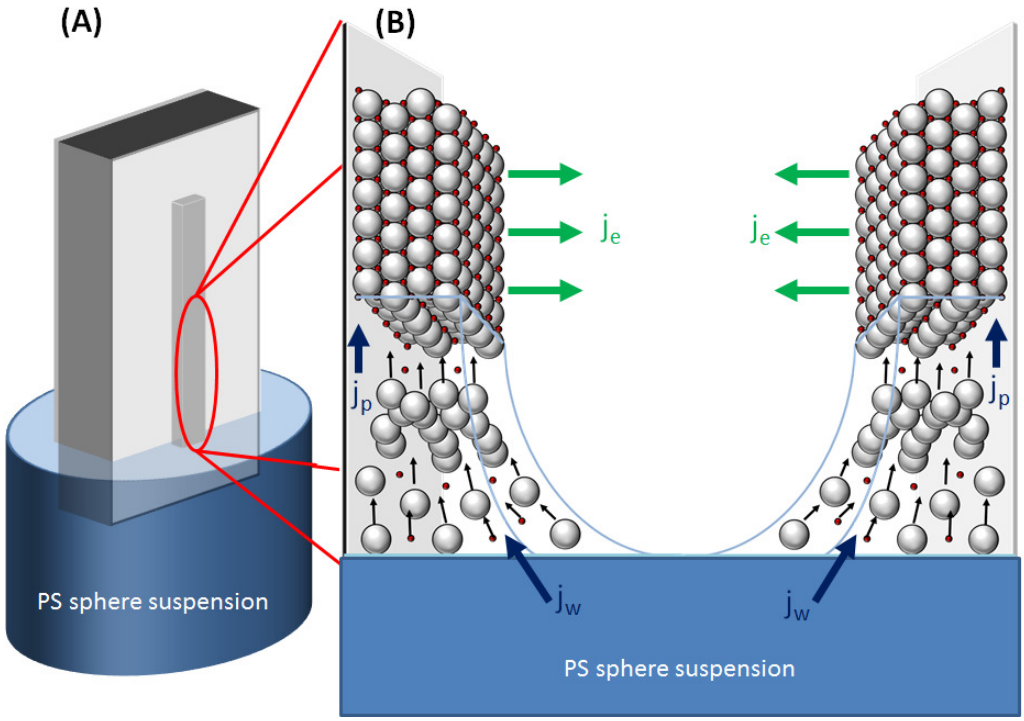

Figure 2.3: Schematic diagram illustrating A) microfluidic chip with channel, partially submerged in PS sphere suspension and B) expanded schematic of crystal growth formation supported on the two side walls of the channel, reproduced from Ko and Shin [32]. Evaporation of solvent, water evaporation flux (j_e), is represented by green arrows, while water flux (j_w) and particle flux (j_p) are illustrated with blue arrows (schematic not to scale).

As shown in Figure 2.3, capillary flow draws the suspension up the μchannel, with the two side walls of the μchannel acting as independent surfaces to support CC assembly as discussed by Ko and Shin [32]. When evaporation begins the concentration of PS spheres in the μchannel gradually increases. Initially macro-sized PS concentration was 1 % w/v in solution but due to evaporation flux, PS concentration in the μchannel began to rise. As the PS sphere concentration increases, the PS spheres are drawn into a close-packed structure by capillary forces, initially at the edge of the μchannel before moving towards the centre of the μchannel over time. Similarly to evaporation-induced co-operative hierarchical self-assembly (EICSA) in dip-drawing, both the macro- and nano-spheres are drawn towards the growth front at the top of each side wall, initially with the same velocity. The larger spheres, which are also in greater concentration, pack in an fcc arrangement, with successive layers forming inwards from the μchannel side walls towards the centre of the μchannel, as shown in Figure 2.3B. Nano-spheres easily move through the macro-sphere structure, drawn by j_w, filling the tetrahedral and octahedral voids of the fcc structure.

The independent parallel growth of the fcc crystal at the two side walls of the μchannel in the μfluidic chip is illustrated by the schematic at time t1 in Figure 2.4. At a certain time point in the dual parallel growth of the bCC at both side walls of the μchannel, the solvent front of both walls overlaps, creating a liquid meniscus which joins both crystals. This creates a new solvent front for evaporation-induced crystal growth, causing the crystal to be formed from the side walls into the centre of the μchannel and from the bottom of the μchannel up towards the centre, as illustrated in the schematic at time t2 in Figure 2.4.

CC growth continues until PS concentration reaches 100 % in channel at which point all the solvent, in this case water, has been evaporated and the CC is fully formed. During solvent evaporation PS sphere concentration is replenished by j_w and j_p from the colloidal suspension allowing continuous CC formation throughout the entire µchannel depth. This multidirectional growth continues until the µchannel is fully packed, as illustrated by time t3 in Figure 2.4. SEM images of the µchannel at time t1 and time t2 are shown in Figures 2.5A and B respectively.

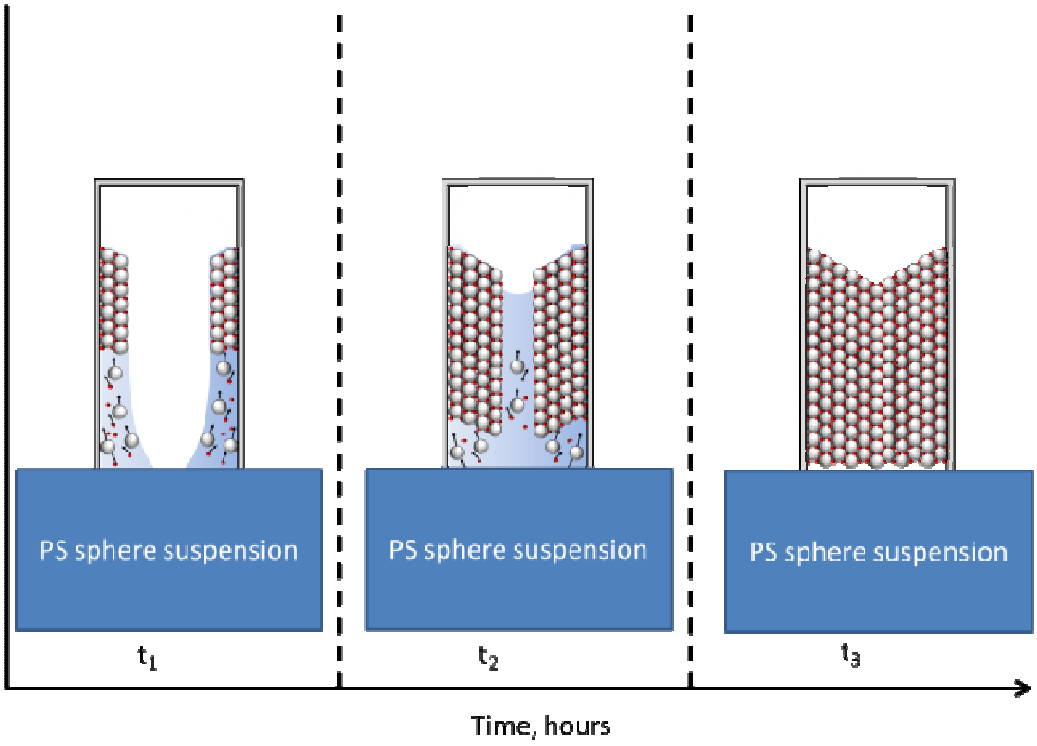

Figure 2.4: Crystal growth schematic illustrating at time t1 growth of fcc from side walls inwards towards centre of µchannel; at time t2 growth from both side walls and from bottom of µchannels towards centre; and at time t3 the is µchannel filled with bCC (not to scale).

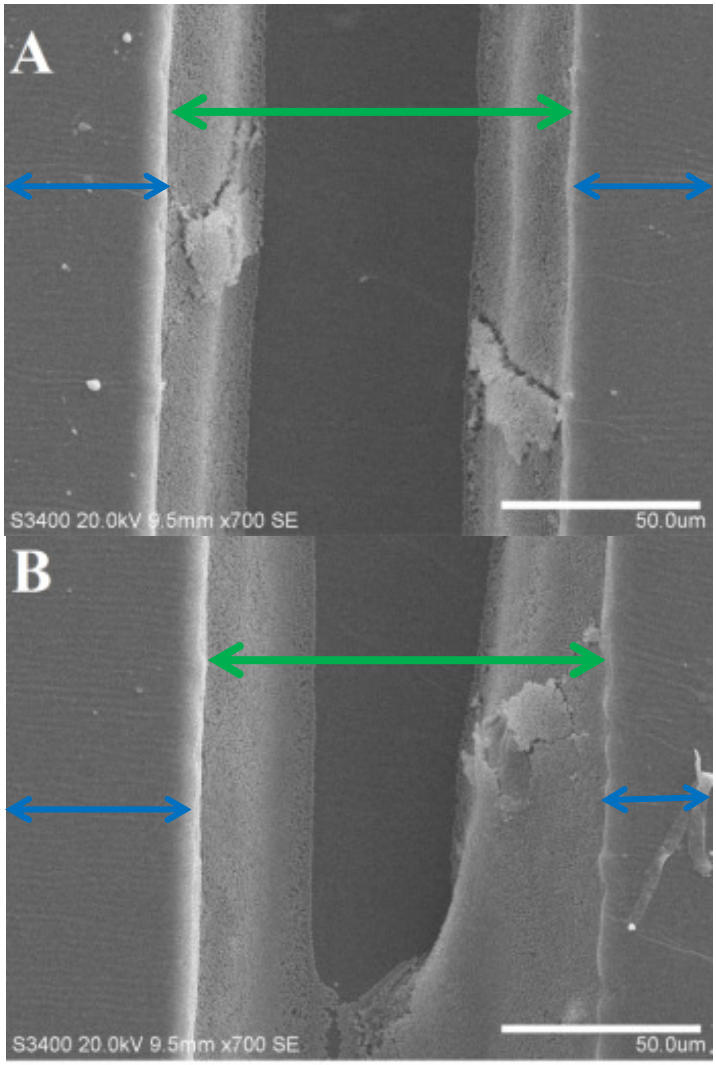

Figure 2.5: SEM image of bCC, D_S = 200 nm, D_L = 1 µm and $VF_{S/L}$ = 0.1, showing bCC formation. The µchannel is illustrated with a green arrow, while the PDMS support is shown with blue arrows. A) Dual CC growth supported by the side walls of the µchannel after 8 h packing, and B) movement of particles towards the centre of the µchannel as PS concentration increases with continuous CC growth, after the solvent fronts have joined to create a meniscus between the two CCs growing on the side walls after 10 h packing. Mag: 700; scale bar 50.0 µm.

Typically bCC formation was completed after 12 h using the conditions described in the Methods Section 2.2.3.4. To visually illustrate the formation process, bCC fabrication was stopped after 8 & 10 h allowing bCC growth to be imaged via SEM

analysis. To demonstrate that the two-step bCC fabrication was also possible over wider geometric areas, µchannel widths of 180 µm were used in Figure 2.5. bCC was observed to form across the entire width of the µchannel. Artefacts are noted in Figure 2.5A & B at the edge of the µchannel walls due to halting of the bCC growth prematurely resulting in areas with cracks as j_w and j_p halted after the experiment was stopped.

The number of layers (k) formed by dip-drawing methods can be determined using Equation 1 below:

$$k = \frac{\beta l j_e V F_{S/L}}{0.74048 V_w d + \Gamma'(1 - V F_{S/L})}$$

(Equation 1)

where j_e is water evaporation flux, 0.74048 is the volume occupied by a fcc sphere structure, d is particle diameter, β is the ratio between velocity of a particle in solution and fluid velocity, l is the meniscus height, Γ' is water volume flux between particles and V_w is the withdraw rate when using dip-drawing methods [32, 159]. The number of layers of bCC formed is therefore dependent on $VF_{S/L}$. In the work presented here however, the number of layers is dictated by the depth of the µchannel. This independence from $VF_{S/L}$ allows for greater control over the resulting bCC template in comparison to other techniques.

To comply with $D_{S/L}$ constraints a nano-sized PS sphere suspension of D_S = 200 nm was chosen, resulting in $D_{S/L}$ = 0.200. The number of nano-sized PS spheres occupying the interstitial voids can be influenced by $VF_{S/L}$ (the ratio of % w/v nano-sized spheres to % w/v of macro-sized spheres in solution; *e.g.* equal volumes of a

0.1 % w/v 200 nm PS sphere and a 1 % w/v 1 µm PS sphere suspension will give a $VF_{S/L}$ = 0.1). Additionally, control of $VF_{S/L}$ was shown to have a large effect on the resulting bimodal PS template [128-130]. By optimising $VF_{S/L}$, within an appropriate range, control and manipulation of the number of nano-sized spheres packed within interstitial voids is possible [132, 160]. It has previously been demonstrated that a practical working range was between $0.001 < VF_{S/L} < 0.1$ [135]. As a result $VF_{S/L}$ within this range was chosen and the resulting structures investigated to assess fabrication of reproducible PS bCC templates and to demonstrate the range of $VF_{S/L}$ ratios which can result in ordered bCCs.

Variation and optimisation of $VF_{S/L}$ can allow for the fabrication of different LS_n packing structures. Through manipulation of $VF_{S/L}$ (whilst maintaining $D_{S/L}$ = 0.200) variations in the number of nano-sized PS spheres packed within the interstitial voids created by three adjacent macro-sized PS spheres was achieved, therefore providing for variation in LS_n structure. Examples of potential theoretical LS_n structures are shown in Figure 2.6. Figure 2.6A shows an example of an LS_2 structure (theoretical definition where structures consist of macro-sized (L) spheres and nano-sized (S) in a 1:2 ratio) which has one nano-sized PS sphere packed within the interstitial void created by three adjacent macro-sized PS spheres. Figure 2.6B shows an example of an LS_4 structure. The LS_4 structure (L:S 1:4) is more complex with variation in the number of nano-sized PS spheres packed, from one to three, within each interstitial void. Finally Figure 2.6C shows an example of an LS_6 structure (L:S 1:6); here three nano-sized PS spheres are packed within each interstitial void site. Other LS_n structures have been reported by researchers including LS_3 and LS_5 with the potential to continue as high as LS_{17}. However, most reported LS_n structures have been fabricated in monolayer at the air water interface. Due to the high complexity of the

resulting structures, multi-layered bCC's with high LS_n structures are extremely difficult to fabricate with poor reproducibility and uniformity noted [135, 161]. LS_2 structures (one nano-sized PS sphere in each interstitial void) and LS_6 structures (3 nano-sized PS spheres in each interstitial void) were chosen to demonstrate ordered bCC structure formation. The LS_2 and LS_6 fabrication parameters are detailed in Table 2.2.

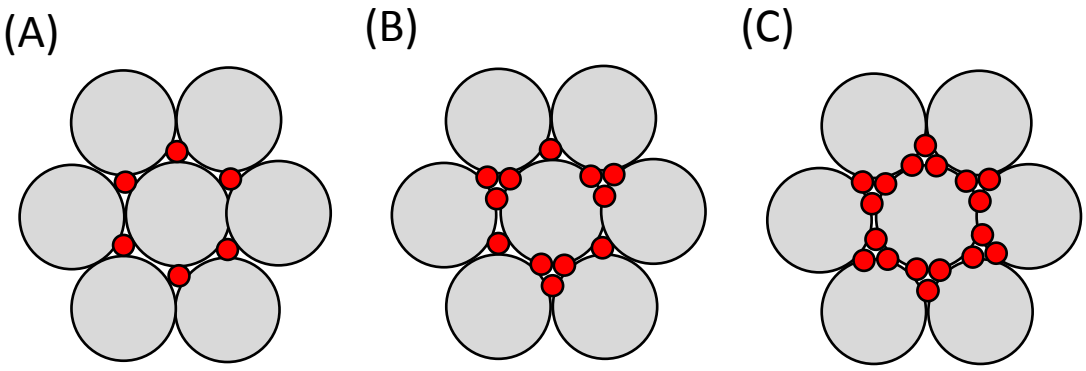

Figure 2.6: Schematic diagram showing examples of theoretical LS_n structures (A) LS_2 structure, (B) LS_4 structure and (C) LS_6 structure, reproduced from Ref 30 [135].

Table 2.2: Parameters of bimodal PS sphere suspensions used during bCC formation.

LS_n structure	***LS_2***	***LS_6***
Large sphere diameter D_S (nm)	1000	1000
Large sphere volume VF_S (% w/v)	1	1
Small sphere diameter D_S (nm)	200	200
Small sphere volume VF_S (%)	0.001	0.1
Diameter size ratio $D_{S/L}$	0.200	0.200
Volume fraction ratio $VF_{S/L}$	0.001	0.1

Figure 2.7 shows the top surface of an LS_2 structure in the μchannel. The structure showed uniformity in macro-sized PS sphere packing with interstitial voids filled with single nano-sized PS spheres, shown in Figure 2.7. Complete fabrication of the repeating structure of one nano-sized PS sphere present in each interstitial void was not achieved throughout the structure with order noted over lengths of 20 – 30 μm before defects were noted. Pockets of low uniformity were noted in the structure with packing of nano-sized PS spheres inconsistent between individual interstitial voids. The $VF_{S/L}$ required for this structure at $VF_{S/L}$ = 0.001 was so low that there were insufficient 200 nm spheres in the packing solution volume available to pack all interstitial voids. (An increase in $VF_{S/L}$ was not carried out, as it was expected to result in a hybrid LS_n structure, as discussed by Dai *et al.*) [135].

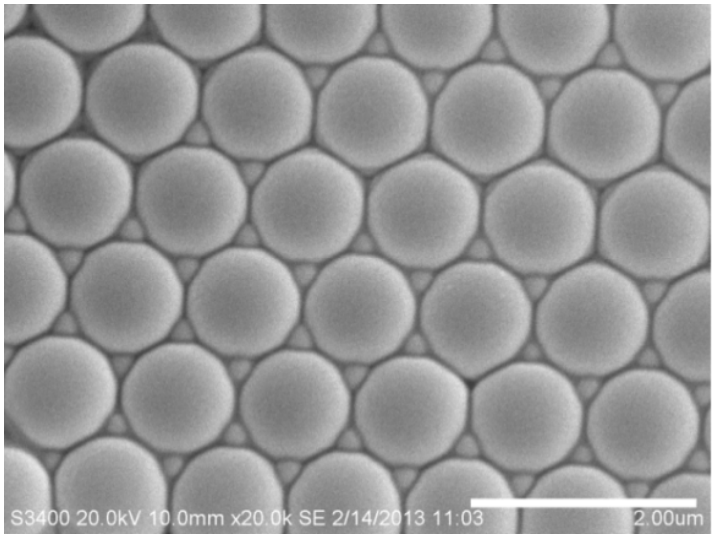

Figure 2.7: Top view of bimodal PS LS_2 bCCs of macro- (D_L = 1 μm) and nano-sized (D_L = 200 nm) PS spheres, $VF_{S/L}$ = 0.001 section of LS_2 structure. Mag: 20 k; scale bar: 2.00 μm.

To examine if the LS_2 structure was confined to the surface of the CC, or was representative of the structure throughout the 3D crystal, an inverse opal of the crystal was obtained using a TEOS sol-gel, with results indicated in Figure 2.8.

Figure 2.8A illustrates the structure at low magnification, with the 3D macro-porous honeycomb-like structure clearly evident. On increasing magnification, several successive layers of ordered fcc crystal can be seen, demonstrating the consistency of the macro-porous structure, Figure 2.8B. Increasing the magnification of the middle internal layers of the structure illustrated in Figure 2.8B results in images typical of those illustrated in Figures 2.8C & D, where the bimodal structure is clearly evident. Examples of meso-pores formed by nano-sized spheres in the original bCC are circled in red while macro-pores formed as a result of the interconnecting macro spheres are circled in green.

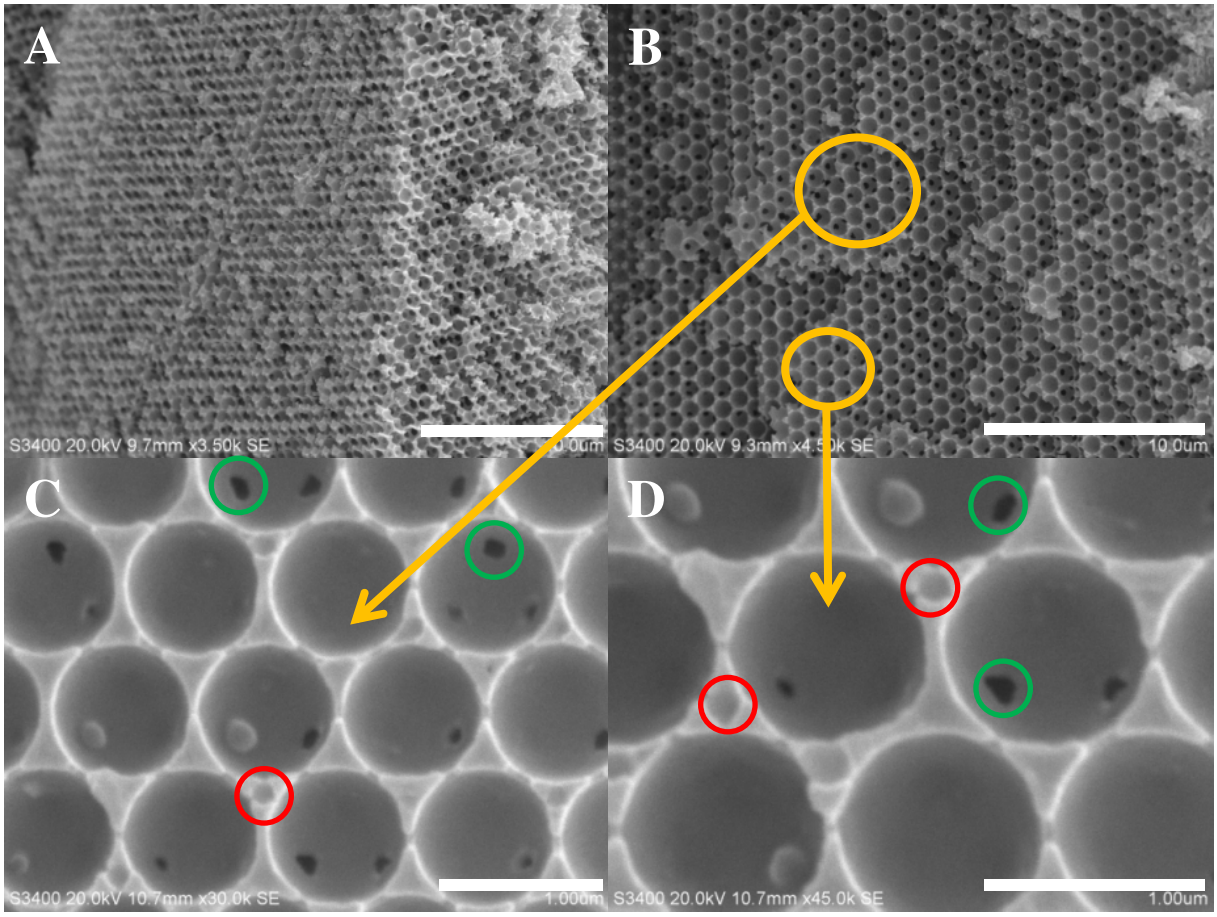

Figure 2.8: SEM images showing 3D TEOS sol-gel inverse opals of bCC macro- (D_L = 1 µm) and nano-sized (D_L = 200 nm) PS spheres with $VF_{S/L}$ = 0.001. A) Mag: 3.50

k; scale bar: 10.0 µm. B) Mag: 4.5 k; scale bar: 10.0 µm. C) Mag: 30.0 k; scale bar: 1.00 µm. D) Mag: 45.0 k; scale bar: 1.00 µm. Note; pores resulting from macro-sized spheres are circled in green and pores resulting from nano-spheres are circled in red.

An increase in $VF_{S/L}$ to 0.1 theoretically should result in an LS_6 structure. The reproducible fabrication of a bCC template with LS_6 structure was achieved with $VF_{S/L}$ = 0.1, Figure 2.9. The macro-sized PS spheres were shown to pack in a reproducible close pack structure with three nano-sized PS spheres placed in each interstitial void.

While the bCC LS_6 structure was highly ordered, some structural defect pockets were noted between ordered areas. These consisted of empty interstitial voids, or empty macro-sized PS sphere sites. Comparable defects resulting from self-assembly methods are routinely detected in 2D bCC arrays, with best technical practice minimising but not eliminating defects completely [162-164]. For CC structures fabricated from soft micro-gel spheres, a decrease in crystallinity with addition of small spheres to induce a binary structure was observed, but not quantified [165]. In this work, in the fabricated LS_6 structure order was observed over lengths of approx. 100 – 150 µm within the crystal, comparable to 2D bCC structures. Overall however, reproducibility and order was increased for the LS_6 structure in comparison with the LS_2 structure with order noted over significantly larger areas.

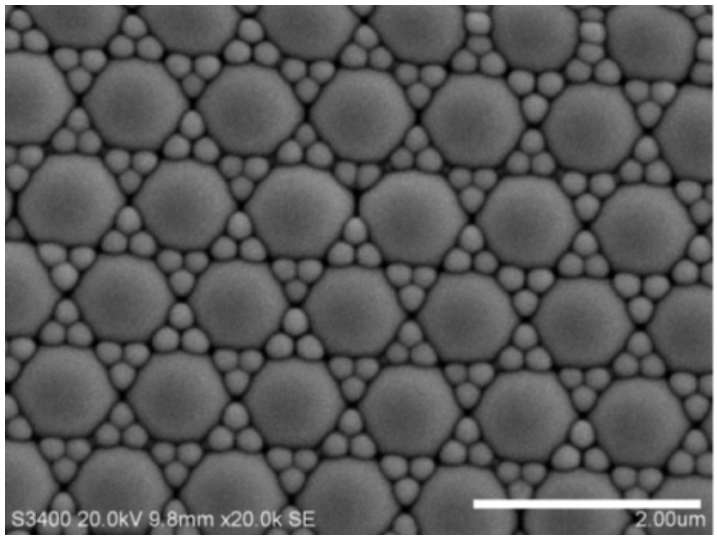

Figure 2.9: Top view of LS_6 PS bCCs of macro- (D_L = 1 µm) and nano-sized (D_L = 200 nm) PS spheres with $VF_{S/L}$ = 0.1. Mag: 20 k; scale bar: 2.00 µm.

Again, to illustrate that the bCC structure was not confined to the top of the crystal surface, an internal cross section of the PS bCC structure after removal from the µchannel were obtained Figure 2.10A and B. 3D order was shown through the multi-layer LS_6 structure via the resulting cross section, with 3 nano-sized PS sphere present in each interstitial void, Figure 2.10A and B. TEOS inverse opal structure of the PS bCC LS_6 structure Figure 2.10C and D were obtained with connection between layers evident with flow through pores (circled in green) as a result of interconnecting macro-spheres shown in Figure 2.10D, while the bimodal character within the 3D cross structure was illustrated with mesopores (circled in red) evident in multiple layers of the structure, shown in Figure 2.10D. Pores are grouped in sets of 3, the inverse of the bCC which had 3 nano-spheres in each interstitial void, maintaining LS_6 structure throughout.

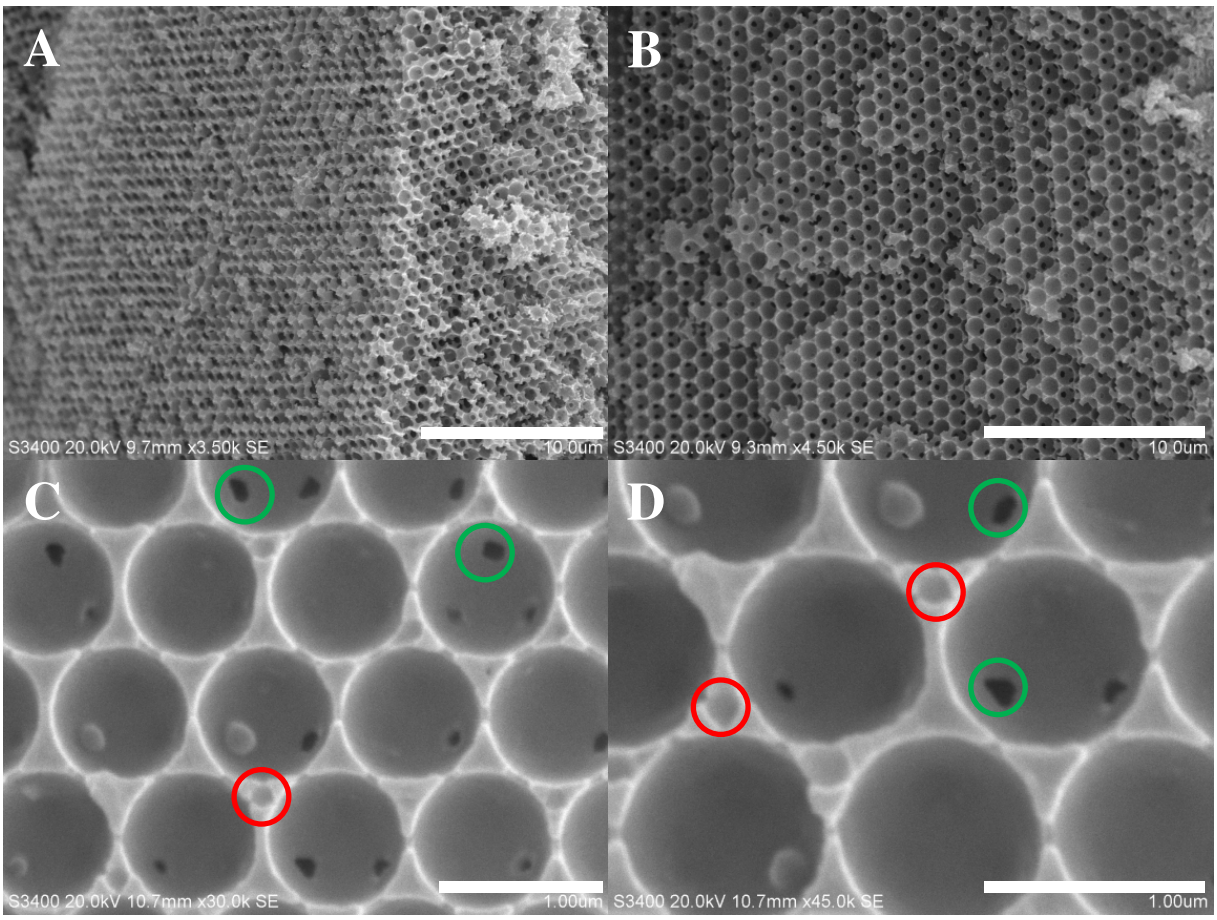

Figure 2.10: SEM images A) illustrates PS bCC LS_6 structure of macro- (D_L = 1 µm) and nano-sized (D_L = 200 nm) PS spheres with $VF_{S/L}$ = 0.1. Mag 2.50 k; scale bar 20.0 µm. B) PS bCC TEOS sol-gel cross section at higher magnification. Mag 15.0 k; scale bar: 3.00 µm. C) bCC cross section of PS bCC. Mag: 5.00 k; scale bar: 10.0 µm. D) High magnification of TEOS sol-gel inverse opal. Mag: 20.0 k; scale bar: 2.00µm. Note; pores resulting from macro-sized spheres are circled in green and pores resulting from nano-sized spheres are circled in red.

Optical spectroscopy was also utilised to characterise the 3D bCC template. A 400 µm fibre beam width was used to measure the light intensity which passed through empty PDMS micro-channels, as well as uCC and bCC crystals fabricated within these micro-channels. As the spectroscopic beam was 400 µm in width, the micro-

channel width was extended to 220 µm to maximise the proportion of the beam which passed through the channel, and where incorporated, the CC. As shown in Figure 2.11, the highest light intensity was observed for the empty micro-channel, as expected. On incorporation of a 1 µm PS sphere CC, there was a decrease in light intensity, again as expected, due to the presence of the PS CC. On incorporation of a bCC comprising 1 µm and 200 nm PS spheres, there was a further significant decrease in light intensity, due to the increased PS sphere volume fraction within the channel. Nano-sphere incorporation within the interstitial voids throughout the CC would be required to result in an increase in volume fraction sufficient to reduce the light intensity to the extent observed.

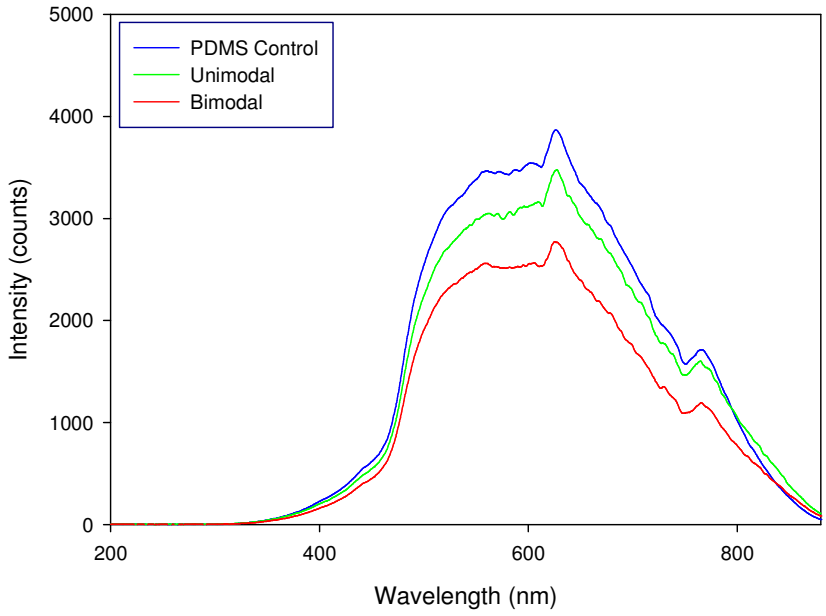

Figure 2.11: Intensity of light passing through an empty PDMS µchannel (shown in blue), µchannel incorporating a uCC (1 µm macro-sized PS spheres, shown in green) and µchannel incorporating a bCC (1 µm macro and 200 nm nano-sized PS spheres, shown in red). µchannel was of dimension 220 µm width x 60 depth, and optical measurements were carried out with a 400 µm beam width.

After UV studies were performed the time taken to flow through the uCC and bCC structures were compared in sealed PDMS μchannels. Time taken for D.I water to pass successful through an empty PDMS channel, a PDMS channel packed with a uCC and bCC (LS_6) 60 μm in depth and 10 mm in length were compared. Flow rate was maintained at a nominal 0.1 μL/min using a syringe pump, with the time taken for flow through measured. The back pressure generated by flowing through a packed bed was not measured, but it was expected that an increase in back pressure would result in a reduction in the actual flow rate achievable by the syringe pump. Therefore in contrast to what would be expected for a more sophisticated pumping system, such as a HPLC pump, the more densely packed channels were expected to fill more slowly, in spite of having a lower void volume throughout the channel. For the empty μchannel flow through was completed after 34±7 s. Upon addition of a uCC in channel flow through time increased to 79±26 s. Finally bCC flow through time was measured at 170±14s. The increase in time taken to pass through the structures therefore supported the hypothesis that there was an increased volume of spheres within bCC packed channels, and accordingly a decreased void volume remaining in these channels. (It should be noted that this experiment was a proof of concept experiment, and did not explore if flow through or eddy channels exist within the sealed channels.)

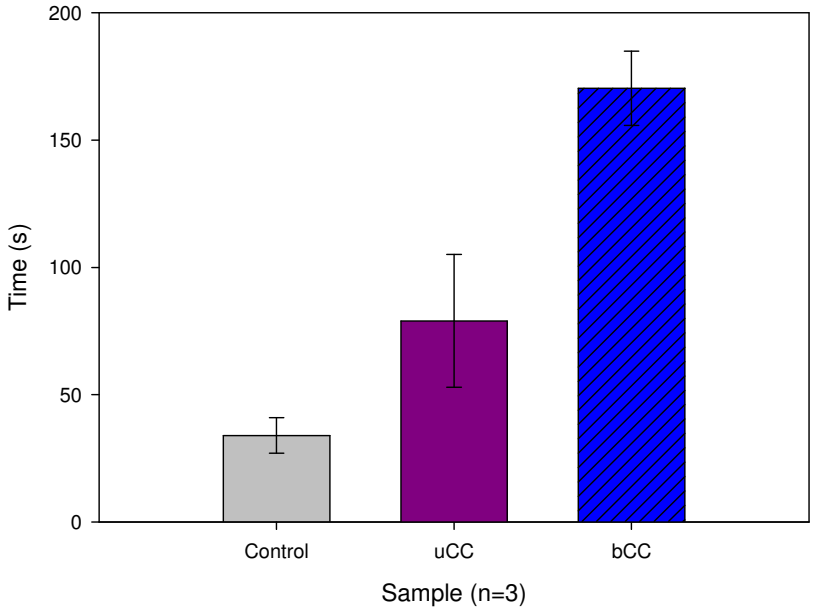

Figure 2.12: Time taken to for deionised water to flow through A) an empty PDMS μchannel sealed to a glass slide at 0.1 μL/min shown in grey, B) a uCC packed in channel depth 60 μm length 10 mm shown in purple and C) a bCC packed in channel with depth = 60 μm and length = 10 mm shown in blue.

2.4 Conclusion

The successful fabrication of 3D ordered bCC PS templates in defined geometric areas is demonstrated here. During fabrication of 3D bCC templates, control of resulting structures was shown through manipulation of $VF_{S/L}$ and $D_{S/L}$. At low $D_{S/L}$, below $D_{S/L} = 0.150$, bCC templates were prone to areas of disorder due to free packing of nano-sized PS spheres within the channel and tetrahedral/octahedral voids, disrupting macro-sized PS sphere close packing. To control the packing of nano-sized PS spheres within only the interstitial voids, the $D_{S/L}$ was controlled within a range of $0.150 \leq D_{S/L} \geq 0.225$.

Control of nano-sized PS sphere packing was achieved within the interstitial voids, along with the manipulation of nano-sized PS sphere number in each interstitial void. Through increases in $VF_{S/L}$ from 0.001 – 0.1 the packing of nano-sized PS spheres was increased from one to three in each void. At low $VF_{S/L} = 0.001$ an LS_2 structure was formed in channel. With $VF_{S/L} = 0.1$ the fabrication of an LS_6 structure was achieved with a marked increase in reproducibility and reduction in defect number when compared to the LS_2 structure. Through investigation of the sol-gel inverse structure, the 3D structure was investigated, and the bimodal properties of the crystal were shown to be present both on the surface and within the structure.

The packing method presented allows for 3D bCC formation in a defined geometric space (μchannel) in a one-step process, independent of $VF_{S/L}$. Template thickness is reproducible and is accurately controlled by the depth of the μfluidic channel itself. The benefits of this method are the independence of CC thickness from $VF_{S/L}$, ease of fabrication, high uniformity and 3D order of final PS templates. The capillary force packing method developed in this work offers for the first time a method to fabricate uCC and bCC structures specifically within a μchannel unlike other

methods such as drop casting, spin coating and dip-drawing which are designed for CC fabrication on planar substrates. Many potential analytical applications in LOC designs and separation science are available for templates of this nature.

Chapter 3

Electrochemically Polymerised Inverse-Opal Conducting Polymer Structures in μfluidic Channels

3.1 Introduction

Electrochemical polymerisation offers a unique method to tailor the polymerisation of intrinsically conducting polymer (ICP) materials on specific surfaces. The main requirement during electrochemical polymerisation is stability of electrode material in acidic media. Acid pH is required to ensure solubility of monomer and generation of the most conducing form (*e.g.* Emeraldine Salt form of PANI) [166]. During electrochemically polymerisation the application of a constant potential is routinely used to oxidise monomer units forming the aniline radical cation [167]. The mechanism of electrochemical polymerisation of aniline is detailed in Scheme 3.1. Step 1 is formation of a radical cation due to oxidation on the electrode surface, step 2 coupling of radicals with elimination of two protons. Step 3 is oxidation of the dimer formed and coupling to a radical cation causing chain propagation and finally step 4 illustrates the conversion between the doped and dedoped PANI Emeraldine Salt/Base forms. Step 1, radical formation is deemed the rate determining step of the electrochemical polymerisation of aniline. Polymerisation of aniline is also a self-catalysing process which means the more polymer that is formed the higher the rate of polymerisation [167]. The benefit of using electrochemical polymerisation is the added control during polymerisation with variation in time and/or monomer concentration resulting in thicker/thinner films over controlled areas (i.e. the electrode area placed in the monomer solution). Another significant benefit of electrochemical polymerisation is the addressability resulting from deposition onto an electrode material. As a result of this addressability application of electrochemically polymerised ICP films in drug delivery systems (DDS) [19-21], micro-extraction [168, 169] and electrochemically modulated separations [12, 13]

have been reported with electrochemical addressability being a distinct advantage in each case.

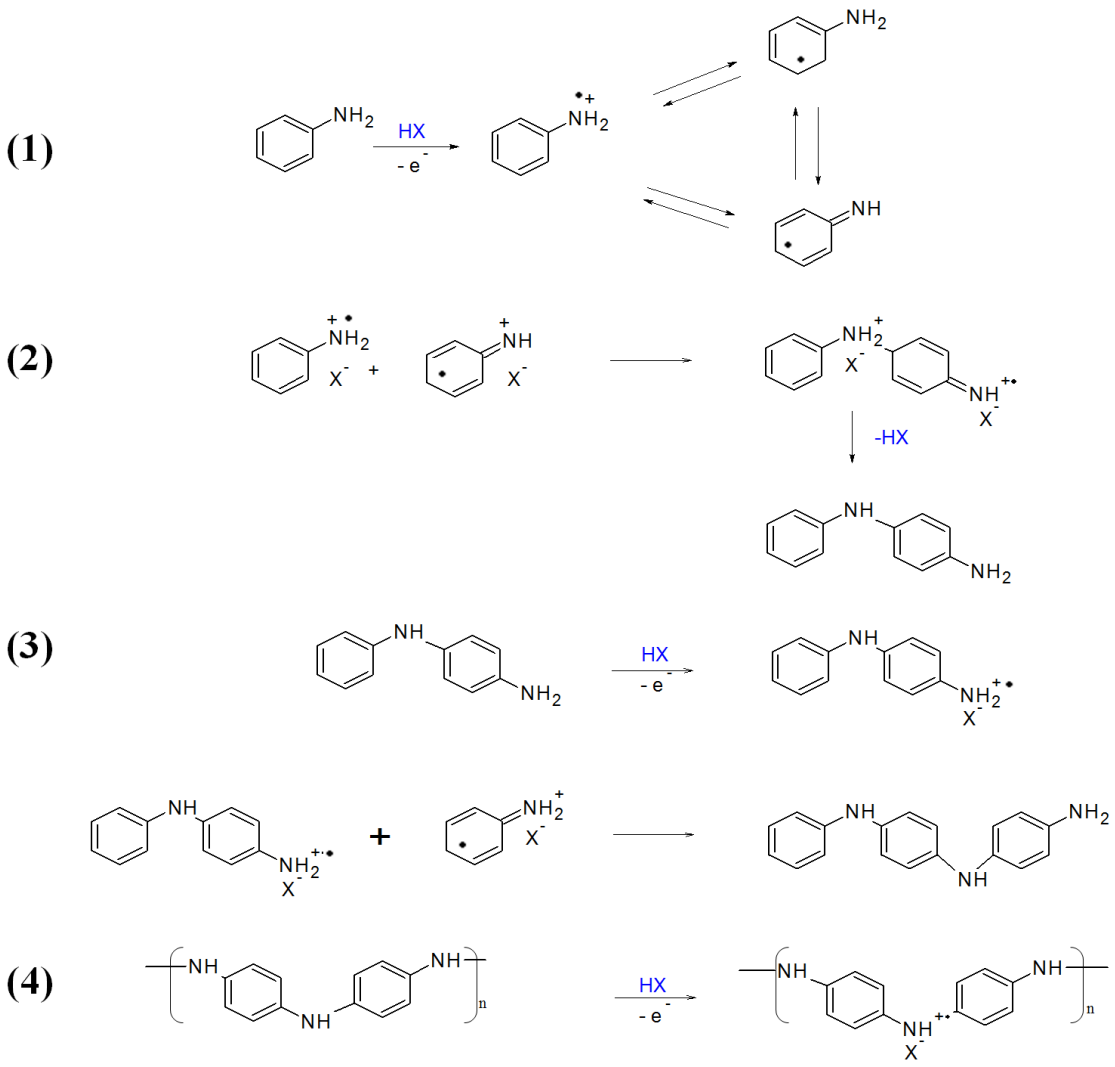

Scheme 3.1: Mechanism of electrochemical polymerisation of aniline showing 1) initiation radical formation, 2) propagation: coupling of radicals, 3) chain propagation and 4) final dedoped/doped polyaniline polymer chains, where X^- denotes the dopant [167]. In this case, the dopant is chloride.

Control over the final structure of electrochemically polymerised ICP films has been reported on planar substrates through hard templating to increase the resulting ICP film surface area. The specific applications for these high surface area materials

include energy storage and conversion [170], biosensing [171-174] and controlled drug release [18, 175, 176].

An example of ICP templating during electrochemical polymerisation was shown by Bartlett *et al.* [177]. ICP growth was achieved electrochemically through a polystyrene (PS) colloidal crystal (CC). Here, a three-electrode cell consisting of a gold working electrode (WE), platinum counter and Ag/AgCl reference electrode were used to polymerise PANI and polypyrrole (PPY). A PS template was employed with resulting thickness from 1 – 6 sphere radii (sphere size 0.50 or 0.75 μm). The PS template was subsequently removed by dissolution in toluene. The ICP films fabricated had regular pore sizes and interconnectivity between layers. Limitations such as shrinkage and deformation of the ICP films were noted over thin films of between 0.25 – 2.25 μm thick [177]. Significantly it was shown that the PANI and PPY films were electrochemically addressable on the gold WE after polymerisation. The dissolution of PS sphere template, using toluene, did not adversely affect the electro-activity of the ICP films.

Similarly, Xu *et al.* [178] demonstrated the electrochemical polymerisation of polypyrrole (PPY) in a three-electrode cell with an indium tin oxide (ITO) WE, in sodium dodecylbenzene sulfonate (NaDBS). A PS CC consisting of 440 nm spheres was prepared via vertical deposition. The resulting thickness of the PPY inverse opal was 2 μm. The PPY inverse opal displayed reversible stop band conversion between the oxidised and neutral states. In conjunction the conductivity and the wettability of the PPY film was switchable based on oxidation state [178]. PANI electrochemically polymerised on planar ITO through a PS sphere template by Ge *et al.* [179] demonstrated that ion diffusion reversibility and ion storage were greatly improved over bulk material due to the interconnected porous structure, which benefited from

the fast penetration of ions [179]. Tian *et al.* [180] again demonstrated electrochemically polymerisation of aniline through a PS CC. Here, incorporation of dopants was shown to significantly affect the structure and the mechanical stabilities of the opaline films. The rate of polymerisation was shown to increase dramatically once polymerisation through the internal structure of the template had taken place. This was ascribed to a rapid increase of the electrochemical reaction area once the growth front of the deposited material reached the template/bulk solution interface. Finally, Santos *et al*. [181] described the controlled the fabrication of 2D ordered PPY via electrochemical polymerisation on planar substrates. Here, by controlling the charge passed during the polymerisation, the growth of PPY could be controlled leading to control over the depth and corresponding diameters of the resulting pores [181].

The examples discussed above demonstrate the ordered inverse structures of ICP materials which can be fabricated on planar substrates and the benefits associated with templating such as fast penetration of ions due to the interconnected structure [179]. However, it is critical that these structures can also be fabricated in a range of formats in order to truly realise their full potential. The μchannel is one such format that has shown potential for electrochemically active polymer films for flow through applications. It can be envisaged that 3D ordered inverse ICP structures could have numerous applications in such a format where the flow-through nature and high surface area could be exploited under flowing conditions. Achieving the desired homogeneous 3D structure of the ICP within a μchannel is required in the first instance. A limitation of the methods detailed above is the thickness of ICP films reported (1 – 5 μm thick). In this work, due to the controlled template fabrication method reported in Chapter 2, significantly thicker films can be achieved

overcoming the limitation associated with planar substrates. To achieve this a 3D ordered PS unimodal colloidal crystals (uCC) of 1 µm spheres was packed in a µfluidic channel (0.110 mm x 0.050 mm x 40 mm). Following this structurally directed electrochemical polymerisation of PANI and subsequent removal of the uCC sacrificial template was undertaken. The effect of ICP growth time on the resulting inverse opal structures on-chip was investigated. ICP growth time was shown to be critical to achieving an ordered ICP inverse opal structure with flow-through pores on-chip. The flow-through pores that are demonstrated will be critical for allowing uniform flow and facile diffusion of solution/electrolyte through the ICP-modified µchannel. The concept of growing highly controlled, uniformly porous inverse opal structures of ICPs in µfluidic channels will have future applications as intelligent materials suitable for lab-on-chip (LOC) electro-analytical applications in areas which have already seen successful applications on large substrates such as sensing [182-184], energy storage [185, 186] and extraction [187, 188].

3.2 Experimental

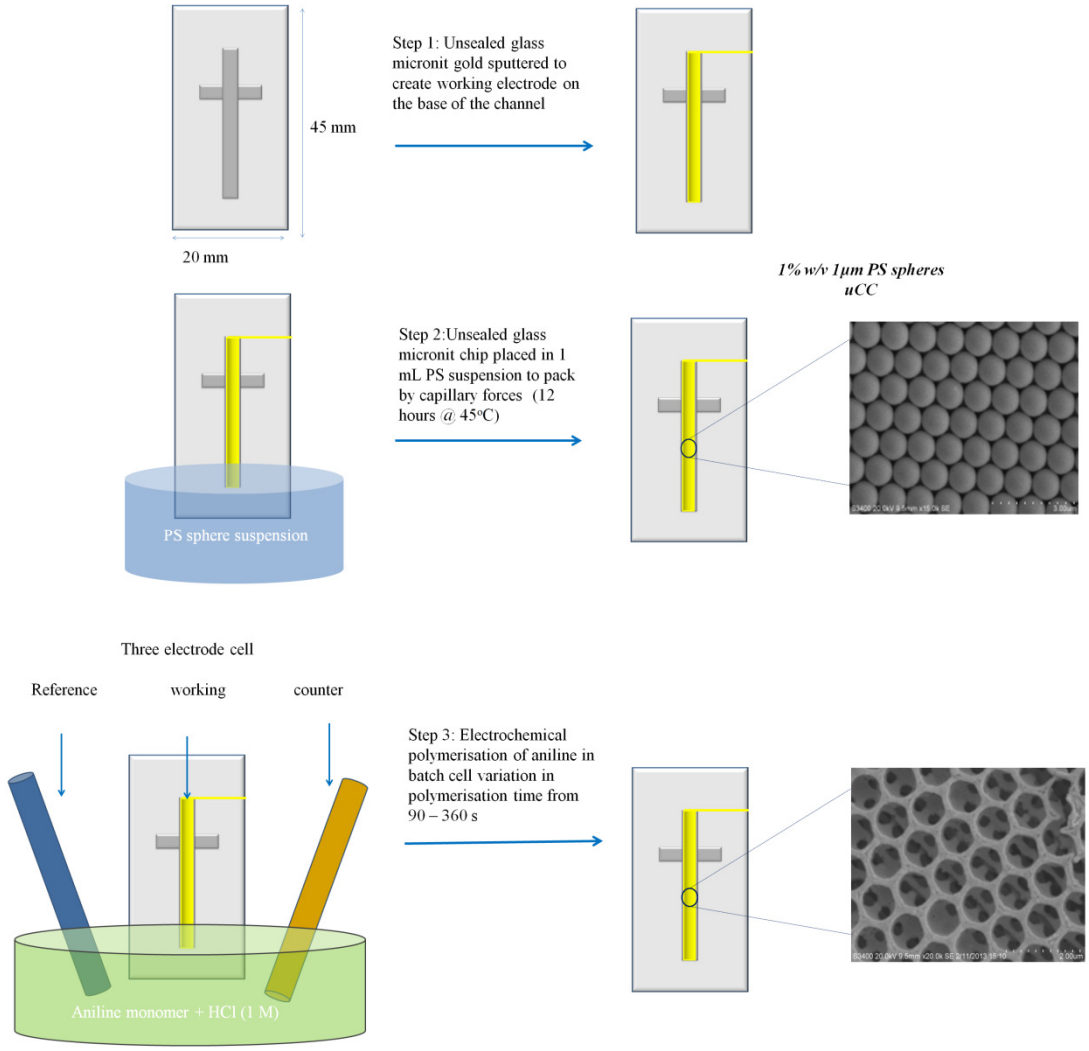

Scheme 3.2: Schematic representation of the method employed to fabricate PANI inverse opals within the depth of a µchannel.

3.2.1 Materials

As per Method Section 2.2.1 with the following addition Aniline (13, 293-4) was purchased from Sigma-Aldrich (Dublin, Ireland) and was distilled before use. The µfluidic glass chips (CU250.005) with channel dimensions of 0.11 x 0.05 x 40 mm were purchased from Micronit (USA). An Ag/AgCl reference electrode was purchased from Bioanalytical Systems, UK, and a platinum mesh (Sigma Aldrich, Dublin, Ireland) was used as the auxiliary electrode.

3.2.2 Instrumentation

As per Method Section 2.2.2 with the following addition electrochemical polymerisation and electrochemical characterisation of the PANI was carried out using a BAS 100 potentsiostat.

3.2.3 Methods

3.2.3.1 Working electrode fabrication on-chip

The µfluidic chip was masked using duct tape to isolate the µfluidic channel for gold-sputtering. The chip was then gold sputtered at 50 mA and 2 mV for 2.5 min to form the working electrode and a conducting path giving a thickness of approximately 150 nm of gold on the surface of the glass chip.

3.2.3.2 PS colloidal crystal fabrication in µfluidic channel

As per Method Section 2.2.3.1

3.2.3.3 Electrochemical PANI growth and characterisation

The electrochemical growth of PANI was carried out in the gold-sputtered µchannel over a range of times. A solution of 19.6 mL HCl (1 M) containing 400 µL (21.94 mM) of distilled aniline was used. A glass µchip containing a PS CC was placed in solution for 10 min before polymerisation to allow the aniline to permeate the PS sphere template. After this, a potential of +0.9 V vs. Ag/AgCl was applied and the polymerisation time varied over 90-360 s. After polymerisation, the PANI was allowed to air dry for 20 min before immersing the chip in toluene to remove the PS CC template (see Scheme 3.3). Upon removal of the PS template a cyclic voltammetry study was performed. CVs were run from -0.3 to +1.1 V vs. Ag/AgCl. The scan rate was 0.1 V/s in all instances, the third voltammetric cycle of each scan rate was plotted and data was extrapolated from this to plot the CV.

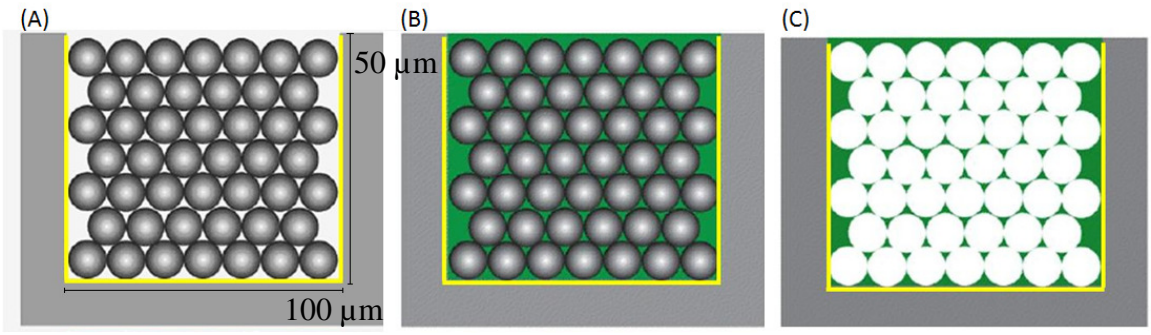

Scheme 3.3: µchannel cross section schematic of templating process in gold-sputtered µchannel: A) Deposition of PS sphere CC template by capillary force packing scale bar: channel depth 50.0 µm, channel width 110.0 µm. B) Growth of PANI through the 3D CC template. C) Removal of PS CC using toluene. A templated unimodal inverse opal PANI structure remains (Schematic of PS sphere template not to scale).

An example of a 360 s amperometric It curve is shown in Figure 3.1. The polymerisation times corresponding to specific structure are highlighted, the most fragile and collapsed structure is boxed in yellow, inverse opal structure is boxed green and bulk over growth is boxed in red.

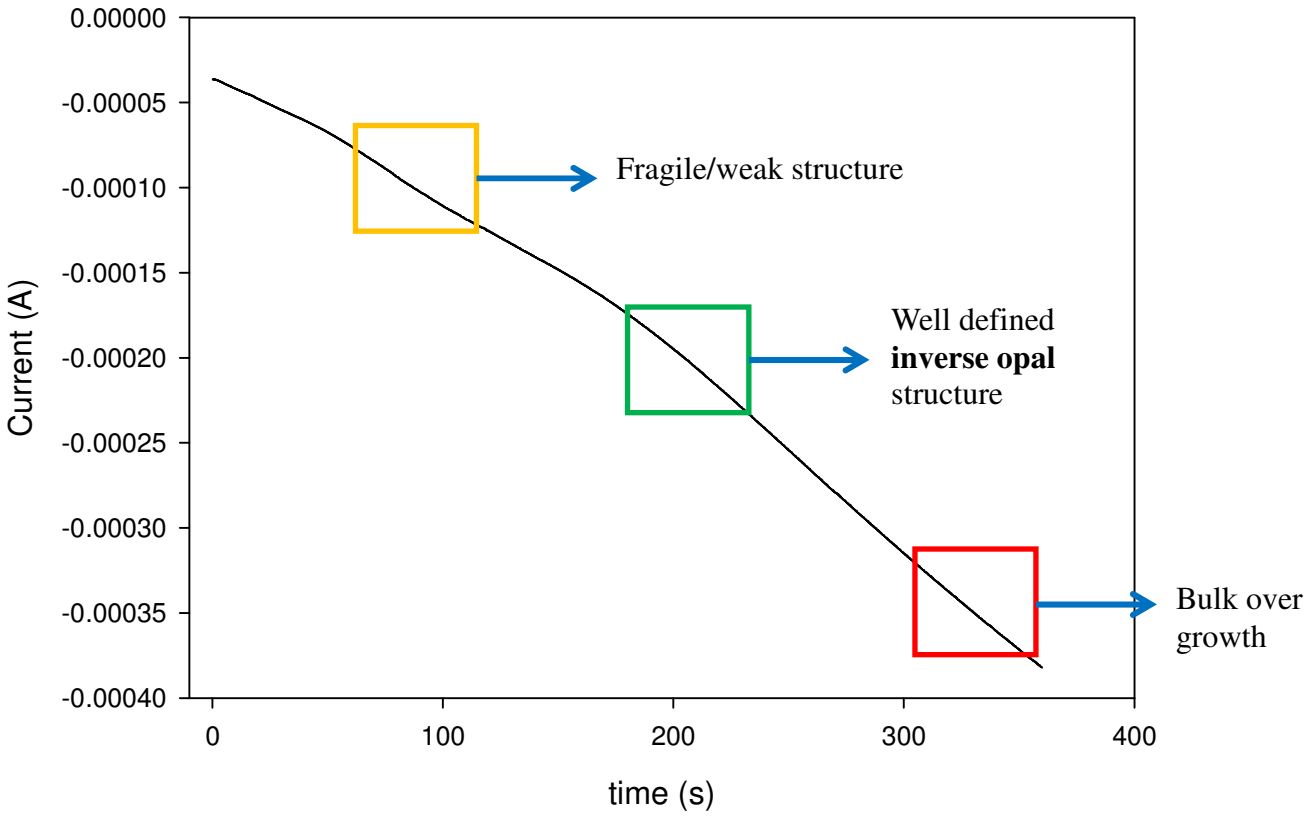

Figure 3.1: Amperometric polymerisation of aniline in HCl (1 M). 360 s polymerisation at a fixed potential of 0.9 V vs. Ag/AgCl (electrolyte 1 M HCl). Sections indicated represent the resulting inverse structure achieved ~90 s fragile structure, boxed in orange. ~210 s inverse opal structure, boxed in green. ~360 s bulk over growth, boxed in red.

3.3 Results and Discussion

Figure 3.2A shows a representative area of the resulting unimodal CC (uCC) achieved within the glass micronit chip with Figure 3.2B shows an SEM image of CC in the μchannel at higher magnification. PANI was electrochemically grown through the PS CC template as described in the Methods Section. Once polymerisation was complete, the PS sphere template was removed using toluene leaving the PANI inverse opal structure, as illustrated in the fabrication steps demonstrated in Scheme 3.3.

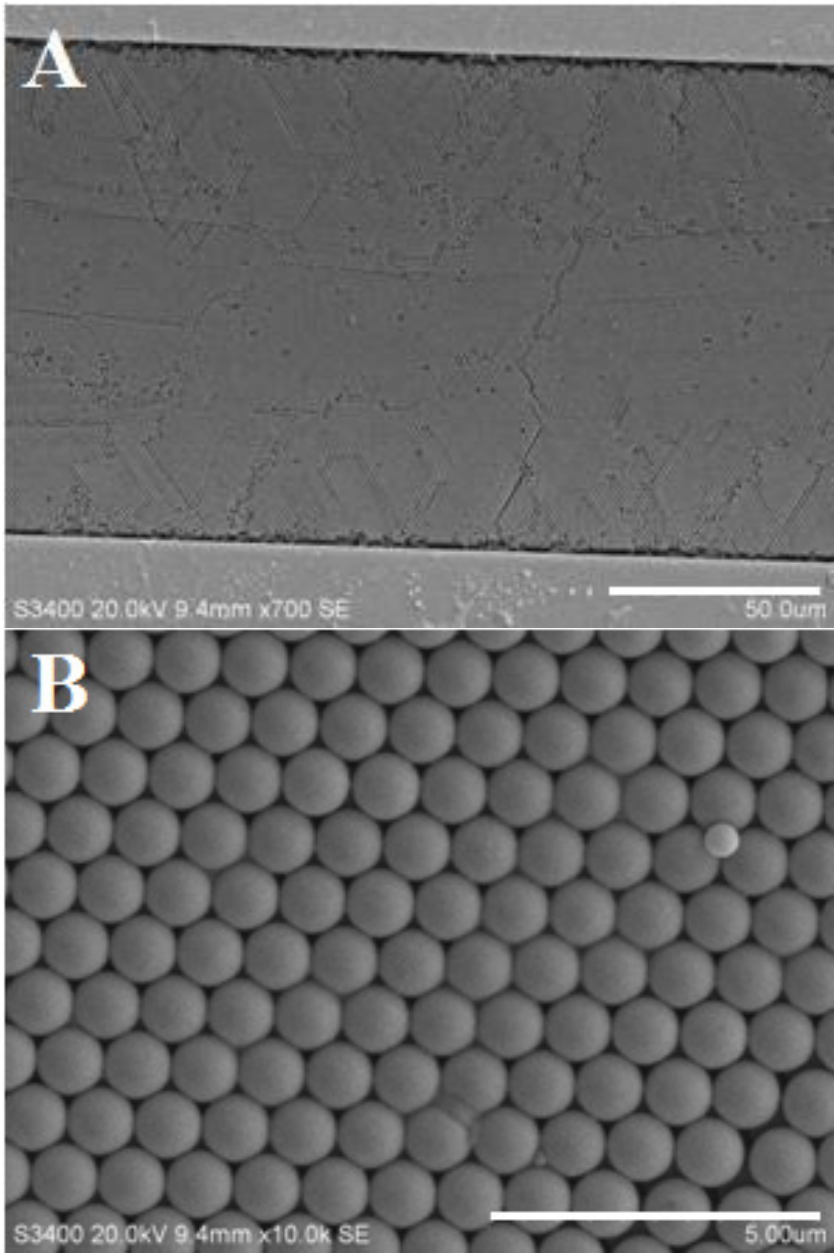

Figure 3.2: SEM images of the PS CC packed via capillary force action in a μchannel using a 1 % w/v aqueous suspension of PS beads (particle size: 1 μm). A) Mag: 700; scale: 50 μm. B) Mag: 10 k; scale: 5 μm.

Figure 3.3 shows the typical morphologies within this PANI structure after 180 s growth. Figure 3.3A shows two distinct structures of the resulting PANI which grew to a thickness greater than the depth of the PS packing (which is equivalent to the height of the μchannel (110 μm)). PANI hollow spheres were observed coincident with the top of the μchannel, which is a result of PANI growing through the template and around the outermost layer of the PS CC template. Excess bulk polymer growth was observed at heights greater than the channel depth where no PS template was present. In order to observe the structure of the PANI internally, duct tape was used to peel away the excess bulk polymer and also the outermost 'hollow sphere' layer. Figure 3.3B shows a typical image of the internal PANI structure within the channel. Defects were observed, which may be as a result of defects in the original PS template or the delamination step with the duct tape. However, the internal structure of the PANI itself appears to be primarily comprised of an ordered, honeycomb morphology.

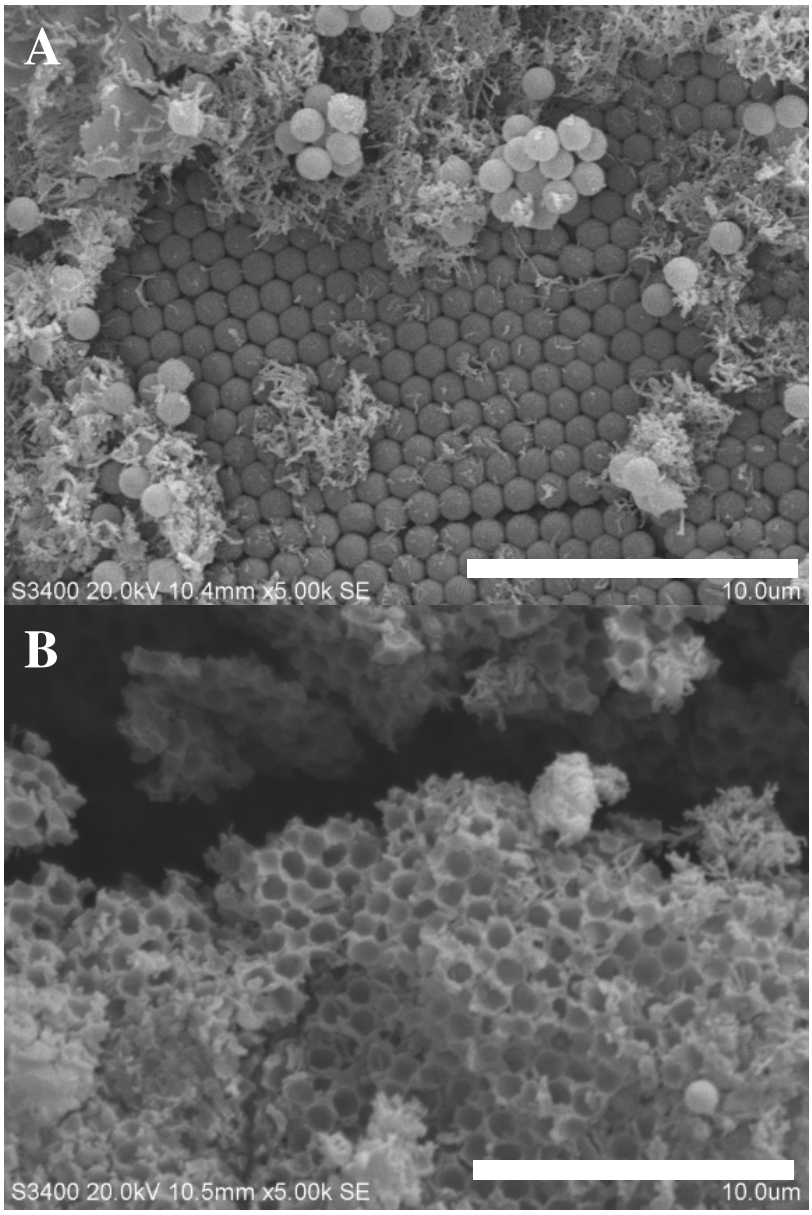

Figure 3.3: SEM images of PANI inverse opals fabricated using amperometry over 180 s in a batch cell. A potential of 0.9 V was applied vs. Ag/AgCl (electrolyte 1 M HCl). Polymerisation of aniline was structurally directed through a PS CC template. A) Imaging after dissolution of template showing hollow sphere formation and excess fibrillar growth above depth of μchannel (50 μm). B) Image of inverse opal PANI internal to the channel revealed by removing the excess PANI shown in (A). Mag: 5.00 k; scale bar: 10.0 μm.

To investigate the effect of polymerisation time, PANI was grown over a range of times on-chip and the resulting PANI inverse opals imaged. Electropolymerisation

times selected were between 90 and 360 s. By varying the growth time, the growth pattern of the templated PANI could be observed. Figure 3.4A shows the morphology of the PANI after 90 s polymerisation time. A highly heterogeneous growth of PANI is evident where growth along the gold-sputtered base and walls of the chip channel is observed. Figure 3.4B shows a more detailed morphology of the PANI for this growth time where both hollow spheres and honeycomb structures were observed. However, the pore size of the honeycomb structure was not uniform indicating a collapse in structure and/or inhomogeneous growth. This was also observed at 120 s, Figure 3.4D. Some flow-through pores were evident after 120 s of polymerisation. However due to frailties in the inverse opal structure and subsequent collapse, the flow-through nature of these pores are most likely lost. Figure 3.4C shows that a uniform growth of PANI was achieved along the base and walls of the channel for 120 s polymerisation time. Therefore after 120 s polymerisation time, uniform growth of PANI within the channel is observed. However, the structure is weak and hence after removal of the PS beads, at polymerisation times up to 120 s, the integrity of the structure was lost.

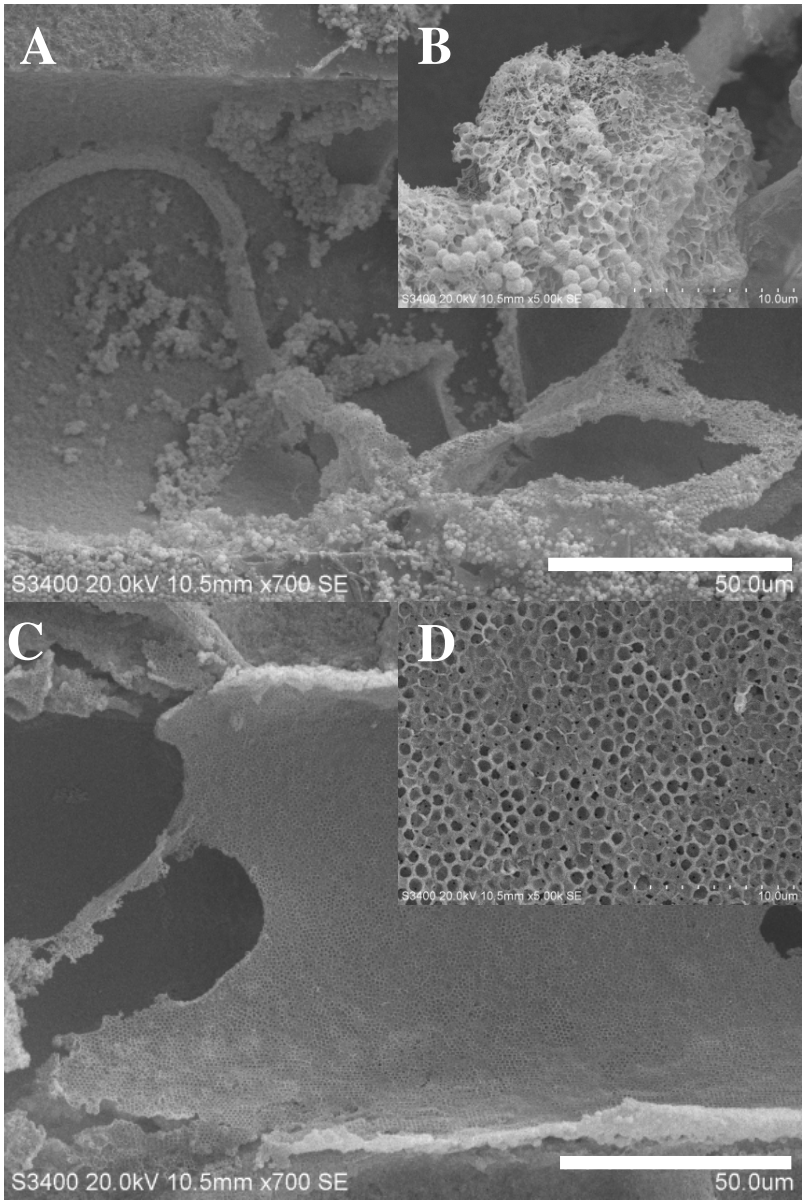

Figure 3.4: SEM images of PANI inverse opals fabricated using amperometry over 90 and 120 s in a batch cell. A potential of 0.9 V was applied vs. Ag/AgCl (electrolyte 1 M HCl). Polymerisation of aniline was structurally directed through a PS CC template. SEM images of PANI inverse opal after A & B) 90 s and C & D) 120 s polymerisation time. Mag: 700; scale bar: 50 µm; and inset Mag: 5 k; scale bar: 10 µm.

After 180 s polymerisation time, the internal PANI structure was shown to remain intact after removal of the PS template. Although hollow spheres and excess bulk PANI were observed at the top of the channel Figure 3.5A, a honeycomb structure

with some discreet flow-through pores was observed within the channel after removal of outer layers, Figure 3.5A. The process of removal of the outermost layers of PANI may have slightly deformed the structure causing the homogenity in the flow-through pores to be lost. After 240 s polymerisation time, the internal PANI inverse opal structure was again observed. Further improved definition of internal walls was observed, along with the presence of regular flow-through pores, Figure 3.5B. Some of these pores have a fragile PANI film covering them which would have been formed towards the end of the polymerisation and shows slightly too long polymerisation times.

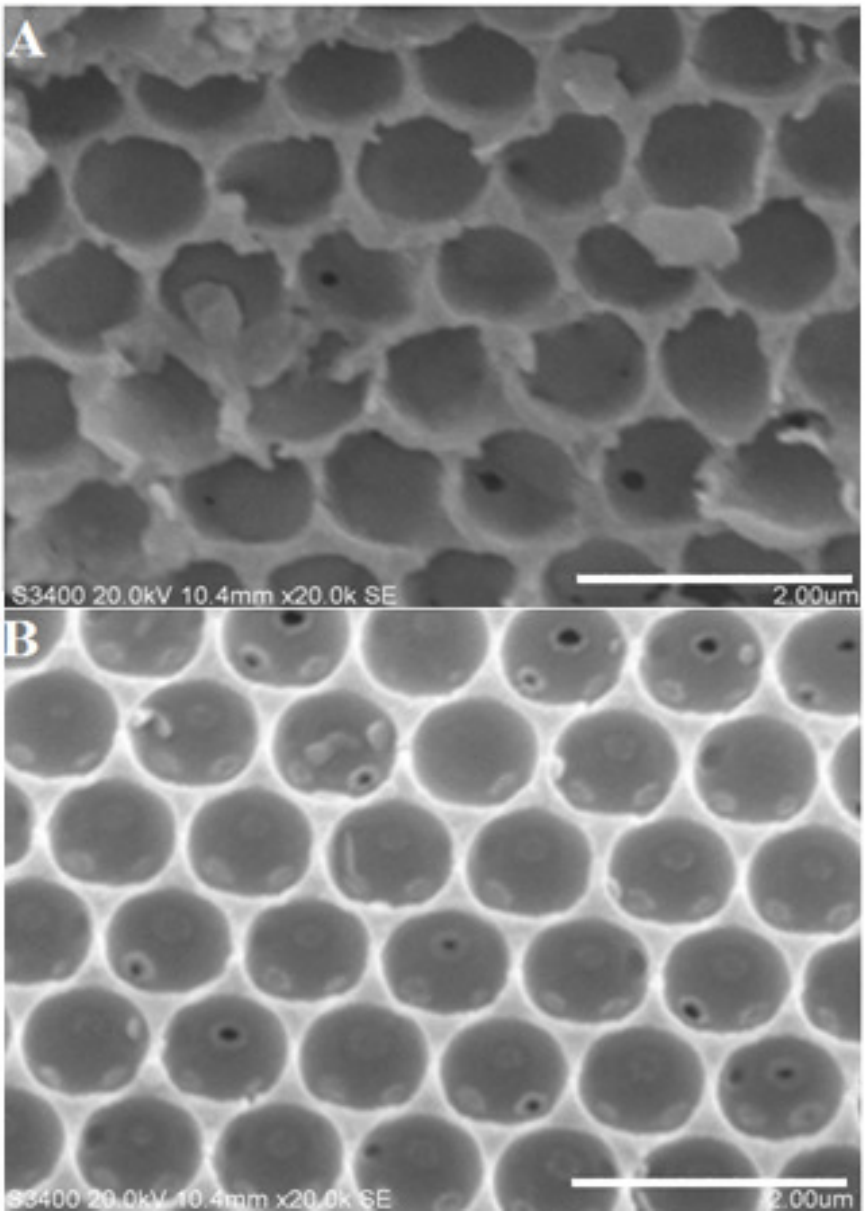

Figure 3.5: SEM images of PANI inverse opals fabricated using amperometry over 180 and 240 s in a batch cell. A potential of 0.9 V was applied vs. Ag/AgCl (electrolyte 1 M HCl). Polymerisation of aniline was structurally directed through a PS CC template. of A) PANI after 180 s polymerisation time. Image shows evidence of discreet flow-through pores in the honeycomb structure. B) SEM images of PANI after 240 s polymerisation. Mag: 20 k; scale bar: 2 µm. (Note: Hollow spheres and excess bulk PANI above the channel were removed using duct tape).

For 360 s polymerisation time, the bulk polymer growth outside the channel has a fibre-like morphology, Figure 3.6A, which is different to what was observed for lower polymerisation times. In addition, the expected inverse opal structure for the internal PANI morphology was not observed, but rather hollow spheres were apparent, Figure 3.6B. This was due to the excessive polymerisation time, which caused the flow-through pores to completely seal off, so that each pore became closed. The PANI then continued to polymerise until a thick, stable layer of PANI had grown around the spheres. Indeed the walls of the PANI was so dense in areas that the toluene did not penetrate to completely remove all the PS spheres, Figure 3.6A.

Figure 3.6A shows the morphology of the bulk PANI grown over the top of the channel. Interestingly the structure is fibrillar, in contrast to the typical branched sponge-like morphology that is typical of bulk PANI. These nano-fibres with approx. widths 100 – 200 nm, therefore must be generated as a result of the templating step. The hollow spheres of PANI formed within the channel have a very rough morphology, shown in Figure 3.6B after removal of bulk PANI. It is likely that the outer ridges on the PANI spheres that formed serve as subsequent nucleation sites for further polymerisation where the beginning of the formation of the small thin shoots of PANI can be observed (central part of image, Figure 3.6B). Further growth on these shoots resulted in the formation of the PANI nano-fibres observed in Figure 3.6A.

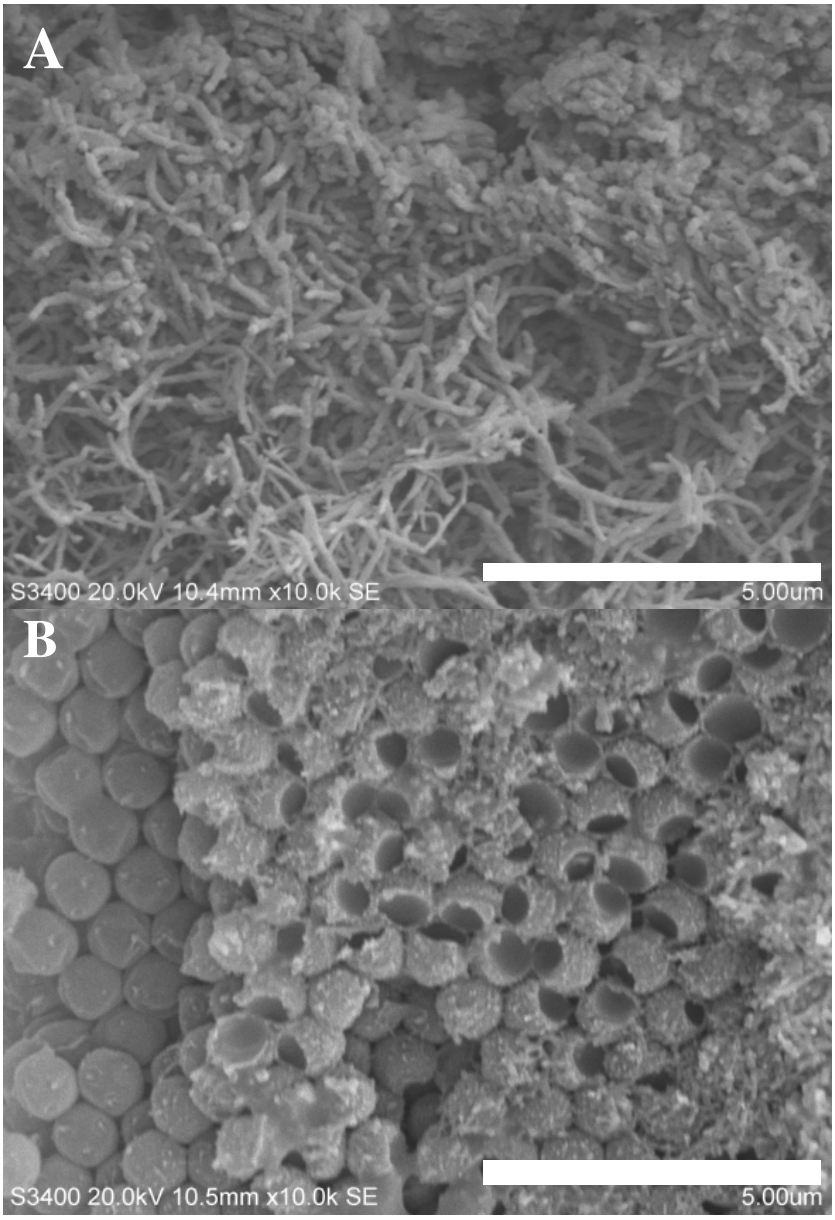

Figure 3.6: SEM images of PANI fabricated using amperometry over 360 s in a batch cell. A potential of 0.9 V was applied vs. Ag/AgCl (electrolyte 1 M HCl). Polymerisation of aniline was structurally directed through a PS CC template. A) Excess bulk PANI growth protruding from the channel. B) Hollow spheres formed internal to the μchannel, exposed after duct tape was used to remove outer excess growth. Mag: 10 k, scale bar: 5 μm.

A CV of PANI films polymerised amperometrically for 90, 210 and 360 s polymerisation are shown below in Figure 3.7 as expected the current gradually increases from 90 s – 210 s moving from a fragile structure to an invere opal. Increased peak height at 0.6 V after 90 s polymerisation is likely due to contribution from the underlying gold WE which may not have been fully isoltaed due to the short polymerisation time. The peak at ~0.6 V decreases gradually in intensity for both 210 and 360 s polymerisation time due to increased PANI coverage with extended polymerisation.

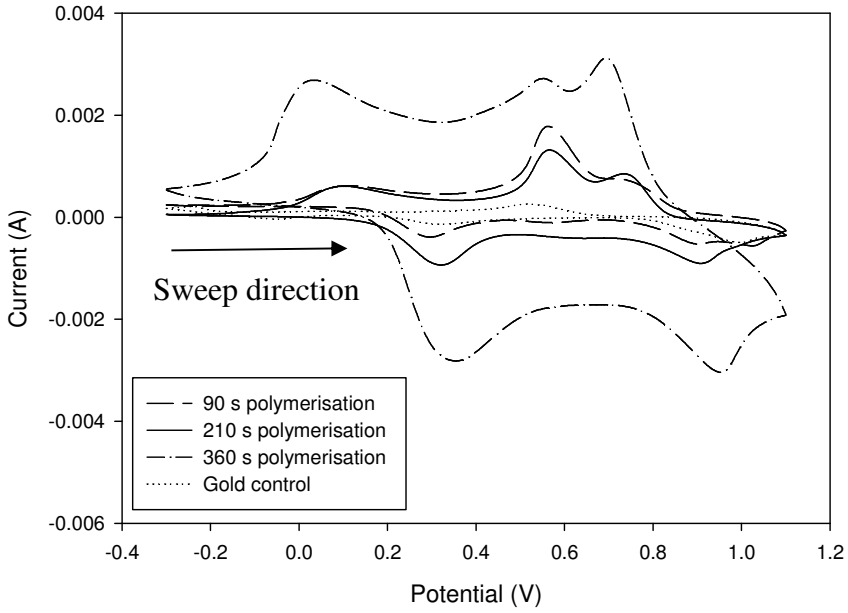

Figure 3.7: CV of templated PANI films after 90, 210 and 360 s amperometric polymerisation at a fixed potential of 0.9 V with a gold WE, Ag/AgCl reference and Pt mesh counter electrode. PANI films were CV's were performed in 10mL 1 M HCl at a scan rate of 0.1 Vs^{-1} vs. Ag/AgCl reference electrode over 6 segments with the 5th and 6th segments plotted as a comparison.

As a result of varying electrochemical polymerisation time an optimum growth time was determined to be 210 s which would allow for an inverse opal structure with

discrete flow-through pores between interlinking layers of the 3D ICP structure. In conjunction with this it would ensure more homogeous ICP growth throughout the length and depth of the μfluidic channel.

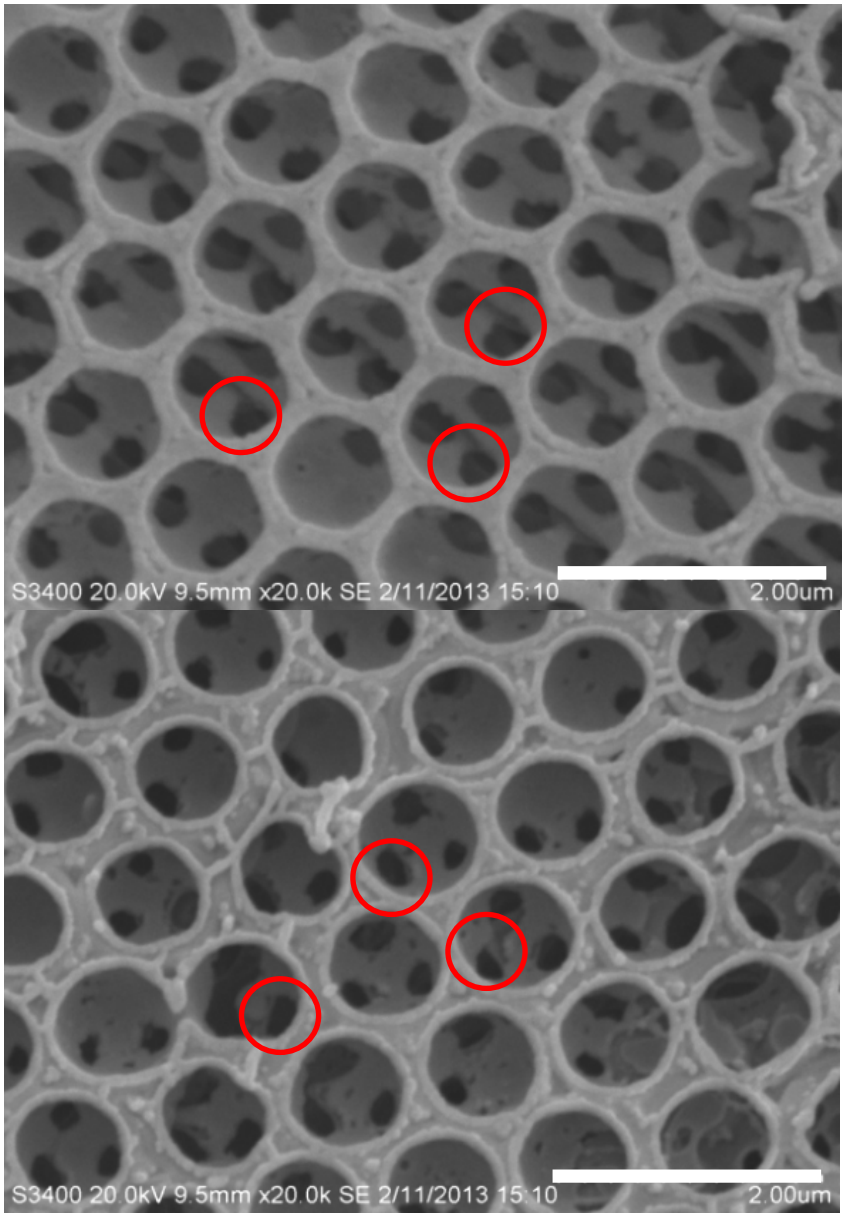

Figure 3.8: SEM images of PANI inverse opals fabricated using amperometry over an optimum growth time of 210 s in a batch cell. A potential of 0.9 V was applied vs. Ag/AgCl (electrolyte 1 M HCl). Polymerisation of aniline was structurally directed

through a PS CC template. SEM images of A) top area and B) middle area of PANI. Note flow-through pores have been circled in red. Mag: 20 k; scale bar: 2 µm

Figure 3.8A & B illustrate the optimised ICP inverse opal structure after 210 s electrochemical polymerisation. Well defined flow-through macro-pores were noted as expected, circled in red, connecting upper and lower layers of the 3D ordered ICP inverse opal structure. CV was performed on the micro-structured, templated PANI grown after 210 s in the µchannel, Figure 3.9. Typical electrochemistry of PANI was observed [174]. This was compared to that of bulk, non-templated PANI grown for the same amount of time. Both CVs were comparable showing electrochemical control over PANI in channel. However, due to bulk over-growth during polymerisation, as shown earlier in fibrillar bulk PANI and hollow sphere formation, PANI electrochemistry is likely to have been overshadowed by "bulk" electrochemistry in the upper areas of the channel and surface of the µfluidic chip.

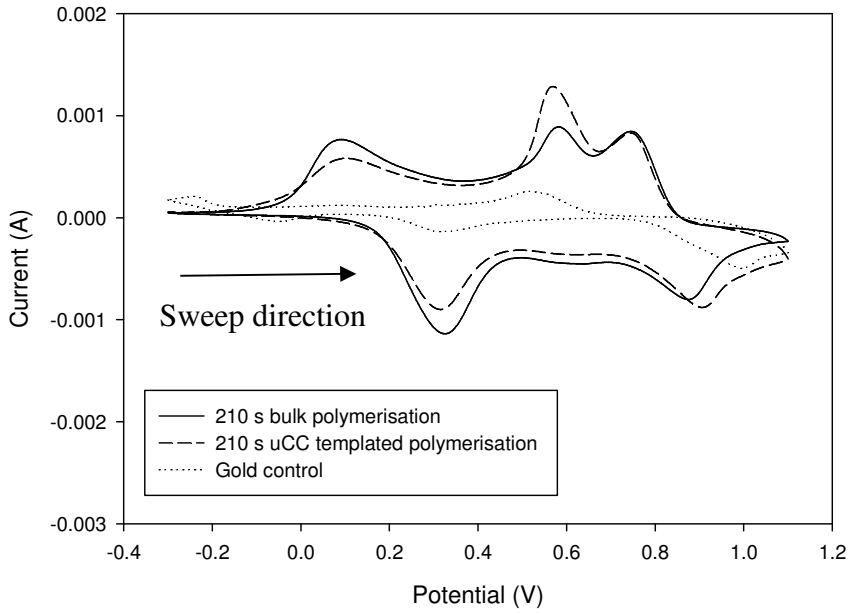

Figure 3.9: CV of bare gold WE control, bulk PANI and uCC templated PANI films fabricated within the confines of a μchannel. Amperometric polymerisation was used over 210 s at 0.9 V vs. Ag/AgCl (electrolyte 1 M HCl). CV's were performed in 10mL 1 M HCl at a scan rate of 0.1 Vs^{-1} vs. Ag/AgCl reference electrode over 6 segments with the 5^{th} and 6^{th} segments plotted as a comparison.

3.4 Conclusion

This chapter demonstrates that templating of conducting polymers such as PANI can be achieved easily within μfluidic channels and that the electropolymerisation time is critical not only to the depth of the PANI, but also to the intrinsic morphology and flow-through nature of the material. Future application for these findings include the development of new LOC applications utilising highly-controlled conducting polymer materials for sensing.

Specifically, CC comprised of PS were achieved in glass μfluidic channels from surfactant-free suspensions of PS using capillary force packing. PANI was then electrochemically polymerised through the PS uCC template for a range of times, and the template was subsequently removed, resulting in inverse opal micro-structures of PANI housed in a μchannel. Two main morphologies of PANI were evident within the channels: hollow spheres were observed at the top of the channel and a honeycomb structure was observed internally. Variation in electropolymerisation times resulted in different inverse opal morphologies of the PANI. At short polymerisation times (< 120 s), thin PANI coatings were observed on the walls and base of the channel. Within the films, both honeycomb and hollow sphere formation was observed but the structures were fragile and appeared collapsed in places. At excessively long polymerisation times the inverse opal structure of the template was completely lost and hollow sphere formation was observed within the channel. At an optimised polymerisation time of 210 s, the PANI inverse opal structure was shown to be defined with flow-through pores evident, demonstrating its potential for flow-through LOC applications such as high surface area catalysis and sensing and as a conducting separation phase or extraction material.

Chapter 4

Chemical Polymerisation of Homogenous 3D Ordered Conducting Polymer-Polystyrene Opal Structures in μfluidic Channels

4.1 Introduction

Chemical polymerisation is a simple process which offers a method to fabricate bulk quantities of intrinsically conducting polymer (ICP) materials. Oxidation of monomer units during chemical polymerisation methods is achieved using a chemical oxidant with high oxidation potentials (exceeding +1.0 V) such as ammonium persulfate (APS) [189]. Acidic pH is used during polymerisation for monomer solubility and formation of the most conducting salt forms (*e.g.* Emeraldine Salt in the case of polyaniline (PANI)). The mechanism for chemical polymerisation of aniline is initially similar to that presented in Scheme 3.2 for electrochemical polymerisation. Where chemical polymerisation of aniline differs from electrochemical polymerisation is during chain propagation. Due to the high oxidising power of chemical oxidants such as APS formation of the fully oxidised Pernigraniline Salt form, in the case of PANI results [166]. The conducting Emeraldine Salt is subsequently formed when the oxidant has been fully consumed and the remaining aniline in solution reduces fully oxidised Pernigraniline Salt to the partially oxidised Emeraldine Salt. Many aspects of chemical polymerisation can be manipulated to vary the resulting morphology, conductivity and molecular weight. For example, chemical polymerisation at lower temperatures (*e.g.* below 5^{o}C) have been shown to decrease defects in the resulting PANI films (such as ortho-coupling) and fabricate higher molecular weight PANI [190]. A limitation of chemical polymerisation is that the ICP film is not initially electrochemically addressable as polymerisation occurs in solution rather than at an electrode surface. As a result deposition onto a working electrode (WE) is required after polymerisation to achieved electrochemical addressability.

Chemically polymerisation of ICP films/composites has seen widespread application in areas such as energy storage [191-193], separations [70, 194, 195], and sensing [196, 197]. Similar to electrochemical polymerisation, templating during chemical polymerisation has shown a route to highly ordered ICP structures. Templating methods include hard templates such as polystyrene (PS) sphere colloidal crystals (CC) [198] and soft templates [199] such as surfactants [200]. The presence of a soft template such as a surfactant during chemical polymerisation can result in controlled ICP morphologies. For example Olad *et al.* [201] demonstrated the fabrication of PANI nano-fibres through chemical polymerisation in the presence of Triton X-100 a non-ionic surfactant. The homogeneity and consistency of PANI nano-fibres fabricated was improved upon addition of the surfactant. Similarly Zhou *et al.* [202] demonstrated the fabrication of PANI nano-fibres through the addition of cetyltrimethyl ammonium bromide (CTAB) and sodium dodecylbenzyl sulfonate (SDBS) in a mixed surfactant method. Here the conductivity was increased (0.102 S/cm) in comparison to single component surfactant methods (5.3×10^{-3} S/cm) and more uniformly branched PANI nano-fibres were achieved.

Examples of chemically polymerised ICP films structurally directed using hard templates include Yang *et al.* [203], who demonstrated a simple chemical polymerisation method to fabrication PANI inverse opals on glass micro slides. Patterned gold electrodes were used in the presence of dodecylbenzenesulfonic acid (DBSA). Templating of PANI inverse opals was achieved using a PS sphere CC. Fabrication of PS CC through dip drawing produced ordered PS templates with variation in thickness achieved by increasing % w/v of PS suspensions. Thickness of resulting PANI inverse opals was between 2.4 - 9.7 μm (5 – 20 layers of 485 nm PS spheres) [203]. Yang has detailed the application of such PANI films in chemical

[204] and gas sensing [205]. Chemical polymerisation was also used to form PANI-infiltrated TiO_2 inverse opal photonic crystals [198]. In this instance, aniline was chemically polymerised through TiO_2 inverse opals fabricated through PS templating. These structures were shown to be optically sensitive to pH.

In the case of hard templates, it is generally assumed in the literature that if the 3D CC template structure is uniform throughout, the resulting template directed ICP film will also possess this structural homogeneity. Indeed, the advantages attributed to 3D ordered macroporous (3-DOM) materials are often dependent upon such inverse opal homogeneity [206, 207]. However, template directed polymerisation methods, such as electrochemical polymerisation, do not necessarily result in this assumed homogeneity. Here, the potential for structural inhomogeneity as a result of electrochemical polymerisation through a hard template is demonstrated. An alternate polymerisation strategy to overcome this inhomogeneity has been developed where chemical polymerisation was employed in the fabrication of a 3D ordered PANI/PS opal. This method demonstrates a flow-through 3D ordered PANI/PS opal structure housed within a sealed μfluidic channel and offers an electrochemically addressable flow-through material. The flow-through nature and homogeneity of the ICP material fabricated in this work demonstrates an improvement on other μfluidic housings incorporating ICP films in channel which demonstrate flow over [57, 94] rather than through the ICP material in channel. Materials of this type will have application in future Lab-On-Chip applications such as sensing [196, 208] and separation [209].

4.2 Experimental

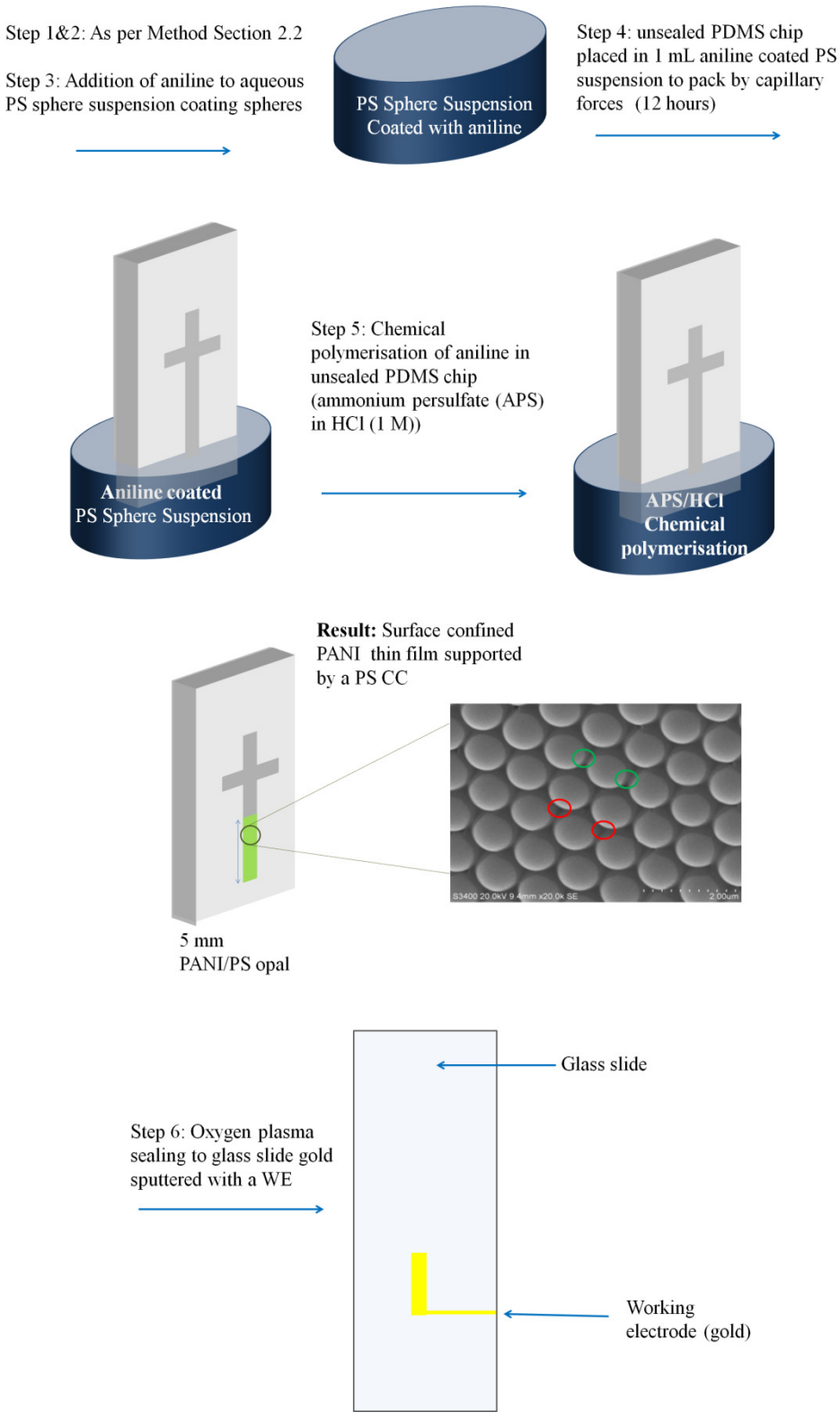

Scheme 4.1: Schematic representation of the method employed to fabrication a surface confined chemically polymerised PANI structured opal within a μchannel.

4.2.1 Materials

As per method Section 3.2.1.

4.2.2 Instrumentation

As per Method Section 3.2.2 with the following addition, a CHI600c electrochemical analyser (CH Instruments Inc., USA) was used for all electrochemical experiments. A CMA microinjection system (Microdialysis, Sweden) was used for all flow-through experiments. All oxygen plasma treatment was performed using a Harrick plasma cleaner PDC-001 expanded model.

4.2.3 Methods

4.2.3.1 PDMS chip fabrication incorporating an electrochemical cell

As per Method Section 2.2.3.2 with the following addition, a well was punctured in the chip at the outlet to enlarge it to 3 cm in diameter. The combined reference and auxiliary electrodes were housed in the well during electrochemical experiments as detailed previously by Power *et al.* [57]. Sealing of chips to WE for the electrochemical cell was achieved through oxygen plasma treatment of the surface of the PDMS chip and a glass slide for 5 min before sealing together and applying pressure for 20-30 s. PDMS chips were masked to isolate the μfluidic channel using duct tape, and then gold sputtered for 2.5 min at 45 mA to form the WE with dimensions of 0.110 mm x 40 mm. Alternatively, WE's were sputtered to a glass slide using an appropriate mask corresponding to channel width. Gold sputtered glass slides were then sealed to PDMS chips. Figure 4.1 illustrates a sealed μfluidic chip with gold sputtered WE aligned to the μchannel and the combined reference and counter electrode housed within the outlet.

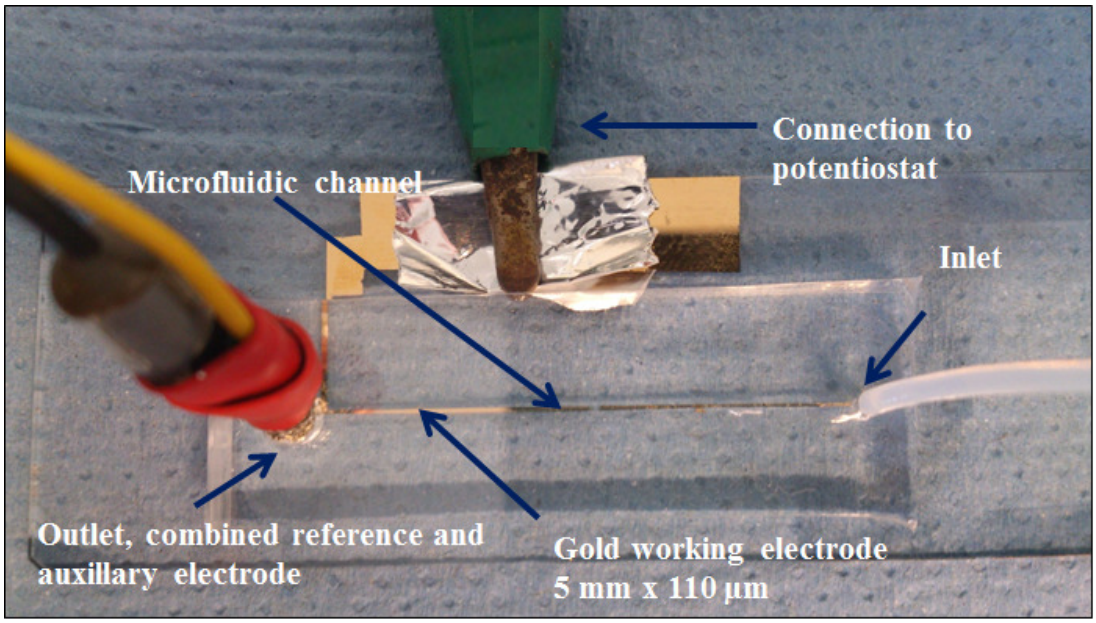

Figure 4.1: Picture showing the microfluidic housing developed by Power et al.[57] with a gold sputtered WE 5mm x 110 µm, combined reference (Ag/AgCl) and counter electrode (Pt mesh) housed within the outlet of the microfluidic housing.

4.2.3.2 PS colloidal crystal formation

As per Method Section 2.2.3.3 and 2.2.3.4

4.2.3.3 Electrochemical polymerisation of aniline through CC template

As per Method Section 3.2.3.3

4.2.3.4 Preparation of aniline-coated PS spheres

81.6 µL of aniline (2.2 mM) was added to 0.4 g of 1 µm PS sphere in 40 mL of D.I. water under constant stirring for 30 min. The aniline-coated PS spheres were then centrifuged down at 5000 rpm for 7 min to remove excess aniline in solution. The spheres were then re-dispersed in 40 mL D.I. water resulting in a 1 % w/v aniline-coated PS sphere suspension.

4.2.3.5 Chemical polymerisation of aniline-coated PS CC

A PDMS μchip containing an aniline-coated CC was immersed in a solution of APS (7.8 mM) in 10 mL of HCl (1 M) at room temperature and left standing for 8 h. After polymerisation, the PANI was washed in D.I. water for 20 s and subsequently allowed to air dry for 20 min. After chemical polymerisation, a 10-segment voltammetry cycling between -0.3 and +1.1V vs. Ag/AgCl and scan rate of 0.1 V/s was performed to induce a consistent electrical connection between the PANI-coated CC and the underlying WE.

4.3 Results and Discussion

4.3.1 PS CC template formation

Capillary force packing was used to form ordered multi-layer unimodal CC (uCC), Figure 4.2A, and bCC, Figure 4.2B, structures within the confines of a μfluidic channel. During CC fabrication as described in the methodology, the volume fraction (VF) was constant at 1 % w/v for uCC with a $VF_{S/L}$ = 0.1 for bCC structures. All CC were fabricated over 12 h according to the dimensions of the channel (0.11 mm x 0.11 mm x 40 mm) and were used as templates for PANI growth.

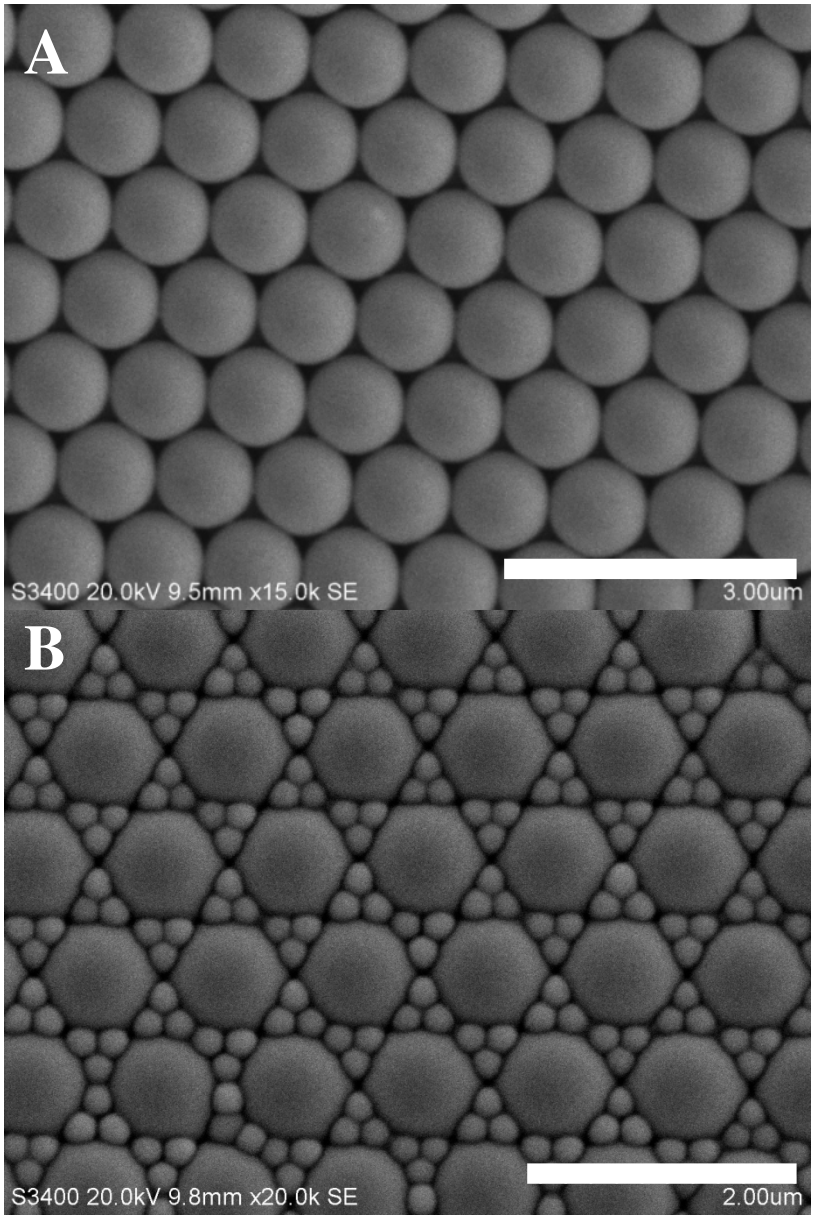

Figure 4.2: Images of µchannel housed a) uCC PS template comprising macro (D_L = 1 µm 1 % w/v) and b) bCC PS template comprising macro (D_L = 1 µm) and nano (D_S = 200 nm) spheres ($VF_{S/L}$ = 0.1). Mag: 20.0 k; scale bar: 2.00 µm.

4.3.2 Electrochemical polymerisation of aniline through bCC template

Electrochemical polymerisation was carried out in unsealed µchannels through CC templates. Aniline was electrochemically polymerised through the template for 100 s resulting in a reproducible ordered PANI structure, by SEM analysis of the internal structure within the µchannel. However, when internal sections of the resulting PANI structure were imaged by SEM, subsequent to the removal of the PS bCC scaffold, it

could be seen that the morphology of the structure continuously decreased in wall thickness towards the top of the μchannel. In images of upper internal layers of the structure, which was furthest from the integrated gold WE, the PANI structure showed some areas comprising the desired macro and meso-pores resulting from the interconnectivity of the macro-spheres and placement of nano-spheres in the interstitial voids. However, the structure appeared fragile and contained defects, likely due to a collapsed structure, Figure 4.3(b)A. Moving down the depth of the channel towards mid-way, the density of the PANI continued to increase. Flow-through pores arising from the interconnecting macro-sized PS spheres were formed. However, loss of mesopores from the nano-spheres was noted, Figure 4.3(b)B. Finally, along the lower areas of the channel, closest to the gold WE, PANI had the densest morphology with the desired mesopores, and flow-through macro-pores, completely sealed due to excessive PANI growth, Figure 4.3(b)C. This electrochemical fabrication technique was observed to result in PANI morphology with a density gradient through the μchannel depth. This was likely the result of a charge density gradient descending from the integrated WE to the top of the PANI structure [210, 211], and illustrated that the morphology of the PANI structure was non-homogenous throughout the inverse opal.

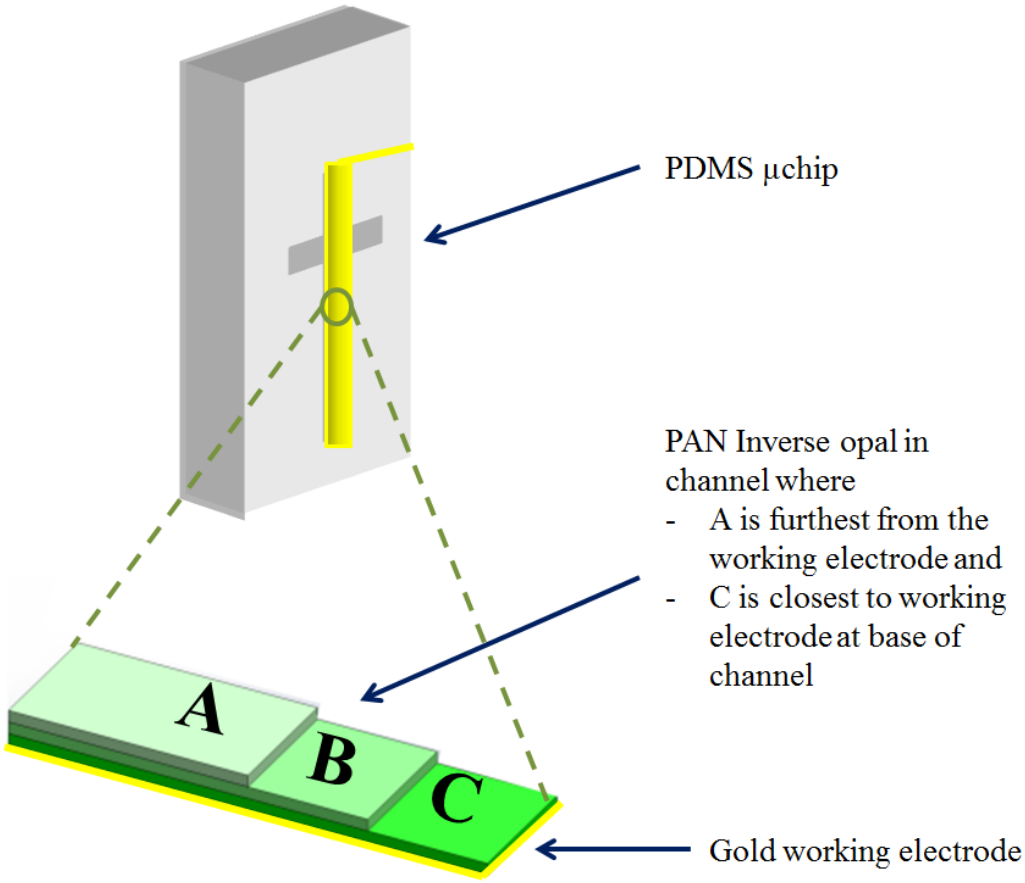

Figure 4.3(a): Schematic of PDMS chip containing a µchannel housing an electrochemically grown PANI inverse opal where areas of the inverse structure are defined as A) upper layer furthest from WE, B) ~ middle area of µchannel and C) lower area closest to WE at base of µchannel.

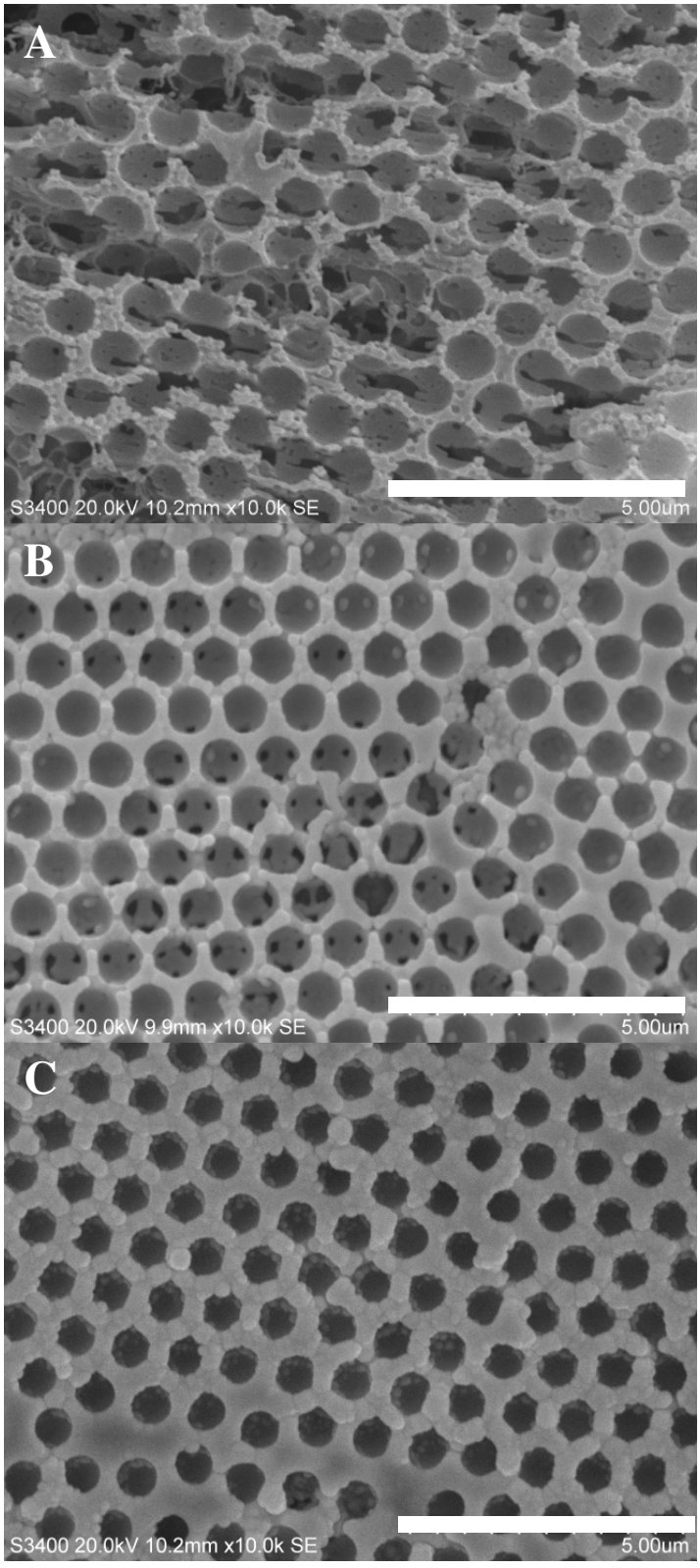

Figure 4.3(b): SEM images of PANI inverse opal housed within a PDMS μchip. PANI was electrochemically polymerised in a batch cell and structurally directed by a PS uCC template during application of a constant potential of 0.9 V vs. Ag/AgCl reference electrode with a Pt mesh counter (electrolyte 1 M HCl). After removal of

PS template the PANI inverse opal homogeneity was investigated A) corresponds to the upper layer of the PANI inverse opal furthest from the WE. B) Middle layer of PANI inverse opal. D) Lower layer of PANI inverse opal, closest to WE. Mag: 10.0 k; scale bar; 5.00 µm.

4.3.3 Bulk chemical polymerisation of aniline through bCC template

After concluding that homogeneity during electrochemical polymerisation was poor a move to bulk chemical polymerisation was investigated to try to increase homogeneity through the depth of the µchannel. Increased homogeneity was achieved in the µchannel. However, bulk untemplated PANI areas, Figure 4.4A, and PANI core shells, Figure 4.4B, were achieved on the PDMS chip surface in the case of bulk PANI and at the top of the CC closest to the aniline/oxidant solution in the case of PANI core shells.

As a result of excessive polymerisation the PDMS µchip surface was covered in bulk PANI thereby masking the template-directed monolith in channel, Figure 4.4A. Template-directed structure with increased uniformity was evident upon removal of upper layers using duct tape, Figure 4.4C. However, due to excessive bulk polymerisation the templated sections of PANI monolith were not addressable electrochemically as the µchip could not be sealed subsequent to bulk chemical polymerisation.

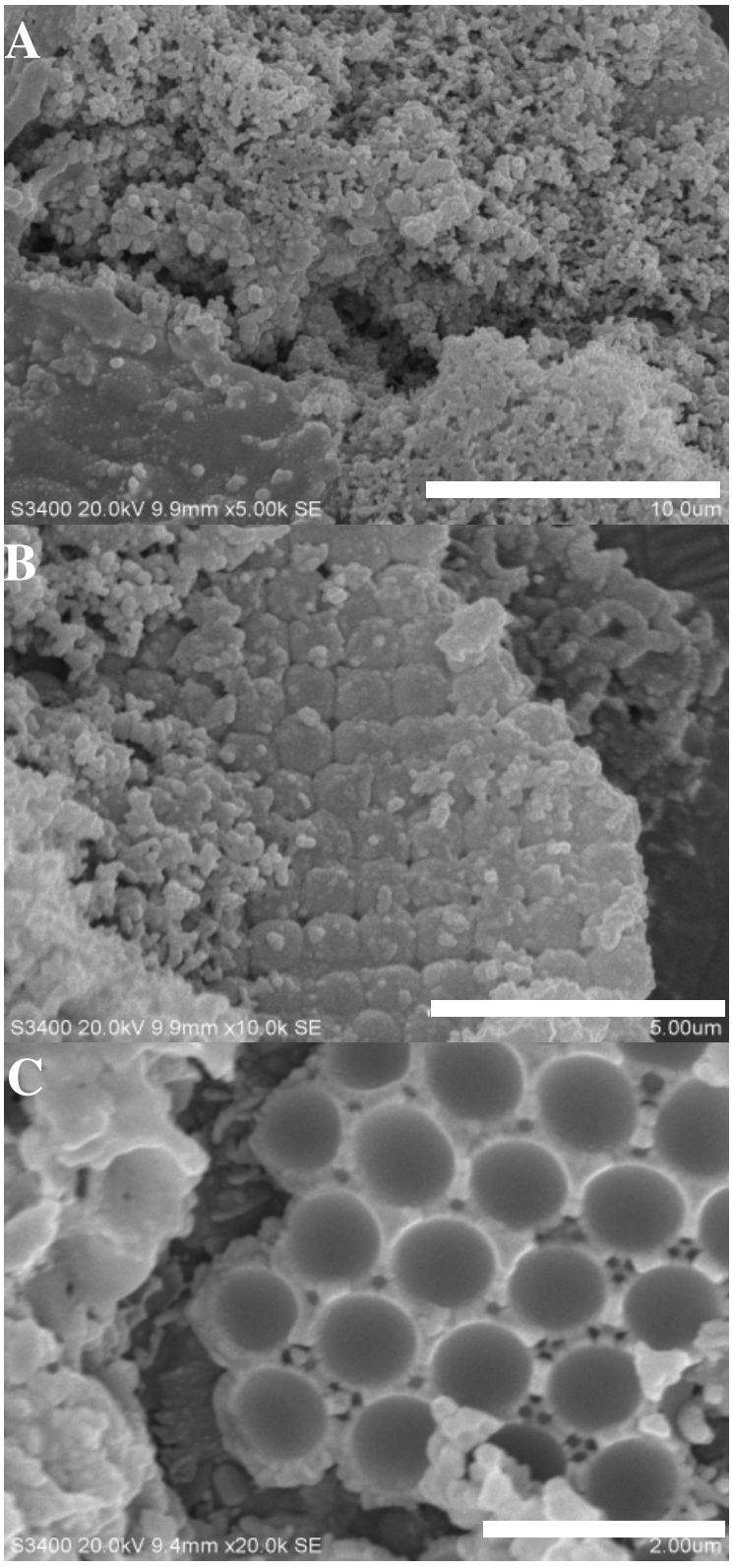

Figure 4.4: SEM images of PANI inverse opal structure fabricated in batch cell through mixing of aniline monomer and oxidant in the presence of acid (1 M HCl) for 8 h. PS bCC structure subsequently removed after polymerisation using toluene. SEM images illustrate A) PANI at the top of the μchannel where excessive bulk

polymerisation was noted. Mag: 5.00 k; scale bar: 10.0 µm. B) Core shell and bulk PANI, top of channel. Mag: 10.0 k; scale bar: 5.00 µm. C) Ordered inverse opal structure present below bulk growth imaged after removal of excess bulk PANI. Mag: 20.0 k; scale bar: 2.00 µm

4.3.4 Chemical polymerisation of aniline-coated uCC template

To enable multiple polymerisation initiation sites homogenously dispersed throughout the PS template, which would overcome the density gradient previously observed in electrochemical and the excessive polymerisation noted during bulk chemical polymerisation, aniline-coated PS spheres were prepared. As detailed in the Methods Section 4.2.3.6, 1 µm PS spheres were exposed to aniline (2.2 mM) in an aqueous medium. Hydrophobic-hydrophobic interactions between PS spheres and benzene ring of the aniline monomer facilitated the adsorption of aniline to the PS spheres. A schematic showing the adsorption of aniline to the PS sphere and its subsequent polymerisation is detailed in Scheme 4.2. After modification, the aniline-coated PS spheres were successfully packed uniformly in channel by capillary force packing according to Methods Section 2.3.2. The aniline coating was then chemically polymerised in chip in both unsealed and sealed channel formats.

After the chemical polymerisation of the aniline a thin coating was observed through the uCC. Due to the fragility of the PANI coatings, the CC template was kept in place to act as a supporting scaffold resulting in a PANI-PS structured opal. In this composite structure (PANI-coated PS spheres) flow through was achieved through the interstitial voids present between the macro-sized PS spheres.

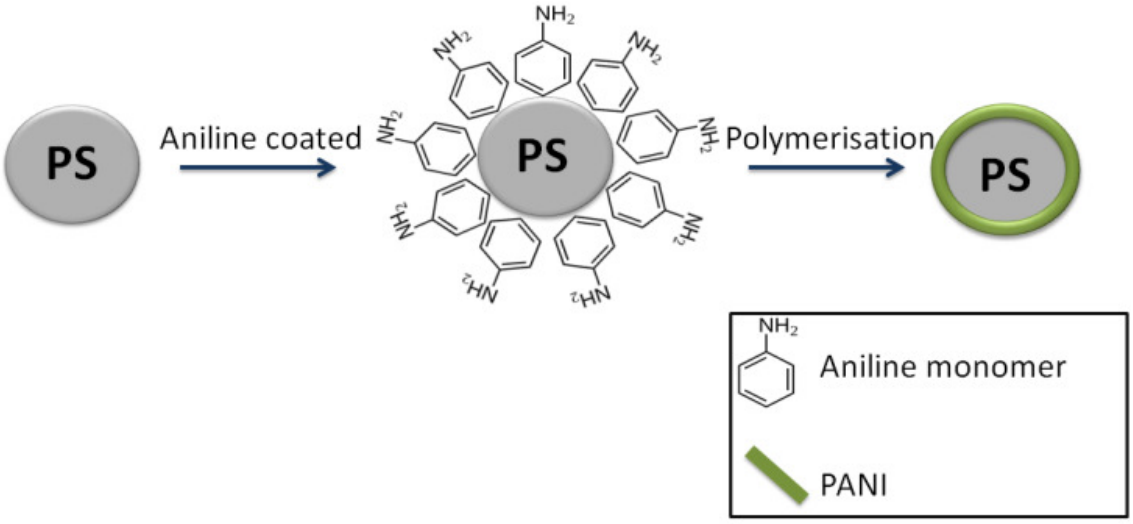

Scheme 4.2: Schematic of PS sphere coating with aniline and subsequent surface confined polymerisation of PANI on individual PS spheres.

Using chemical polymerisation, homogeneous PANI coverage throughout the full depth of the µchannel was achieved, illustrated in Figure 4.5. SEM images were taken of internal upper, middle and lower layers of the µchannel corresponding to the areas previously noted during electrochemical polymerisation, Figure 4.3. In the case of PANI-PS CC polymerised chemically under flow conditions the same morphology was shown in each area with a thin layer of PANI present within the µchannel (circled in green) and interstitial voids (circled in red) of the uCC structure, Figure 4.5A. The flow profile of oxidant/HCl solution through the face centred cubic (fcc) uCC structures dictates that polymerisation can only occur in the voids present between PS spheres. Where PS spheres touch no polymerisation can occur as flow cannot reach these areas. Figure 4.5D-F show the inverse structures achieved after contrast conversion using Hitachi S-3400N SEM software, illustrating further the voids where polymerisation occurs during chemical polymerisation in a sealed µchannel under flow conditions. Thus the inhomogeneity during electrochemical polymerisation was shown to have been successfully overcome with homogeneous

coverage over all layers within the 180 µm deep µchannel. To investigate the homogeneity of the coverage further an area of 245 μm^2 was examined to determine the % of channel and interstitial voids successfully coated with a thin PANI coating after flow-through chemical polymerisation. It was found that 92 % of channel voids and 97 % of interstitial voids were successfully filled using this method.

4.3.5 Investigation of electrochemical behaviour of PANI-PS composites

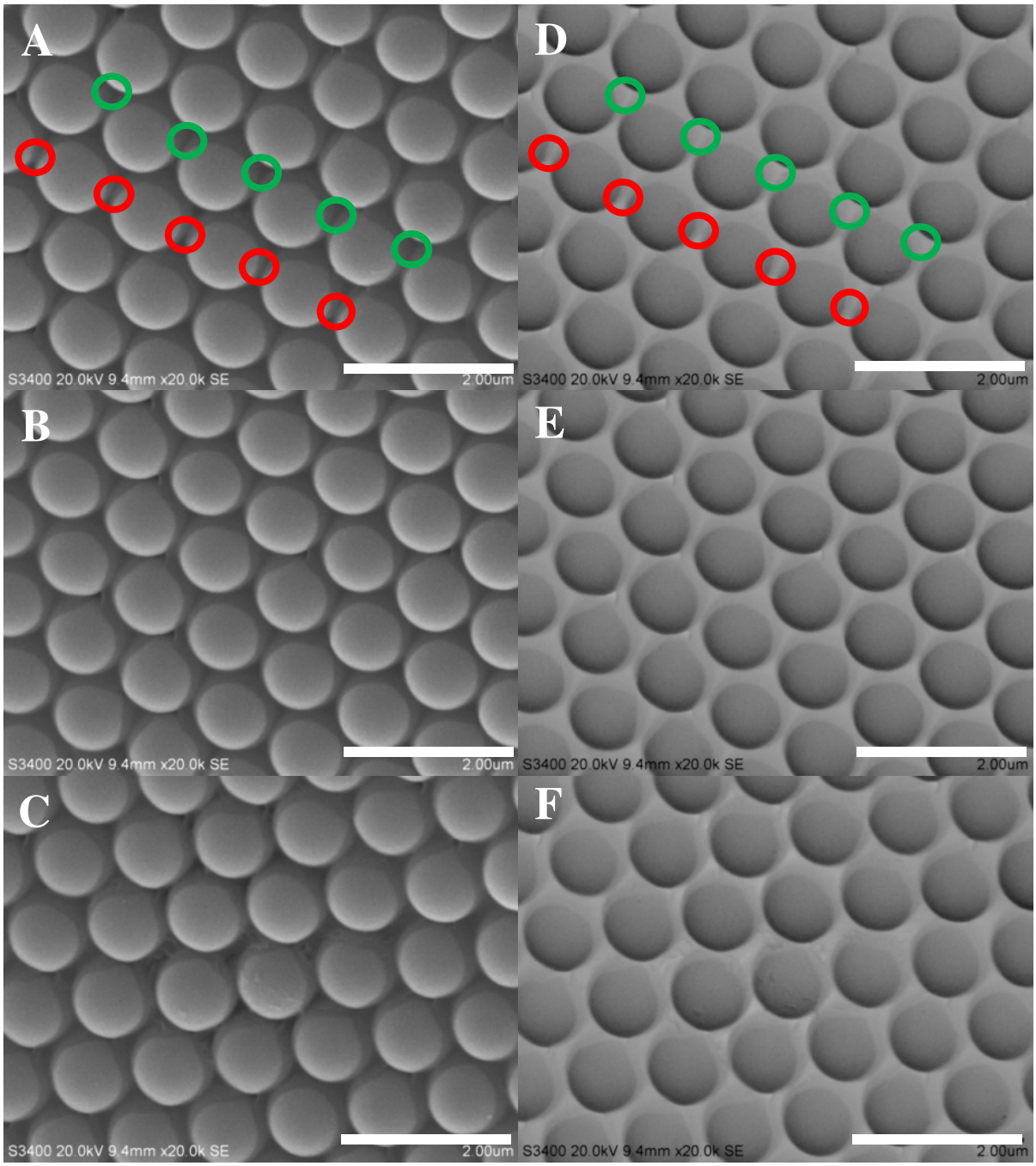

Figure 4.5: PANI/PS opal structures – polymerised by flow through of oxidant (APS) in the presence of an acid (1 M HCl) in a sealed μchannel for 8h. SEM images illustrating representative internal layers as follows: A) upper layer B) middle layer and C) lower layer of PANI-PS CC. Thin layers of PANI present within the channel void, circled in red and interstitial voids, circled in green, are highlighted. Images D-F show the inverse structures of images A-C after contrast conversion using Hitachi S3400N SEM software. Mag: 10.0 k; scale bar: 5.00 μm.

After chemical polymerisation of the aniline-coated PS uCC only, the electrochemical behaviour of the system was investigated. It was found that the electrochemistry of the PANI-coated CC could only be accessed by electrochemically polymerising a thin PANI film to the integrated gold WE in order to give an electrical bridge between the soft thin PANI coating on the CC and the gold WE. The electrochemistry exhibited when the PANI-coated uCC was present before cycling in aniline was dominated by typical bulk gold redox electrochemistry with the gold surface changed due to gold chloride formation, illustrated by the large peak at 0.4 V, Figure 4.6B. To illustrate that the gold electrochemistry was typical of bulk gold in HCl, voltammetric cycling of a bare gold electrode, diameter 1 mm, in a batch cell was performed to demonstrate the electrochemistry of bulk gold in HCl, Figure 4.6A; here the characteristic large peak at 0.4 V is evident. The electrochemistry observed for the PANI-PS opal structure in a sealed μchannel, WE dimension of 0.220 x 5 mm, before electrochemical connection to the WE, was dominated by this typical bulk gold redox electrochemistry. A slight shift below 0.4 V was noted as a result of increased resistivity in the system due to the PS CC backbone of the opal structure. Figure 4.6C shows the electrochemistry of a bare gold electrode in a sealed μchannel with WE dimension of 0.220 x 5 mm. In all cases

electrochemically cycling was performed vs. Ag/AgCl in HCl (1 M) under stop-flow conditions at a scan rate of 0.1 V/s.

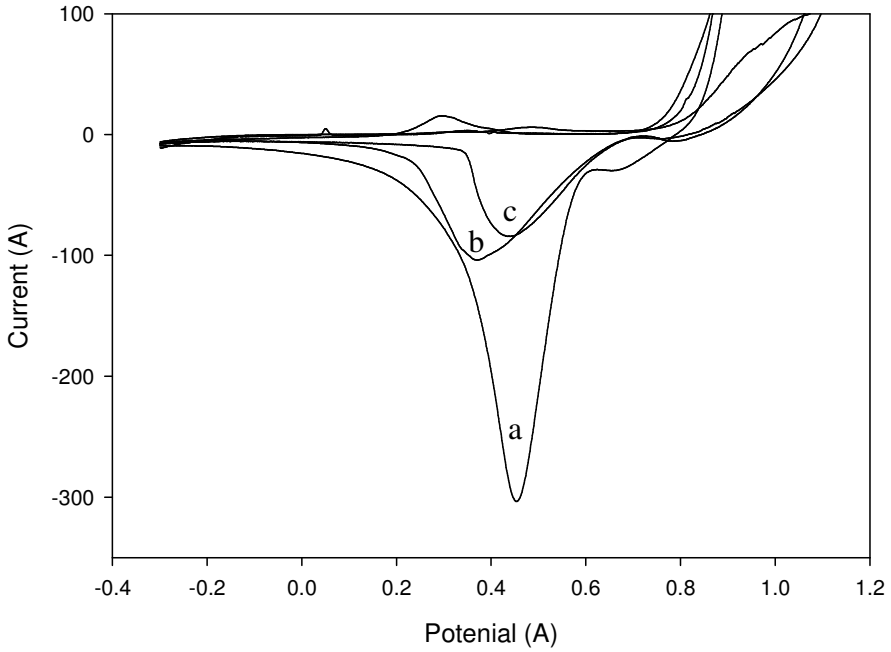

Figure 4.6: Comparison of gold electrochemistry A) in three electrode cell with WE diameter 1 mm. B) Illustrates the electrochemistry in a sealed μchannel with PANI-PS opal structure in place before electrochemical bridging under stop-flow conditions, WE dimensions 0.220 x 5 mm. C) Illustrates the electrochemistry of a gold WE in a sealed μchannel with WE dimensions 0.220 x 5 mm under stop-flow conditions vs. Ag/AgCl. In all cases CV was performed vs. Ag/AgCl reference electrode and Pt mesh counter electrode in HCl (1 M) with the third cycle of each taken and plotted.

After confirmation of the gold electrochemistry in the μchannel 10 voltammetric cycles were performed in aniline in a sealed μchannel containing the PANI-PS CC opal structure to electrochemically bridge the PANI structure to the WE, Figure 4.7.

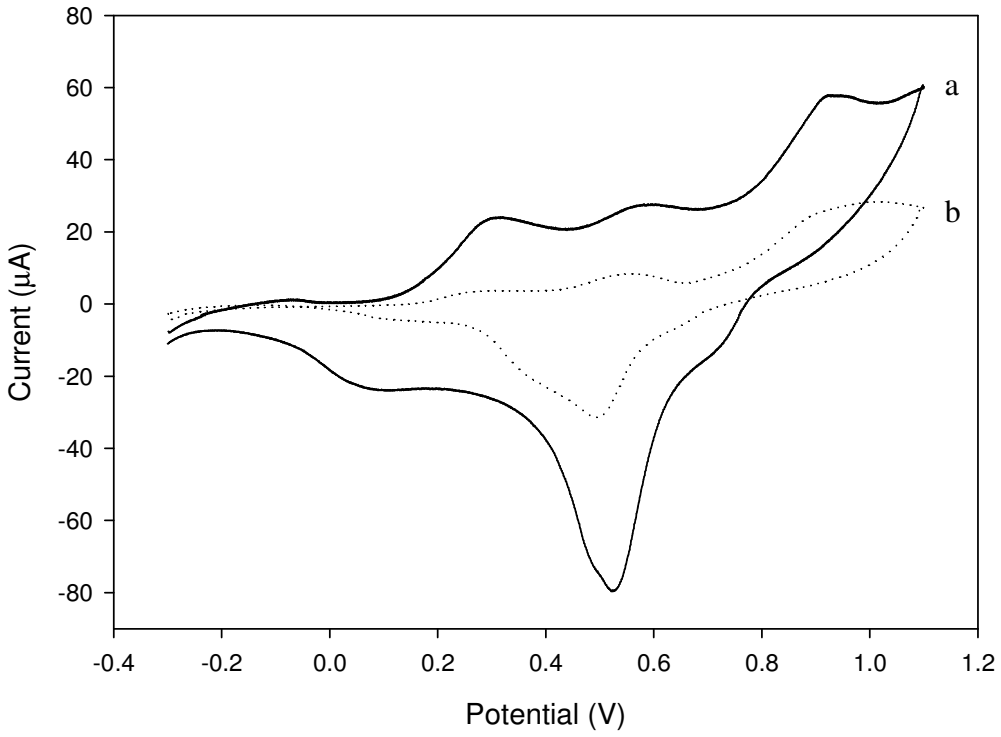

Figure 4.7: A) Cyclic voltammetry of PANI-coated PS CC in a sealed µchannel under stop-flow conditions 0.1 V/s scan rate vs. Ag/AgCl (1 M HCl electrolyte) after 10 voltammetric cycles were performed electrochemically polymerising a thin PANI coating. The coating ensured a consistent connection between the PANI/PS opal structure and the gold WE. A control is also shown B) CV of a bare PS CC in a sealed µchannel under stop-flow conditions 0.1 V/s scan rate vs. Ag/AgCl (1 M HCl electrolyte) after electrochemical polymerisation of aniline to mimic the same electrical connection.

Figure 4.7A shows the electrochemistry observed in the µchannel in the presence of the PANI-PS opal after electrochemical synthesis of the PANI-based electrical connection. Typical PANI electrochemistry was obtained that is dominated by the chemically polymerised PANI-PS opal structure. To verify this electrochemistry was primarily attributed to the electrochemically-deposited PANI, PANI was electrochemically grown to induce the same electrochemical connection from the

integrated WE to a bare PS opal as a control, Figure 4.7B. It can be seen in the control experiment that, although PANI electrochemistry is evident, currents were significantly lower than those resulting from the PANI-coated PS opal structure, demonstrating that the electrochemistry of the chemically polymerised PANI-PS opal structure could be successfully accessed by this approach.

To further characterise the PANI structure a scan rate study was performed from 0.010 – 0.1 V/s (Figure 4.8). The oxidation peaks can be assigned to the oxidation of the Pernigraniline Salt (PS) to Emeraldine Salt (ES) and ES to Leucoemeraldine Salt (LS), peaks A and B respectively. The main peaks upon reversing the scan correspond to the reduction of LS to ES and ES to PS, peaks C and D respectively. Figure 4.9 is a graph of i_p vs. scan rate. It shows a high linearity (R^2 = 0.995), demonstrating a well-behaved, stable thin PANI coating with fast electron transfer.

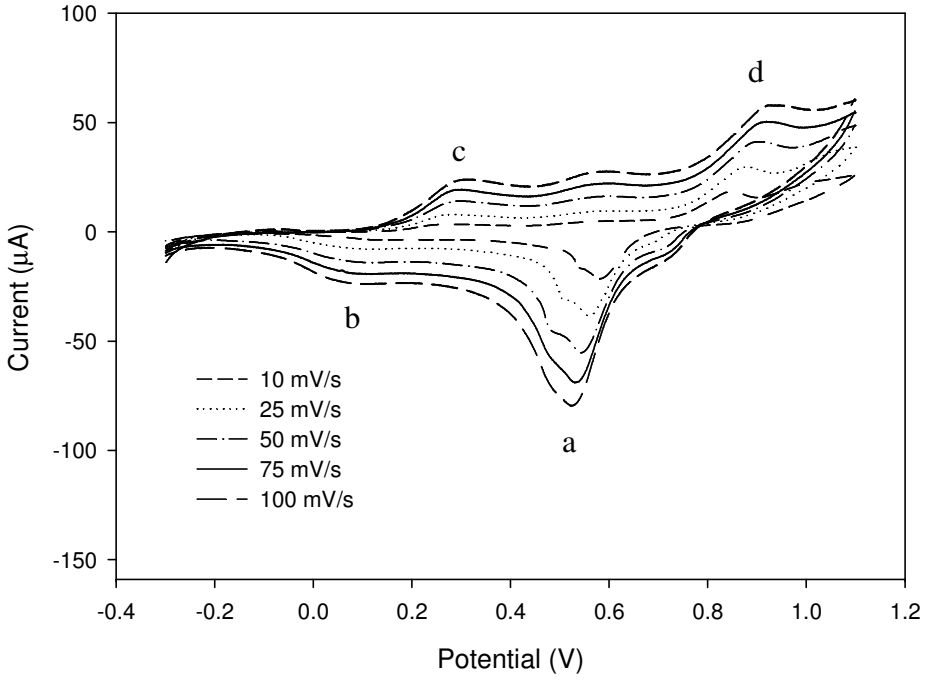

Figure 4.8: Details a scan rate study performed from 0.010 – 0.1 V/s in HCl (1M) vs. Ag/AgCl of PANI-coated PS CC after voltammetry cycling in aniline. Flow rate: 1 μL/min.

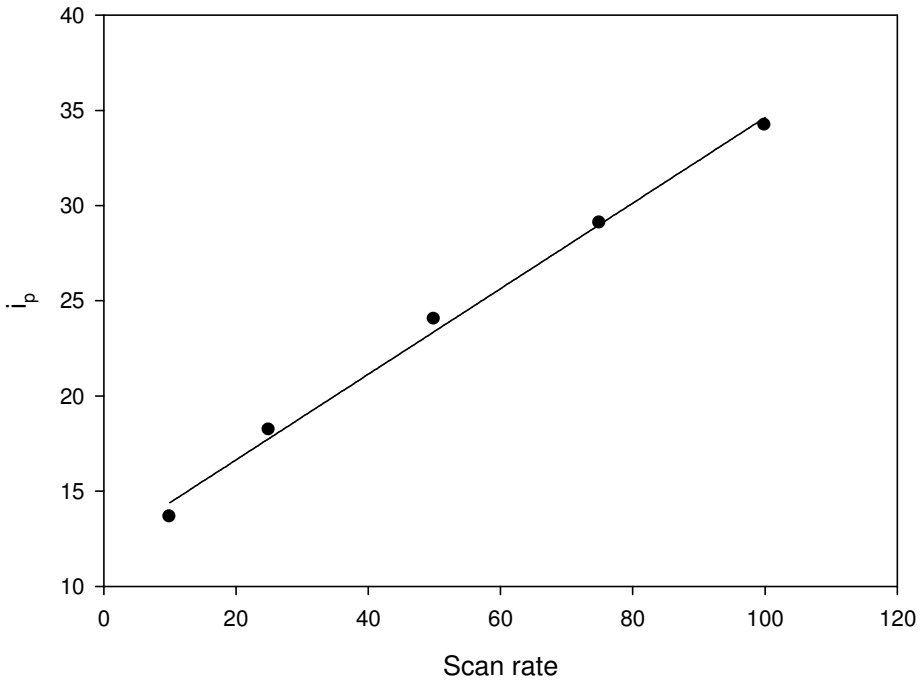

Figure 4.9: Graph of i_p vs. scan rate i_p & scan rate data obtained from scan rate study detailed in Figure 4.8 above. R^2 = 0.995.

4.4 Conclusion

A novel chemical polymerisation strategy was developed to produce a PANI 3D ordered opal structure which was homogenous throughout its structure. This method allowed template-directed chemical polymerisation of aniline throughout the length and depth of the μchannel to yield a PANI-PS opal structure, of which the core comprised a fcc PS uCC. Electrochemical polymerisation ensured a consistent connection between the PANI-PS composite and the integrated gold WE, ensuring that the PANI opal structure was fully addressable electrochemically. The outer PANI coating of this new structure was characterised electrochemically. It displayed stable electrochemistry with fast electron transfer. Thus, this approach is a viable route to obtaining homogenous, electrochemically-responsive, ordered, flow-through materials directly within μchannels where applications including controlled release, electrochemically-controllable stationary phases and electrochemical sensing directly in μchannels.

Chapter 5

Controllable Hydrophobicity of PANI Films through Dopant Variation

5.1 Introduction

During electrochemical and chemical polymerisation of ICP materials in a strong acid, formation of the most conducting form of polymers is achieved. Specifically for polyaniline (PANI) this results in the formation of a polaron site in the polymer backbone with a positive charge [166, 212]. To balance this charge incorporation of ions to "dope" the polymer backbone results, as shown in Figure 1.2 of Chapter 1. The variation of dopant incorporated has been shown to affect morphology and conductivity of ICP materials [213-216]. For example using sodium dodecyl benzene sulfonate (SDBS) as dopant during chemical polymerisation of PANI, Fan *et al.* [217] demonstrated the fabrication of leaf-like PANI morphologies which were 4 µm in length and approximately 3 µm in width. Here, SDBS acted as both dopant and soft template during polymerisation. At a concentration of 2 mM leaf-like PANI structures resulted. The leaf-like structures demonstrated were in contrast to the fibrillar morphology associated with HCl doped PANI films [218] showing that the presence of SDBS during polymerisation directed PANI growth into a leaf-like morphology. Tohumcu *et al.* [219] showed that the conductivity of polypyrrole films could be affected by dopants type. Here, incorporation of dodecylbenzene suphonic acid (DBSA) showed the highest conductivity (3.1×10^{-1} S/cm) in comparison to other dopants such as tetrafluoroborate (BF_4^-) (7.1×10^{-7} S/cm), perchlorate (ClO_4^-) (1.7×10^{-7} S/cm) and oxalate ($C_2O_4^{2-}$) (1.1×10^{-4} S/cm).

Similarly the hydrophobicity of ICP films (i.e. the degree to which they will interact with water where hydrophilic surfaces will display low water contact angle and increased interaction with water and hydrophobic surfaces will display high water contact angles and decreased interaction with water) can also be manipulated by variation in dopant type. For example Leng *et al.* [220] demonstrated an ICP film

with super-hydrophobic/super-hydrophilic characteristics. Here, PANI films with switchable hydrophobicity were achieved via incorporation of a surfactant, sodium dodecyl sulphate (SDS), during polymerisation. Variations in the molar ratio of SDS:aniline during polymerisation was shown to affect the resulting hydrophobicity. At very low SDS concentrations, SDS was incorporated only intermittently, resulting in no change in hydrophobicity. At high SDS concentrations an excess of unbound SDS was deposited on the surface of the polymer film, resulting in a super-hydrophilic polymer surface. At an optimised SDS:aniline ratio of between 0.03-0.05, reproducible PANI films with switchable hydrophobicity were fabricated which in the doped Emeraldine Salt (ES) state were ultra-hydrophobic and upon dedoping to the Emeraldine Base (EB) became super-hydrophilic. Similarly, Zhu *et al.* [221] demonstrated the fabrication of PANI-coated fibres with switchable hydrophobicity. The PANI coated fibres were chemically polymerised in the presence of perfluorosebacic acid (PFSEA). Upon dedoping in the presence of ammonia gas for 1 min, the surface became demonstrably hydrophilic in contrast to the super-hydrophobic surface measured in the doped state [221]. Unfortunately, the films discussed were chemically polymerised and were not electrochemically controllable. A limitation of chemical fabrication of ICP films is that their stimulus is limited to a chemical treatment, which severely limits their potential for stimulus induced renewal once in use.

Electrochemically polymerised films offer the potential to overcome this limitation, as they are electrochemically addressable and so can be subjected to electrochemical as well as a chemical pH-induced stimulus, which has far greater practical potential for stimulus-induced renewal. Isakksson *et al.* [222] spin-coated PANI films doped with dodecylbenzenesulfonic acid (DBSA) which were electrochemically

addressable. Variation in applied potential resulted in switches in oxidation states from Leucoemeraldine (LS) to ES and finally Pernigraniline (PS), where only small changes in hydrophilicity were observed.

In contrast to PANI films, considerably more success has been demonstrated with polypyrrole (PPY) films. Xu *et al.* [223] fabricated electrochemically addressable perfluorootanesulfonate (PFOS) doped PPY films which under negative potential, -0.6 V vs. Ag/AgCl, were reduced to neutral polypyrrole (PPY) films. This process could then be reversed by applying a positive potential, +1.0 V vs. Ag/AgCl. Water contact angle (WCA) of the oxidised PPY film was super-hydrophobic with neutral PPY films displaying super-hydrophilicity illustrating the huge potential for electrochemically varied hydrophobity of ICP films.

The potential of surface modification and induction of super-hydrophobic characteristics in ICP films have also been demonstrated through nano-structuring. Sun *et al.* [224] fabricated flower-like polyaniline films through the addition of valine as a dopant during chemical polymerisation to produce super-hydrophobic nano-structured PANI films [224]. Similarly Zhu *et al.* [225] demonstrated the fabrication of 3D-boxlike micro-structures from 1D-nanofibres in the presence of perflourosebacic acid (PFSEA) which acted as both dopant and soft template. The resulting 3D-boxlike structures also demonstrated super-hydrophobic WCA. Rambutan-like hollow PANI spheres were fabricated with super-hydrophobic WCA as high as 164.5^{o}. Here the hollow PANI spheres were fabricated in the presence of perfluorooctane sulfonic acid which acted as dopant and soft template during chemical polymerisation [226]. The morphology variations detailed for ICP films have successfully induced super-hydrophobic surfaces. However, the limitation of

such modification is the lack of stimulus-response during use, similar to that of chemical polymerisation methods.

In this work PANI films were electrochemically polymerised in the presence of HCl or HCl/SDS. The SDS concentration was manipulated to elucidate controlled hydrophobicity based on salt/base forms of the polymer. Morphology and roughness of resulting HCl-doped and SDS-doped PANI films were compared with similar morphology noted (fibrillar) with an increase in fibre length and diameter noted for SDS-doped films. Similarly, an increase in roughness of SDS-doped films was noted in comparison to HCl-doped films likely due to the soft templating effect of SDS during polymerisation. The potential applications of ICP films with controlled hydrophobicity include ultrafiltration membrane [77, 227] and anti-corrosion coatings [228, 229] as well as actuation [230, 231].

5.2 Experimental

5.2.1 Materials

As per Method Section 3.2.1.

5.2.2 Instrumentation

As per Methods Section 4.2.2 with the following addition, profilometry was performed using a Veeco Dektak V200Si profilometer. WCA measurements were performed on an Artray and Navitar camera FTA32 video with 2.0 datalog software.

5.2.3 Methods

5.2.3.1 Gold working electrode fabrication

As per Method Section 3.2.3.1 on a bare glass slide without masking.

5.2.3.2 Polyaniline polymerisation

As per Method Section 3.2.3.3 with the following addition polymerisation was achieved over 90 or 400 s on a gold sputtered glass slide. An example of the amperometric growth for both HCl-doped (dashed line) and SDS-doped (black line) is shown in Figure 5.1 below.

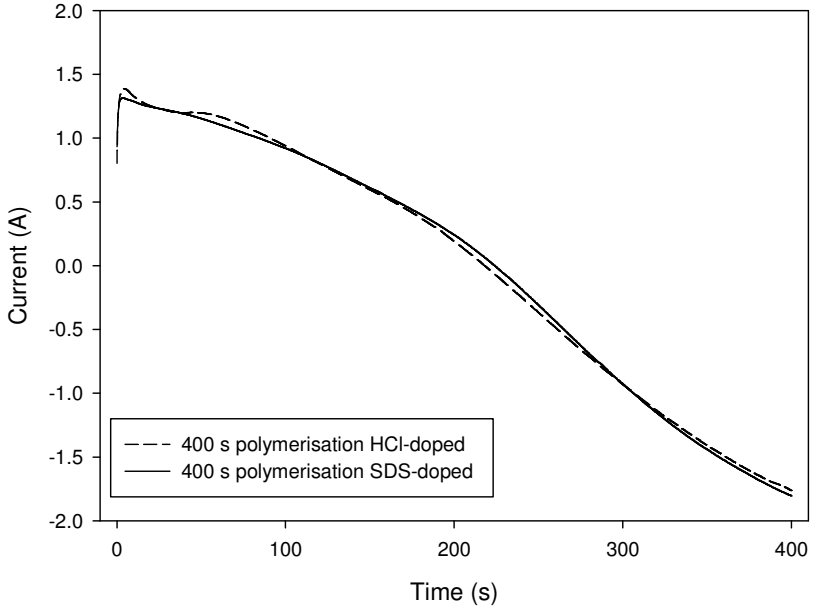

Figure 5.1: Amperometric It curve demonstrating the polymerisation of HCl-doped and SDS-doped PANI films. Polymerisation was undertaken in a 3 electrode cell with a gold WE, Ag/AgCl reference and platinum mesh counter electrode. The potential was held at 0.9 V for 400 s with Electrolyte 1 M HCl and when doping with SDS a molar ratio of 0.02 Aniline:SDS was used.

After polymerisation, PANI films were air dried at room temperature for 30 min. Addition of SDS to aniline/acid solutions was undertaken using an optimum molar ratio of 0.02 optimised from Leng *et al*. [220]. After polymerisation PANI films were placed in HCl (1 M) and held at a fixed potential for 30 s to oxidise or reduce the polymer film. Potentials used vs. Ag/AgCl were -0.2 V for LS, +0.5 V for ES, and +0.9 V for PS. Each of the salts were then dedoped chemically by immersing in NaOH (1 M) for 30 s. This resulted in the corresponding base states of Leucoemeraldine Base (LB), Emeraldine Base (EB) and Pernigraniline Base (PB). The polymer was then dried at 65^{o}C for 30 min.

5.2.3.3 Water contact angle measurements

WCA measurements were performed in triplicate on each sample (n=3) resulting in 9 total readings. Deionised water (D.I.) was placed on the surface of each PANI thin film and the resulting contact angle was measured immediately after water drop placement (5 µL), time zero, t_o and 60 s after water drop placement, t_{60}.

5.2.3.4 Profilometry

Profilometry was performed on samples using a Veeco Dektak V200Si profilometer over 2.3 mm, using a 2.5 µm tip and 5 mg of force, with 5 readings obtained for PANI samples prepared as per Method Section 5.2.3.2. Optimised PANI films in ES and EB oxidation states HCl-doped and SDS-doped were measured and compared.

5.3 Results and Discussion

Initial fabrication to obtain PANI films with switchable hydrophobicity employed a similar experimental design to that of Leng *et al.* [220]. However, in contrast to the chemical polymerisation method employed by Leng, an electrochemical polymerisation was used in this work. The use of electrochemical polymerisation was key to enable electrochemical addressability of the fabricated PANI films subsequent to polymerisation. This allowed for electrochemical stimulus to be applied, inducing variation of oxidation state resulting in a variation in hydrophobicity. Fabrication of PANI films was performed over 400 s before the PANI films were electrochemically varied between oxidation states from -0.2V for Leucoemeraldine salt (LS), +0.5V for Emeraldine salt (ES) and +0.9V for Pernigraniline salt (PS) vs. Ag/AgCl in HCl (1 M). To compare the salt and base forms of each polymer film, films were placed in NaOH (1 M) to induce chemical dedoping. WCA measurements were then performed on each redox state in both salt (doped) and base (dedoped) forms to allow the hydrophobicity of each surface to be determined.

5.3.1 Variation in oxidation state

PANI films were electrochemically varied between oxidation states using amperometry. To obtain the correct potentials for each oxidation state a cyclic voltammogram (CV) of a typical Cl-doped PANI film in HCl (1 M) vs. Ag/AgCl was performed as shown in Figure 5.2. The observed CV of the PANI film shows the uptake and release of ions from the HCl electrolyte into and from the film. In the CV, each peak is labelled illustrating the gradual change in oxidation state of the polymer. Interference from the gold WE is shown circled in yellow. Gold electrochemistry

was evident on the CV (see control) as the PANI did not fully isolate the underlying gold electrode from the electrolyte solution.

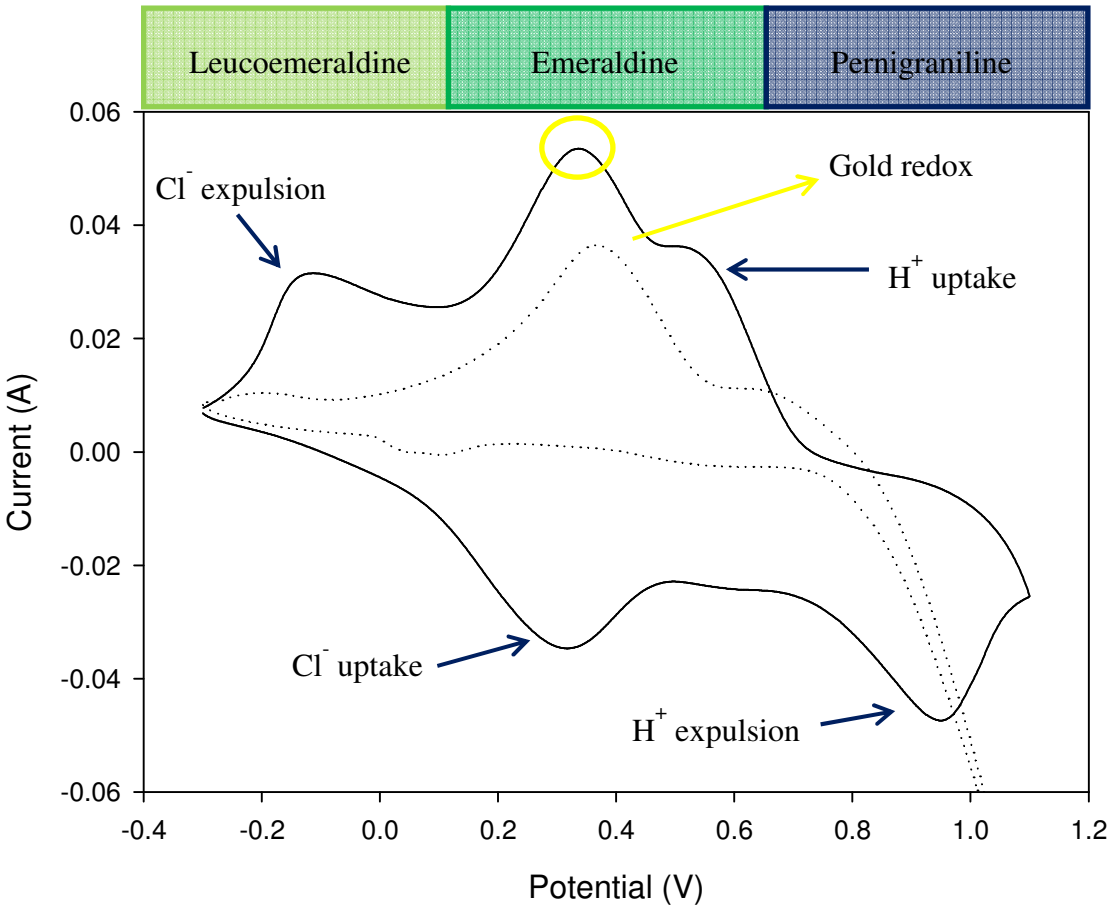

Figure 5.2: CV of bulk Cl-doped PANI film in 1 M HCl scan rate 0.1 V with uptake and release of ions shown as a result of gradual variation in oxidation state (continuous black line). The PANI film was electrochemically polymerised for 400 s at +0.9 V and subsequently cycled between 0.3 – 1.1 V vs. Ag/AgCl reference electrode with a Pt mesh counter. The colour of each oxidation state is also indicated. A CV of a bare gold electrode in 1 M HCl cycled from 0.3 – 1.1 V vs. Ag/AgCl reference electrode with a Pt mesh counter is also demonstrated. Peak at ~0.4 V corresponds to the reduction of gold oxide (dotted line).

With variation in oxidation state switching of the polymers was noted visually. Figure 5.3 shows three photographs demonstrating the colour change of the Cl-doped PANI films after electrochemical switching between states, with the colour seen to change from green in the LS state to turquoise for ES and finally to dark blue for the PS oxidation state. Each PANI film was held at a fixed potential after polymerisation for 30 s and the resulting optical variation in the film was noted.

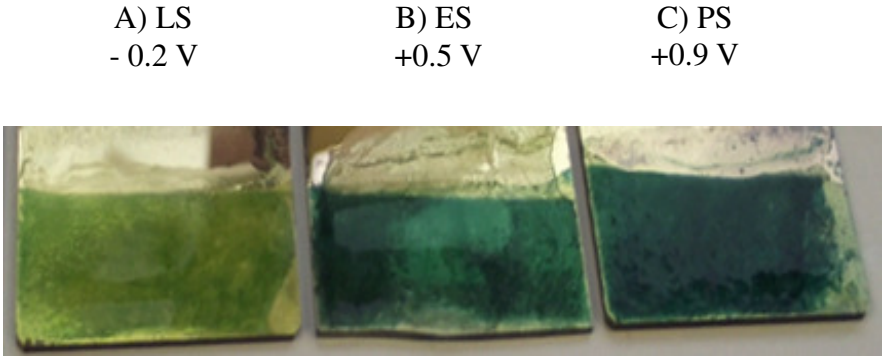

Figure 5.3: Photographs of A) LS, B) ES and C) PS PANI thin films electrochemically polymerised for 90 s. Variation in oxidation state was achieved in 1 M HCl electrolyte in a 3 electrode cell with potentials held at -0.2 V for LS +0.5 V for ES and +0.9 V for PS vs. Ag/AgCl reference electrode with a Pt mesh counter electrode. The resulting optical switching of films is illustrated.

After variation in the oxidation state the WCA was measured for each PANI redox state in both the salt and base form. Films were tested in triplicate at t_o when the water droplet was placed on the surface of the film. It was found that each of the Cl-doped PANI films displayed hydrophilic surface chemistry. Figure 5.4 details the summary of WCA measurements of Cl-doped PANI films. As expected, the Cl-doped PANI films displayed minimal variation in hydrophobicity between oxidation states, which would limit their use in controlling and/or switching hydrophobicity.

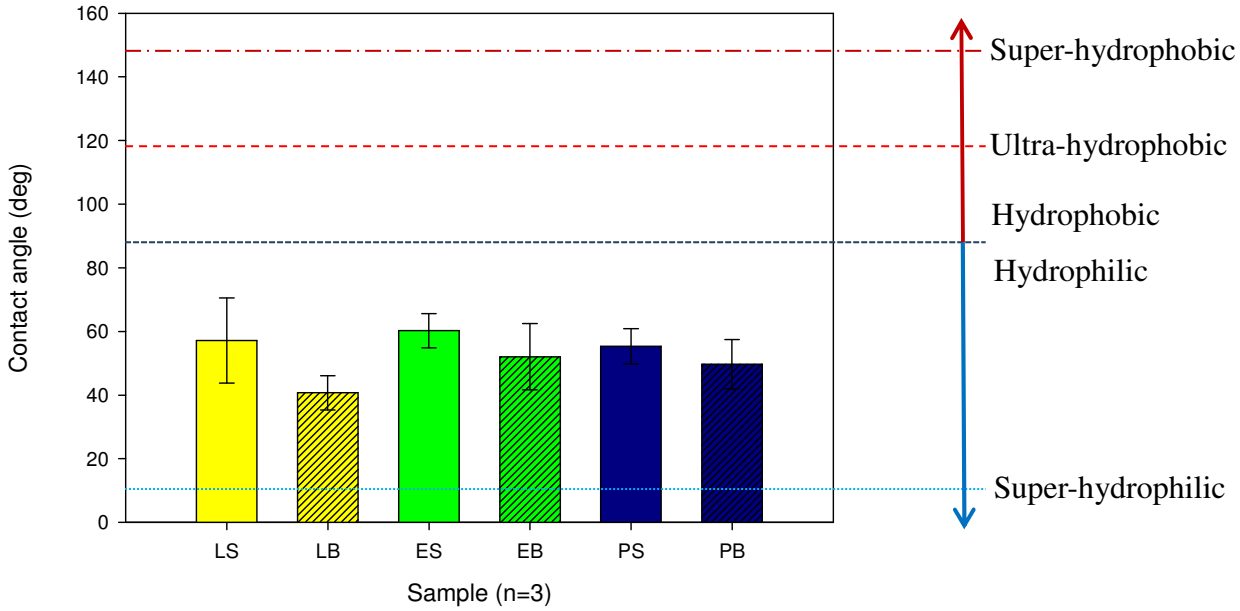

Figure 5.4: Initial WCA measurements for the salts and bases of Cl-doped PANI in its difference oxidation states. LS is shown in yellow, LB shown in yellow with dashed black lines, ES shown in green, EB shown in green with black dashed lines, PS and PB shown in blue and blue with black dashed lines. Hydrophobicity scale developed from Reference [232]. D.I. water was dropped (5 µL) on the surface of each polymer film after drying at 65°C for 30 min. The WCA was immediately measured when the droplet hit the polymer surface.

After measuring WCA, the surfaces of the Cl-doped PANI films were imaged by SEM analysis as shown in Figure 5.5A-C & 5.6A-C. No change in morphology was observed across the different states. PANI films displayed bulk fibrillar morphology interwoven uniformly across the electrode area (10 mm x 25 mm). Accompanying the SEM images are examples of the corresponding WCA measurements for each oxidation state, Figure 5.5, previously summarised in Figure 5.4.

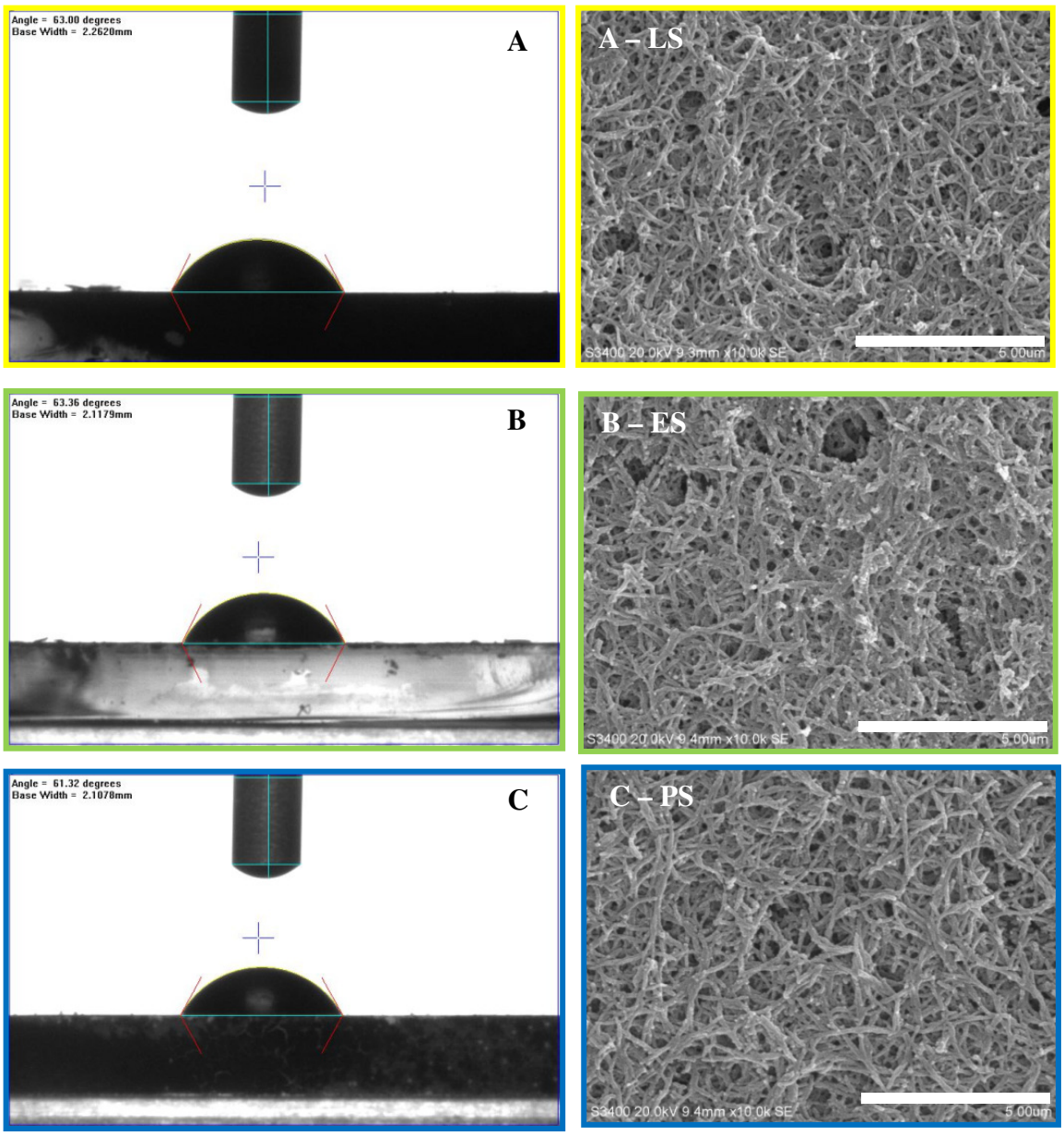

Figure 5.5: WCA measurements and SEM images of A) LS B) ES and C) PS of Cl-doped PANI after electrochemical variation of the redox state in a three electrode cell gold WE, Ag/AgCl reference and Pt mesh counter (1 M HCl electrolyte). Mag. 10.0 k; Scale bar 5.00 µm.

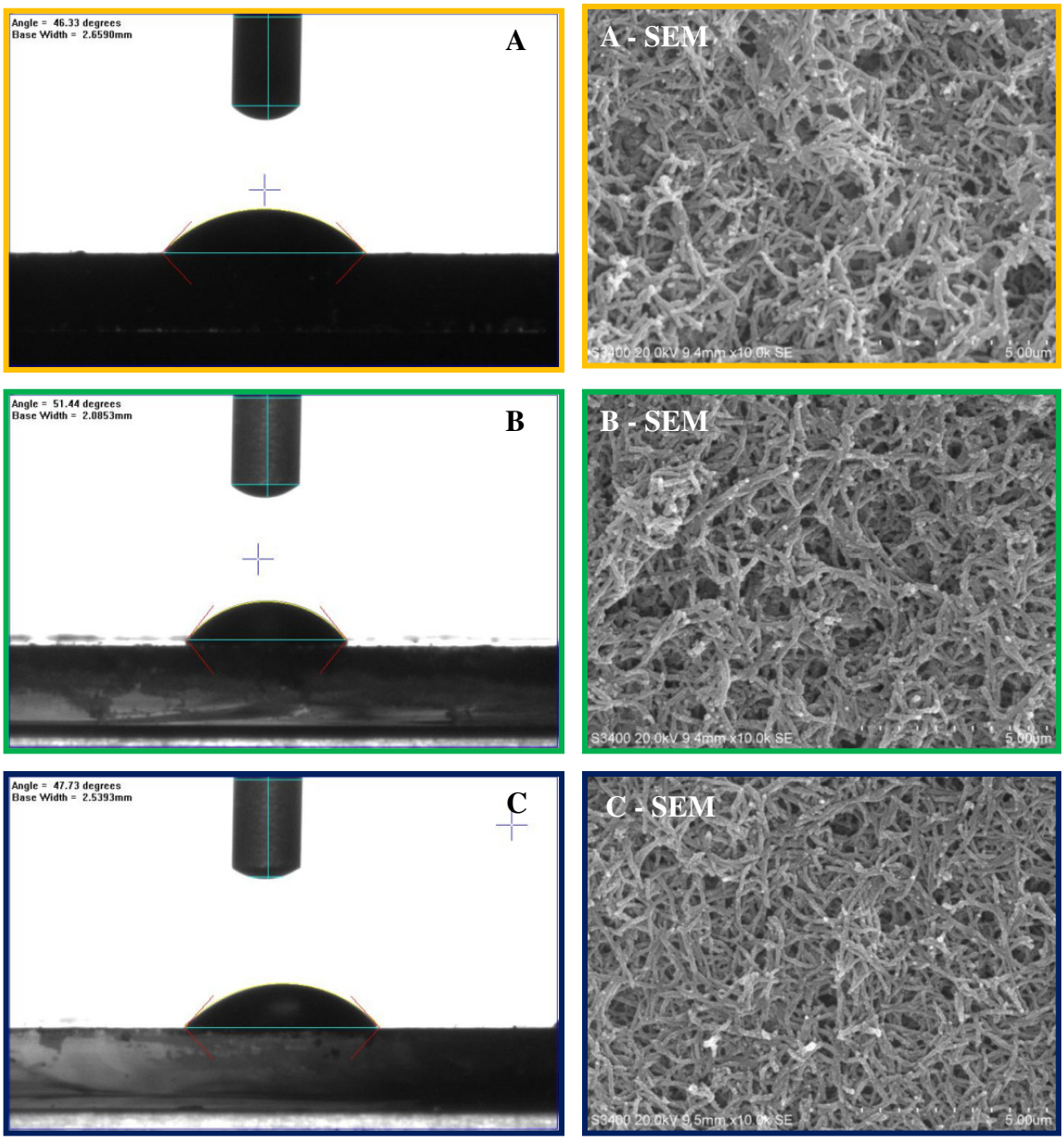

Figure 5.6: WCA measurements and SEM images of WCA measurements and SEM images of A) LB B) EB and C) PB of Cl-doped PANI after electrochemical variation of the redox state in a three electrode cell gold WE, Ag/AgCl reference and Pt mesh counter (1 M HCl electrolyte).Subsequently films were dedoped in NaOH (1 M) to induce the base form. Mag. 10.0 k; Scale bar 5.00 µm.

5.3.2 Electrochemical polymerisation with SDS as dopant and soft template

After WCA measurements of Cl-doped PANI, an alternative dopant SDS was incorporated during polymerisation. Initial concentrations used were comparable to that described by Leng *et al.* [220]. Through incorporation of the SDS surfactant as a dopant to balance the charge in the polymer network, Leng *et al.* demonstrated a hydrophobic PANI film. Upon dedoping it was observed that the PANI film was switched to its hydrophilic state. This switchability was attributed to the change in orientation of the SDS hydrophilic head group away from the polymer network upon dedoping as a result of the neutral charge. In this present work the SDS concentration was optimised beginning with a similar concentration used by Leng *et al*. (molar ratio = 0.03). It was found that when used in conjunction with electrochemical fabrication this resulted in too high a concentration of SDS giving a hydrophilic surface due to excess unbound SDS deposited on the PANI surface. As the excess SDS was unbound it could freely orientate with either the hydrophobic tail or hydrophilic head group towards the surface, so that when the polymer came into contact with an aqueous environment a hydrophilic surface resulted. Upon reducing the SDS concentration to a molar ratio of 0.003 the resulting surface was again hydrophilic, indicating insufficient SDS to induce hydrophobicity. It was found for electrochemical polymerisation employed in this work, a molar ratio of 0.02 was optimum to produce a PANI film which was initially hydrophobic and as such was appropriate to induced switchable hydrophobicity.

Once the molar ratio of SDS:aniline was optimised the WCA measurements of the films were measured at t_o. It was found that for each of the salt forms of the polymers, hydrophobicity was increased from ~60^o for Cl-doped PANI films (meaning films were hydrophilic) data presented in Figure 5.4 to 133± 2^o for LS,

134±2° for ES and 131±3° for PS films incorporating SDS as a dopant, as shown in Figure 5.7, resulting in ultra-hydrophobic surfaces. For each of the base forms the WCA again indicated that the surfaces had become more hydrophobic, with LB 103±20°, EB 66±15° and PB 65±12°. Each of the SDS-doped base forms presented displayed reduced stability in comparison to salt forms, as shown by the large standard deviation. The reduced stability was due to re-hydration of the polymer surface over time. Each PANI film was dried at 65°C for 30 min before WCA measurements to ensure consistency during comparison of oxidation states and SDS-/HCl-doped films. Due to the drying step involved during film preparation, the water droplet gradually soaked into the hydrophilic films. As a result an extended time was needed to allow the droplet to stabilise on the polymer surface; this was in keeping with the findings of Leng *et al.* [220].

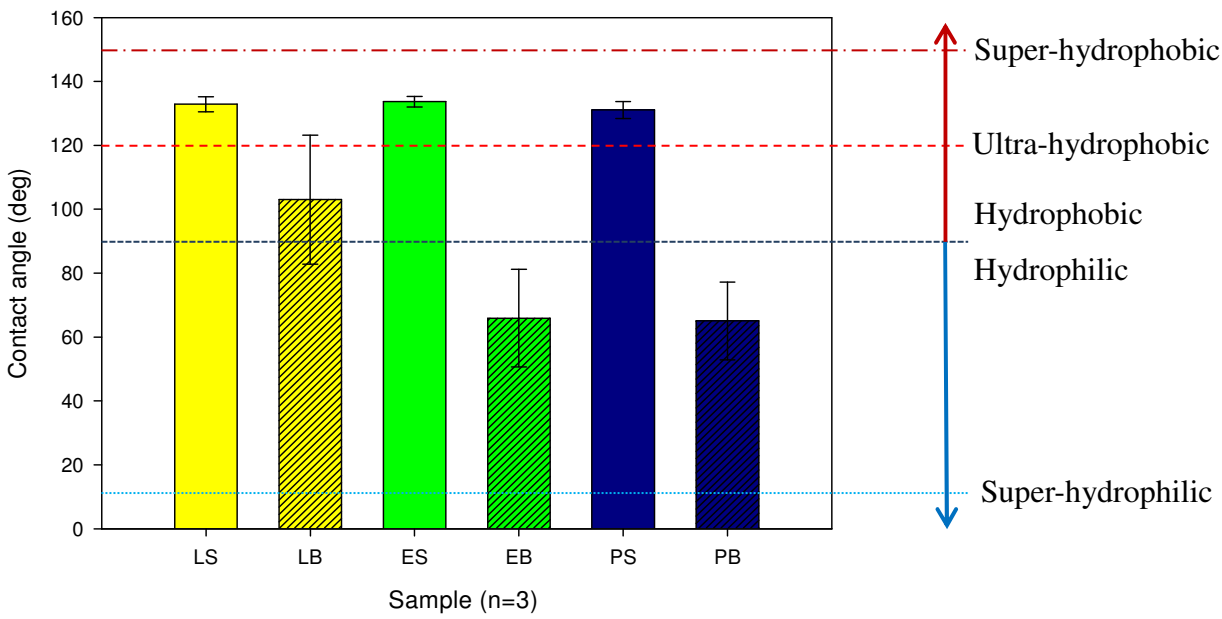

Figure 5.7: t_o WCA measurements for SDS-doped PANI films, oxidation state denominations as per Figure 5.4. D.I. water (5 µL) was dropped on the surface of

each polymer film after drying at 65°C for 30 min. The WCA was immediately measured when the droplet hit the polymer surface.

The WCA of the films was therefore measured again at t_{60} for both the salt and base forms to investigate the extent to which the droplets permeated in PANI coatings over time. The resulting WCA measurements at t_{60} are shown in Figure 5.8. The salt forms of LS & ES remained stable between ~130-120° indicating the ultra-hydrophobicity of the films was not affected over this time scale upon exposure to water. A significant decrease in WCA for the base forms was noted with LB falling to 81±14° from 103±20° for LB, 26±26° from 66±15° for EB and 32±24° from 65±12° for PB showing significant difference in hydrophobicity over a 60 s timeframe. As these were the most hydrophilic films initially, they were most likely to be susceptible to water permeation, and so the results obtained here were to be expected. The large standard deviations for LB, EB and PB were as a result of a large number of the films reaching 0° WCA after 60 s with all samples reaching WCA of 0° after 90/120 s.

Unfortunately, SDS-doping did not result in a change in hydrophobicity between oxidation states. Unfortunately, this meant that SDS-doping did not result in surfaces which switched from hydrophobic to hydrophilic with variation of oxidation state as had been hoped. However, these hydrophobic/hydrophilic switches were noted between the salt and the base forms of each oxidation state. While this dedoping from salt to base normally occurs due to a pH stimulus, Morrin *et al*. [33] has also shown at pH 6.8 that this can occur via application of an electrochemical stimulus, which would also enable the goal of this research to be achieved. The largest change in WCA between the salt and base form was noted for the oxidation state of Emeraldine over the 60 s time period with WCA measurements of 134±1° (ultra-

hydrophobic) and 26±26° (hydrophilic) recorded respectively. This resulted in a WCA difference of 108° after 60 s. On average the difference in hydrophobicity between ES and EB was the highest, the stability of the salt form in the ultra-hydrophobic region was higher than that of PS, and the EB form reached super-hydrophilic WCA quicker than that of LB. The Emeraldine oxidation state was therefore chosen as the optimum due to this stability and large difference in hydrophobicity between salt and base forms.

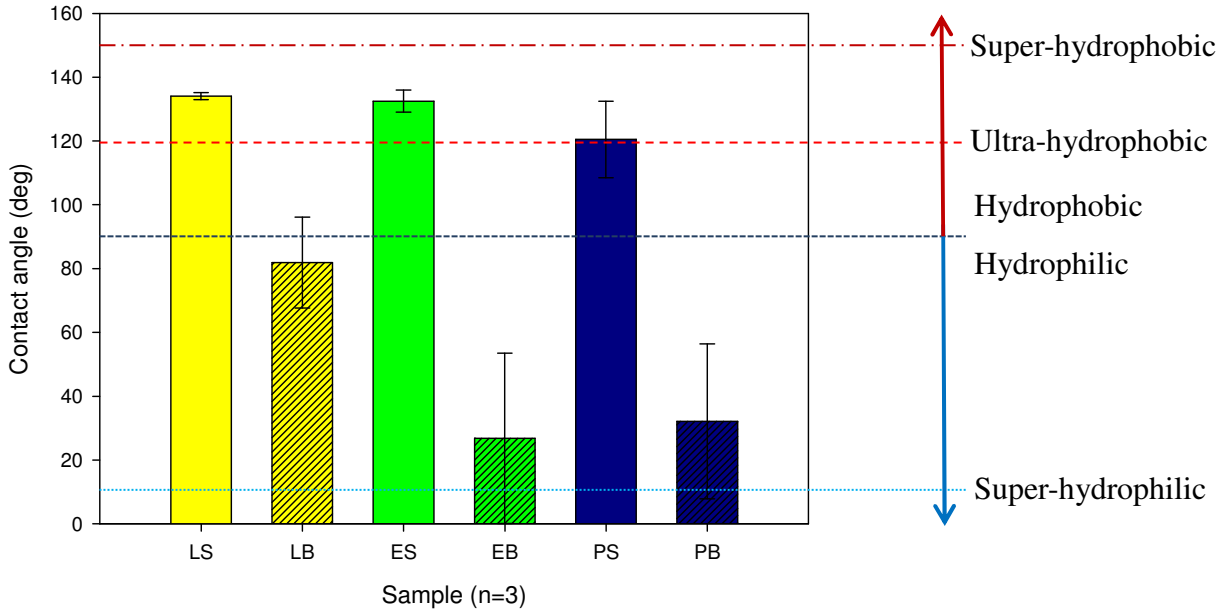

Figure 5.8: WCA measurements after 60 s for SDS-doped PANI films, oxidation state as per Figure 5.4. D.I. water (5 µL) was dropped on the surface of each polymer film (5 µL) after drying at 65°C for 30 min. The WCA was measured at t_{60}, 60 s after the droplet hit the polymer surface.

After measuring WCA the surface of the resulting ES and EB PANI films were imaged by SEM analysis to compare the morphology of HCl-doped to SDS-doped films, shown in Figure 5.9. The surface of the SDS-doped film was fibrillar in morphology comparable to that of the HCl-doped films. Importantly the size

(diameter and length) of fibres formed in the presence of SDS were thicker and longer, as can be seen from Figure 5.9A in comparison to HCl-doped PANI fibre, Figure 5.9B, and as previously noted, significant improvements in hydrophobicity of PANI films were noted with SDS modification. WCA measurements for doped and dedoped SDS-doped PANI films are visually illustrated in Figure 5.10.

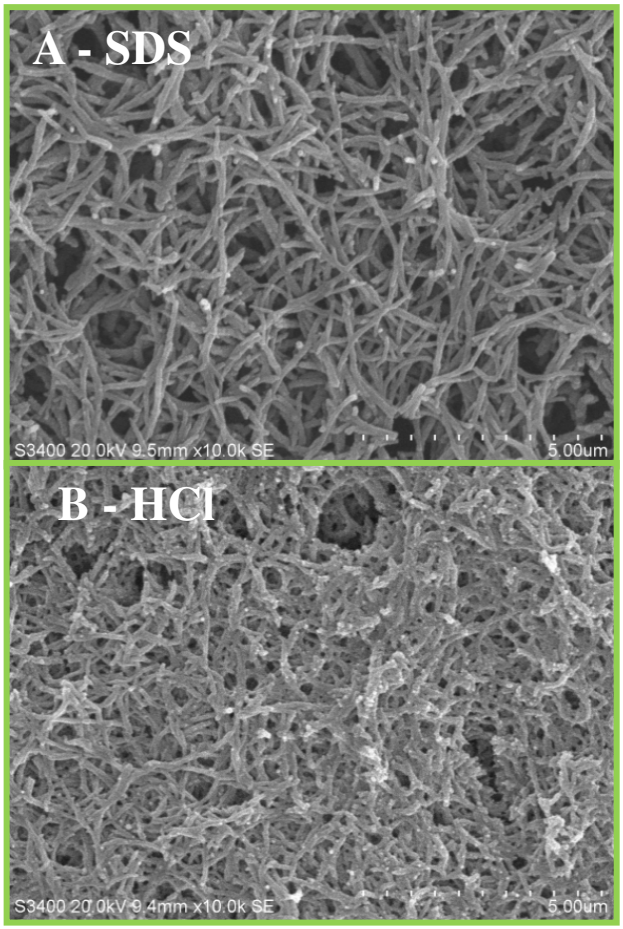

Figure 5.9: SEM images of A) Cl^- doped PANI film and B) SDS doped PANI film in ES oxidation state polymerisation was over 400 s at a fixed potential of 0.9 V in a three electrode cell gold WE, Pt mesh counter and Ag/AgCl reference 1M HCl electrolyte. In the case of SDS-doped films a molar ratio of 0.02 aniline:SDS was used. Mag. 10.0 k; Scale bar 5.00 µm.

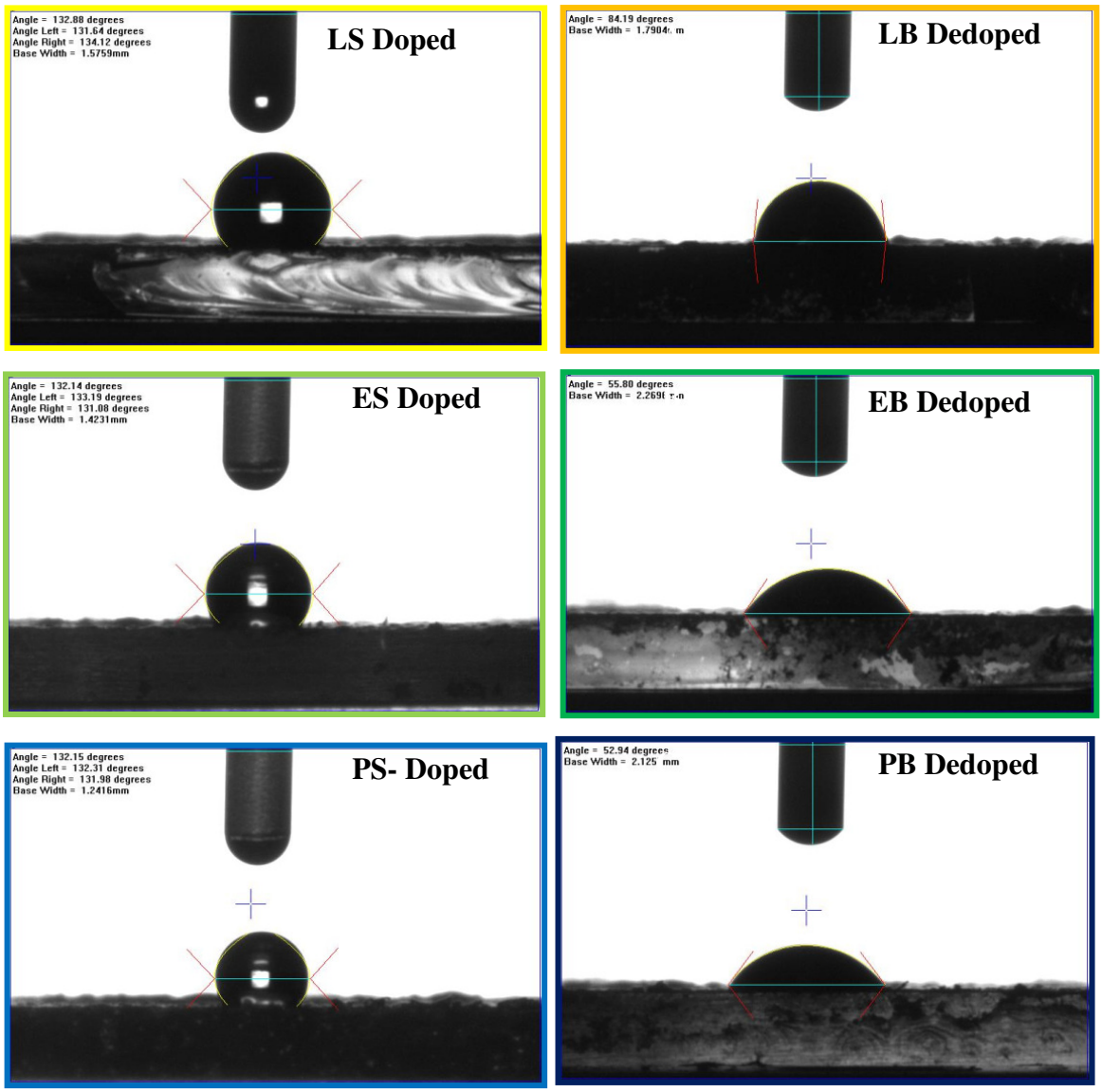

Figure 5.10: WCA measurements at t_{60} and LS & LB ES & EB and PS & PB oxidation states with SDS incorporated. PANI films were polymerised over 400 s at a fixed potential of 0.9 V in a three electrode cell gold WE, Pt mesh counter and Ag/AgCl reference 1M HCl electrolyte. In the case of SDS-doped films a molar ratio of 0.02 aniline:SDS was used. Oxidation states were varied electrochemically in 1 M HCl electrolyte in the same 3 electrode cell with potentials held at -0.2 V for LS +0.5 V for ES and +0.9 V for PS. PANI films were placed in 1M NaOH for 30 s to dedope.

Although PANI film morphology was comparable for SDS- and HCl-doped films i.e. fibrillar, changes in the surface topography/roughness were likely to have resulted from SDS incorporation due the associated soft templating. To investigate this,

profilometry measurements of the PANI film surfaces for ES and EB SDS-doped and HCl-doped were performed.

To examine if the morphology changes observed for Cl-doped and SDS-doped PANI films had a significant effect on the surface roughness/topography the average roughness (R_a) of the optimised films were measured using profilometry. Upon obtaining the R_a values a large difference between the films was noted. In the case of PANI films with no SDS present, the R_a for both the salt and base forms of Emeraldine oxidation state gave a mean of 246±96 nm for ES (shown in green) and 285±71 for EB (shown in blue) as illustrated in Figure 5.11. When these values were compared to PANI films polymerised in the presence of SDS the R_a increased by an order of magnitude to a mean of 2114±475 nm for ES (shown in green with black dashed lines) and 1901±441 nm for EB (shown in blue with dashed black lines) illustrated in Figure 5.11. The presence of SDS during polymerisation therefore was observed to have had a dual role of dopant and soft template. It was hypothesised that SDS aided in structurally directing polymerisation resulting in a significantly rougher surface of the SDS doped PANI film similarly to what was previously observed [220, 233].

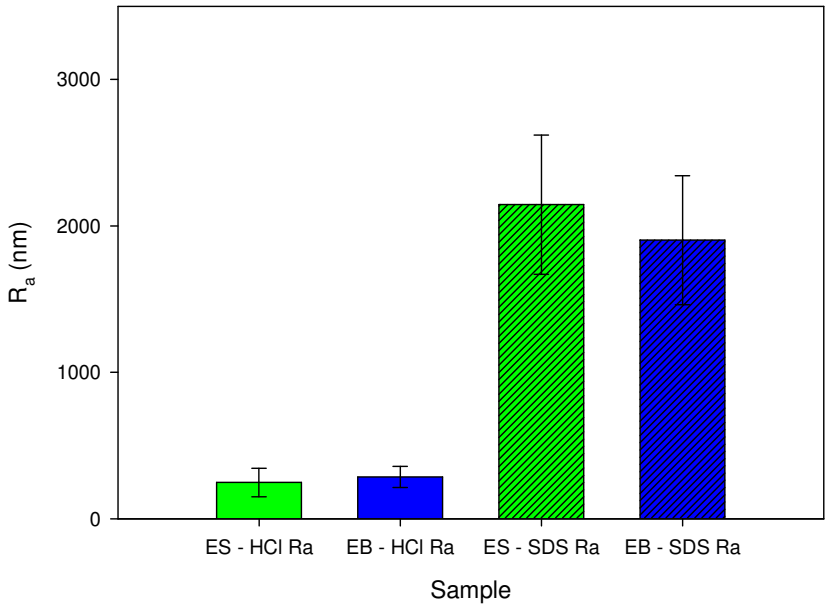

Figure 5.11: R_a measurement for ES (green) and EB (blue) HCl-doped films and ES (green with dashed black lines) and EB (blue with dashed black line) SDS-doped films. Readings were performed over 2.3 mm, using a 2.5 µm tip and 5 mg of force n = 5.

5.4 Conclusion

The successful fabrication of electrochemically polymerised PANI films with controllable hydrophobicity is demonstrated here. PANI films were fabricated on gold-sputtered working electrodes with HCl- or SDS-dopant. To characterise the PANI films, a comparison of WCA measurements and R_a measurements of Cl-doped and SDS-doped PANI films was undertaken. It was found that SDS-doped PANI films displayed ultra-hydrophobic WCA when doped, which upon dedoping displayed hydrophobic initially before a gradual decline in WCA over 60 s to give hydrophilic PANI surfaces. HCl-doped PANI films displayed hydrophilic surface chemistry with little variation upon doping/dedoping. On comparing R_a SDS-doped ICP films displayed an order of magnitude higher roughness to that of the HCl-doped films, likely due to the soft templating effect of SDS during polymerisation. Fibrillar morphology was noted for both HCl-doped and SDS-doped films. However, thicker and longer fibres were noted for SDS-doped films likely due to the soft templating effect of SDS during polymerisation. Potential applications for PANI films with controllable hydrophobicity include anti-corrosion coatings, actuation and novel stationary phase material.

Chapter 6

Conclusions & Future Work

6.1 Conclusion and future work

The incorporation of polymers within μfluidic platforms offer a unique analytical tool for sensing, separation controlled release and extraction with shortened analysis times, high sensitivity and low sample consumption, as explored in the literature review in Chapter 1. One of the limitations of current μfluidic platforms highlighted is the lack of radial homogeneity in polymers fabricated in situ. A potential strategy to overcome these heterogeneities is to template during fabrication to achieve 3D ordered flow through polymer structures within the μchannel. Chapter 2 of this work focused on achieving this potential by developing a fabrication method for reproducible 3D ordered templates within a confined geometric area. The template function was to structurally direct intrinsically conducting polymer (ICP) polymerisation resulting in an electrochemically addressable, reproducible, 3D ordered ICP flow through material housed within a μfluidic channel. This work successfully illustrated a facile fabrication method for 3D ordered, reproducible polystyrene (PS) colloidal crystal (CC) templates. The method developed offers tailored templates with unimodal and bimodal order fabricated within 12 h in a μchannel. Template fabrication was demonstrated to be robust as template formation was achieved within multiple μchannel depths (35 – 220 μm) and lengths (5 – 40 mm). Perhaps a limitation of this work is the focus on PS sphere template fabrications; future work could investigate the potential of silica sphere CC fabrication to determine if the associated packing method was applicable to silica spheres as well as PS spheres as demonstrated here. The advantage of using silica is the high temperature resistance and reduced shrinkage of the material which makes CC of silica ideal for deposition applications at elevated temperatures [234, 235]. With the increased surface area associated with bimodal CC templating methods,

there has been significant focus recently on further increasing surface area through fabrication of multimodal materials [119, 236]. Figure 6.1 shows an example a multimodal PS sphere aggregate fabricated during this work, where the PS sphere aggregation was achieved through electrostatic interaction. Although not explored further in this work, these multimodal aggregate structures offer unique high surface area template applications such as energy storage [236, 237] and separation [238], where higher order structure is not required.

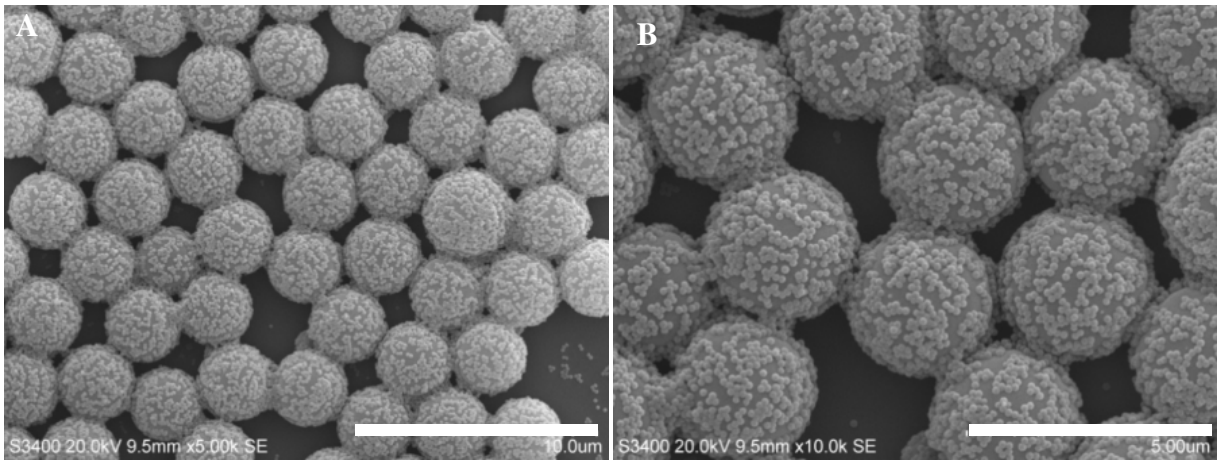

Figure 6.1: SEM image of multimodal PS sphere structures of macro: 3 µm and nano: 222 nm PS spheres. A) Mag 5.00 k; scale bar: 10.0 µm and B) Mag 10.0 k; scale bar: 5.00 µm.

Throughout this thesis, the specific aim of template fabrication was for the template directed growth of electrochemically active, flow through, ICP structures. Template directed ICP polymerisation of polyaniline (PANI) was achieved within µchannels and the resulting PANI monoliths were observed to have reproducible 3D order. Chapter 3 focused on optimisation of electrochemical polymerisation time through a PS CC within a µchannel. Polymerisation time was varied between 90 – 360 s resulting in PANI structures from collapsed inverse opal at short polymerisation times (90 s), inverse opal PANI monolith with defined flow through pores at

optimum polymerisation times (210 s) to core shell PANI particles at excessive polymerisation times (360 s). However, poor homogeneity of the final ICP monolith throughout the depth of the µchannel was observed, as shown Figure 6.2. To overcome this limitation bulk chemical and surface confined chemical polymerisation methods were investigated, as detailed in Chapter 4. It was demonstrated that surface confined chemical polymerisation offered the most homogeneous polymerisation method with 3D order noted within a 180 µm depth µchannel. The resulting homogeneous, 3D order PANI film was electrochemically active with fast electron transfer and high stability within a sealed µchannel.

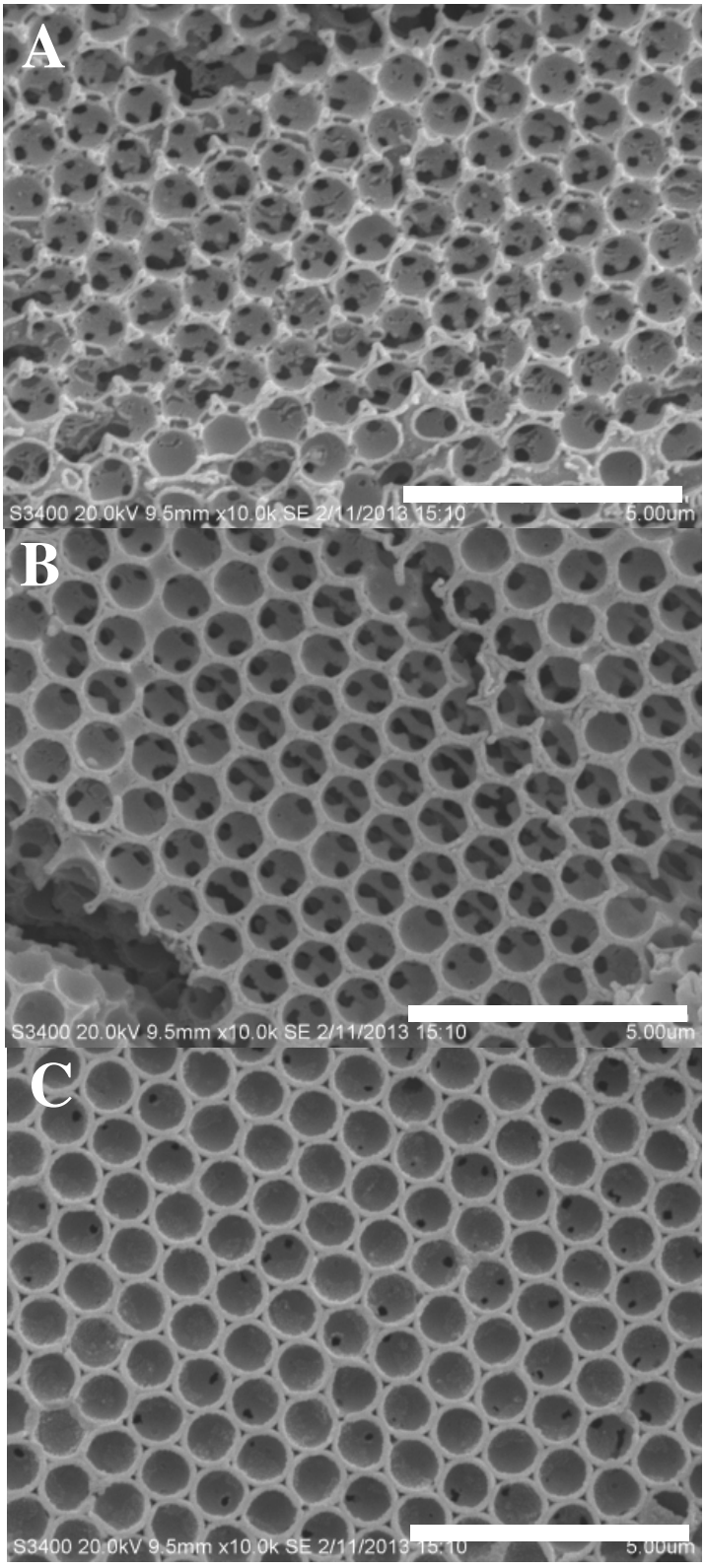

Figure 6.2: SEM images of PANI monolith structures after removal of PS template. A) Upper layer of inverse opal furthest from the working electrode (WE). B) Middle layer of inverse opal. D) Lower layer of inverse opal, closest to WE. Mag: 10.0 k; scale bar; 5.00 µm. PANI films were polymerised in a three electrode cell at a fixed

potential of 0.9 V for 210 s with a gold WE, Ag/AgCl reference electrode and Pt mesh counter electrode.

The PANI flow through material presented in this work is a significant step forward in ICP fabrication within µfluidic platforms. The method offers a reproducible templating and a chemical polymerisation method which offers an electrochemically addressable ICP material which has potential application for lab-on-chip separation, sensing, extraction or drug delivery. To realise these applications, future study should initially focus on optimisation of the µfluidic platforms design particularly the electrode integration in order to maximise the area of the WE, which would augment the separation, sensing, extraction or drug delivery capabilities of the ICP material. Here, the WE length used was 5 mm which proved highly effective in illustrating the potential and optimising the homogeneous ICP network. Power *et al.* demonstrated that no significant increase in internal resistance (IR) was noted when a WE length of 5 mm was used with uniform electrochemical PANI growth over this length scale (resulting in polymer depths of up to 50 % of the µchannel depth) [57]. With this in mind Figure 6.3 demonstrates a potential µchip design which incorporates two µchannels into a µfluidic housing. By introducing a second channel the design can overcome any increase in IR associated with increasing WE length. The dual µchannel design, where µchannels are separated by 1 mm, incorporates bridges at 5 mm intervals to counter any increase in IR. The bridges allow movement of electrolyte and electrical connection between each µchannel connecting the integrated electrodes in µchannel 1 & 2. With slight modification of sputter mask designs similar to those used in Chapter 2 - 4 of this work, isolation of WE and counter/reference electrodes the length and width of each µchannel with associated connections to a potentiostat are possible. With this µfluidic platform design a

significant increase in WE length can be envisaged with increased potential for separation, sensing, extraction or drug delivery applications.

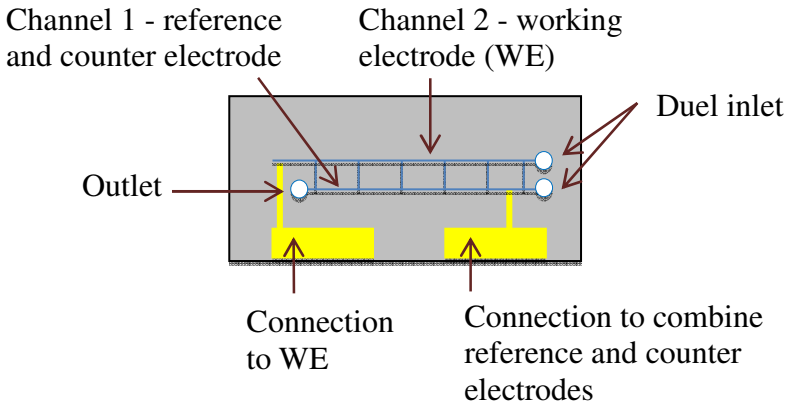

Figure 6.3: Schematic of potential µfluidic platform housing fully integrated electrodes on chip within a dual µchannel design.

More sophisticated µfluidic components such as ICP based pumps employed by Wallace and Diamond *et al.* [99] could also be used for flow control. Fabricating a µfluidic device with reduced dead volume and highly controlled fluid flow would eliminate the need for external pump incorporation, which would in turn increase the applicability of the final devices. Moreover, the resulting reduction in dead volume would increase potential applicability in analytical separations. Due to the low (normally nano-litre) volumes associated with µfluidic analysis, preventing excess dead volume is essential to prevent band broadening which would hinder the potential application of any µfluidic platform in separations.

Chapter 5 of this work investigated the variation of dopant during electrochemically polymerisation for PANI films. Here the hydrophobicity was varied through addition of a surfactant, sodium dodecyl sulphate (SDS). When SDS was incorporated and the

PANI films were doped (in the salt form) Leucoemeraldine Salt (LS), Emeraldine Salt (ES) and Pernigraniline Salt (PS) displayed ultra-hydrophobic water contact angles (WCA). Upon dedoping (base form) Leucoemeraldine Base (LB), Emeraldine Base (EB) and Pernigraniline Base (PB) displayed hydrophobic WCA at time zero, t_o but after 60s, t_{60} hydrophilic WCA measurements were observed. Highest switchability between hydrophobic and hydrophilic states was noted between the ES and EB forms with over 100^o WCA difference after t_{60}. An example of the WCA measurements is presented in Figure 6.4.

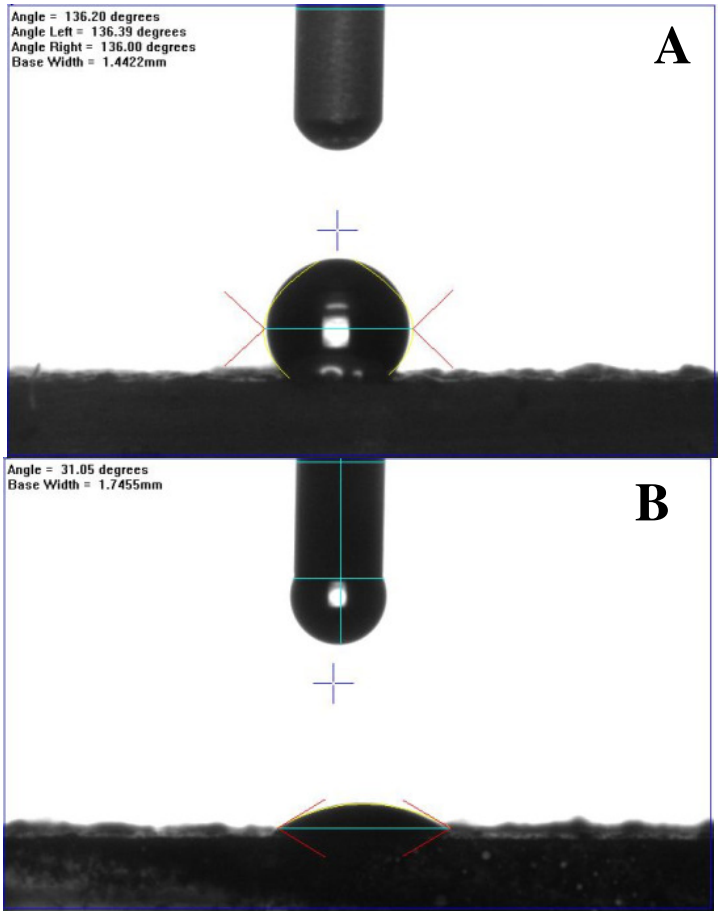

Figure 6.4: WCA measurements for A) PANI film doped ES oxidation state and B) PANI film dedoped EB. Deionised water (D.I.) was dropped on the polymer surface and WCA was measured after t_{60}.

During SEM analysis the surface of SDS- and Cl-doped PANI films, similar fibrillar morphologies were noted. Variations in the fibre length and thickness were visible during analysis of the SDS-doped films in comparison to HCl-doped, likely due to the soft templating effect of SDS addition during polymerisation. Profilometry of the SDS- and HCl-doped films indicated a further difference with the roughness where SDS-doped PANI films had an order of magnitude higher roughness than Cl-doped PANI films.

Potential applications for SDS-doped PANI films presented in Chapter 5 could be within ultrafiltration (UF) membrane applications. The interest in ICP materials as membrane coatings is due to the higher water flux due to increased hydrophilicity and % particle rejection noted as a result of electrostatic interactions upon incorporation of ICPs [239].The incorporation of ICP materials in UF applications has shown to be successful to date [77, 227].

This work has advanced on-chip applications of ICP's and enabled technical realisation of proposed lab-on-chip approaches. While many research groups have developed novel methods to incorporate and control ICPs within lab-on-chip platforms using chemical and electrochemical polymerisation, fabrication and characterisation of ordered 3D flow-through ICP structures had not been investigated in detail. This work focused on this limitation and fabrication of high surface area flow-through ICP materials were achieved by firstly, fabricating a novel templating method within the confines of a μchannel and secondly, structural direct polymerisation of an ICP, PANI, in a μchannel. Subsequently the resulting 3D order and electrochemical control of the PANI flow through materials was demonstrated. The novel template directed polymerisation method detailed in this work offers a

unique approach which can be used in multiple μchannel designs and with the resulting 3D ordered material potentially useful in a broad number of applications.

6.2 List of Publications and Presentations

6.2.1 Publications

- B. Gorey, J. Galineau, B. White, M.R. Smyth, A. Morrin, *Inverse-opal conducting polymer monoliths in microfluidic channels*, Electroanalysis, 2012, 6, 1318 – 1323.
- B. Gorey, M.R. Smyth, B. White, A. Morrin, *Fabrication of homogenous three dimensionally ordered conducting polymer-polystyrene opal structures in microfluidic channels.* Journal of Materials Chemistry C 2014, **2**, 6004-6009.
- B. Gorey, M.R. Smyth, B. White, A. Morrin, *Fabrication of a 3-dimensional nanostructured binary colloidal crystal within a confined channel,* 2014, DOI: 10.1016/j.jcis.2014.08.032.

6.2.2 Oral presentations

- *Polyaniline: A Versatile Conducting Polymer*, Irish Polymer and Material Conference, UCD, Dublin Ireland 30th April 2014.
- *Controlled Surface Morphologies for Conducting Polymer Monolith On-Chip,* Analytical Research Forum, ARF, GlaxoSmithKline & the University of Hertfordshire, UK, 7th July 2013
- *Controlled Surface Morphologies for Conducting Polymer Monolith On-Chip,* Conference of Analytical Science in Ireland, CASi, University College Cork, Cork, Ireland, 1st July 2013.

6.2.3 Poster presentations

- *Inverse-opal conducting polymer monoliths in microfluidic channels,* 14th International Conference on Electroanalysis, ESEAC, Portoroz, Slovenia, 3rd June 2012.

- *Development of 3-Dimensional nanostructured unimodal and bimodal polystyrene templates*, Eirelec, Adare, Co. Limerick, Ireland, 18th May 2011.
- *Production of Polystyrene spheres for use as a templating material for polyaniline monolith structures,* Conference on Analytical Sciences, *CASi,* DCU, Dublin, Ireland, 21st February 2011.

6.3 References

1. Bhadra, S., Khastgir, D., Singha, N.K., and Lee, J.H., 2009. Progress in preparation, processing and applications of polyaniline. *Progress in Polymer Science*. **34**(8): p. 783-810.
2. Bhadra, S., Singha, N.K., and Khastgir, D., 2006. Polyaniline by new miniemulsion polymerization and the effect of reducing agent on conductivity. *Synthetic Metals*. **156**(16): p. 1148-1154.
3. Sharma, P.S., Pietrzyk-Le, A., D'Souza, F., and Kutner, W., 2012. Electrochemically synthesized polymers in molecular imprinting for chemical sensing. *Analytical and Bioanalytical Chemistry*. **402**(10): p. 3177-3204.
4. Chiam, Y.S., Lim, K.S., Harun, S.W., Gan, S.N., and Phang, S.W., 2014. Conducting polymer coated optical microfiber sensor for alcohol detection. *Sensors and Actuators A: Physical*. **205**: p. 58-62.
5. Korba, K., Pelit, L., Pelit, F.O., Özdokur, K.V., Ertaş, H., Eroğlu, A.E., and Ertaş, F., 2013. Preparation and characterization of sodium dodecyl sulfate doped polypyrrole solid phase micro extraction fiber and its application to endocrine disruptor pesticide analysis. *Journal of Chromatography B*. **929**: p. 90-96.
6. Jiang, S., Sun, Y., Cui, X., Huang, X., He, Y., Ji, S., Shi, W., and Ge, D., 2013. Enhanced drug loading capacity of polypyrrole nanowire network for controlled drug release. *Synthetic Metals*. **163**: p. 19-23.
7. Patil, A.O., Heeger, A.J., and Wudl, F., 1988. Optical properties of conducting polymers. *Chemical Reviews*. **88**(1): p. 183-200.

8. Nalwa, H.S., 1997. Handbook of organic conductive molecules & polymers: conductive polymers, transport, photophysics & applications vol 4. *Recherche*. **67**: p. 02.

9. Wallace, G.G., Teasdale, P.R., Spinks, G.M., and Kane-Maguire, L.A.P., *Conductive electroactive polymers: intelligent polymer systems*. 2008: CRC press.

10. Holze, R., 2011. Copolymers-A refined way to tailor intrinsically conducting polymers1, 2. *Electrochimica Acta*. **56**(28): p. 10479-10492.

11. Anu Prathap, M.U., Thakur, B., Sawant, S.N., and Srivastava, R., 2011. Synthesis of mesostructured polyaniline using mixed surfactants, anionic sodium dodecylsulfate and non-ionic polymers and their applications in H_2O_2 and glucose sensing. *Colloids and Surfaces B: Biointerfaces*. **89**: p. 108-116.

12. Ge, H. and Wallace, G., 1989. Characterization of novel conducting polymeric stationary phases and electrochemically controlled high-performance liquid chromatography. *Analytical Chemistry*. **61**(21): p. 2391-2394.

13. Deinhammer, R.S., Shimazu, K., and Porter, M.D., 1991. Ion chromatographic separations using step and linear voltage waveforms at a charge-controllable polymeric stationary phase. *Analytical Chemistry*. **63**(17): p. 1889-1894.

14. Yakes, B.J., Keller, D.W., and Porter, M.D., 2010. Electrochemically modulated liquid chromatographic separation of triazines and the effect of pH on retention. *Journal of Chromatography A*. **1217**(26): p. 4395-4401.

15. Nyström, G., Strømme, M., Sjödin, M., and Nyholm, L., 2012. Rapid potential step charging of paper-based polypyrrole energy storage devices. *Electrochimica Acta*. **70**: p. 91-97.

16. Razaq, A., Nyholm, L., Sjödin, M., Strømme, M., and Mihranyan, A., 2011. Paper-Based Energy-Storage Devices Comprising Carbon Fiber-Reinforced Polypyrrole-Cladophora Nanocellulose Composite Electrodes. *Advanced Energy Materials*. **2**(4): p. 445-454.

17. Gurunathan, K., Murugan, A.V., Marimuthu, R., Mulik, U.P., and Amalnerkar, D.P., 1999. Electrochemically synthesised conducting polymeric materials for applications towards technology in electronics, optoelectronics and energy storage devices. *Materials Chemistry and Physics*. **61**(3): p. 173-191.

18. Svirskis, D., Travas-Sejdic, J., Rodgers, A., and Garg, S., 2010. Electrochemically controlled drug delivery based on intrinsically conducting polymers. *Journal of Controlled Release*. **146**(1): p. 6-15.

19. Richardson, R.T., Wise, A.K., Thompson, B.C., Flynn, B.O., Atkinson, P.J., Fretwell, N.J., Fallon, J.B., Wallace, G.G., Shepherd, R.K., and Clark, G.M., 2009. Polypyrrole-coated electrodes for the delivery of charge and neurotrophins to cochlear neurons. *Biomaterials*. **30**(13): p. 2614-2624.

20. Abidian, M.R. and Martin, D.C., 2009. Multifunctional nanobiomaterials for neural interfaces. *Advanced Functional Materials*. **19**(4): p. 573-585.

21. Wadhwa, R., Lagenaur, C.F., and Cui, X.T., 2006. Electrochemically controlled release of dexamethasone from conducting polymer polypyrrole coated electrode. *Journal of Controlled Release*. **110**(3): p. 531-541.

22. Crowley, K., Morrin, A., Hernandez, A., O'Malley, E., Whitten, P.G., Wallace, G.G., Smyth, M.R., and Killard, A.J., 2008. Fabrication of an ammonia gas sensor using inkjet-printed polyaniline nanoparticles. *Talanta*. **77**(2): p. 710-717.

23. Huang, J., Virji, S., Weiller, B.H., and Kaner, R.B., 2003. Polyaniline nanofibers: facile synthesis and chemical sensors. *Journal of the American Chemical Society*. **125**(2): p. 314-315.

24. Stamenov, P., Madathil, R., and Coey, J.M.D., 2012. Dynamic response of ammonia sensors constructed from polyaniline nanofibre films with varying morphology. *Sensors and Actuators B: Chemical*. **161**(1): p. 989-999.

25. Tavoli, F. and Alizadeh, N., 2013. Optical ammonia gas sensor based on nanostructure dye-doped polypyrrole. *Sensors and Actuators B: Chemical*. **176**: p. 761-767.

26. Umana, M. and Waller, J., 1986. Protein-modified electrodes. The glucose oxidase/polypyrrole system. *Analytical Chemistry*. **58**(14): p. 2979-2983.

27. Bai, H. and Shi, G., 2007. Gas sensors based on conducting polymers. *Sensors*. **7**(3): p. 267-307.

28. Gupta, N., Sharma, S., Mir, I.A., and Kumar, D., 2006. Advances in sensors based on conducting polymers. *Journal of Scientific & Industrial Research*. **65**: p. 549-557.

29. Safarnavadeh, V., Zare, K., and Fakhari, A.R., 2013. Capability of parasulfonato calix [6] arene, as an anion dopant, and organic solvents in enhancing the sensitivity and loading of glucose oxidase (GOx) on polypyrrole film in a biosensor: A comparative study. *Biosensors and Bioelectronics*. **49**: p. 159-163.

30. Khan, R., Solanki, P.R., Kaushik, A., Singh, S., Ahmad, S., and Malhotra, B., 2009. Cholesterol biosensor based on electrochemically prepared polyaniline conducting polymer film in presence of a nonionic surfactant. *Journal of polymer research*. **16**(4): p. 363-373.

31. Matharu, Z., Sumana, G., Arya, S.K., Singh, S.P., Gupta, V., and Malhotra, B.D., 2007. Polyaniline Langmuir-Blodgett film based cholesterol biosensor. *Langmuir*. **23**(26): p. 13188-13192.

32. Michira, I., Akinyeye, R., Somerset, V., Klink, M., Sekota, M., Al-Ahmed, A., Baker, P., and Iwuoha, E. *Synthesis, characterisation of novel polyaniline nanomaterials and application in amperometric biosensors*. in *Macromolecular symposia*. 2007. Wiley Online Library.

33. Morrin, A., Ngamna, O., Killard, A.J., Moulton, S.E., Smyth, M.R., and Wallace, G.G., 2005. An amperometric enzyme biosensor fabricated from polyaniline nanoparticles. *Electroanalysis*. **17**(5-6): p. 423-430.

34. Gerard, M., Chaubey, A., and Malhotra, B., 2002. Application of conducting polymers to biosensors. *Biosensors and Bioelectronics*. **17**(5): p. 345-359.

35. Dhand, C., Das, M., Datta, M., and Malhotra, B., 2011. Recent advances in polyaniline based biosensors. *Biosensors and Bioelectronics*. **26**(6): p. 2811-2821.

36. Tahir, Z.M., Alocilja, E.C., and Grooms, D.L., 2005. Polyaniline synthesis and its biosensor application. *Biosensors and Bioelectronics*. **20**(8): p. 1690-1695.

37. Ramanavičius, A., Ramanavičienė, A., and Malinauskas, A., 2006. Electrochemical sensors based on conducting polymer-polypyrrole. *Electrochimica Acta*. **51**(27): p. 6025-6037.

38. Zhang, Y., Kim, J.J., Chen, D., Tuller, H.L., and Rutledge, G.C., 2014. Electrospun polyaniline fibers as highly sensitive room temperature chemiresistive sensors for ammonia and nitrogen dioxide gases. *Advanced Functional Materials*. **24**(25): p. 4005-4014.

39. Palod, P.A., Pandey, S.S., Hayase, S., and Singh, V., 2014. Template-Assisted Electrochemical Growth of Polypyrrole Nanotubes for Development of High Sensitivity Glucose Biosensor. *Applied biochemistry and biotechnology*: p. 1-14.

40. Thompson, B.C., Moulton, S.E., Ding, J., Richardson, R., Cameron, A., O'Leary, S., Wallace, G.G., and Clark, G.M., 2006. Optimising the incorporation and release of a neurotrophic factor using conducting polypyrrole. *Journal of Controlled Release*. **116**(3): p. 285-294.

41. Hepel, M. and Mahdavi, F., 1997. Application of the electrochemical quartz crystal microbalance for electrochemically controlled binding and release of chlorpromazine from conductive polymer matrix. *Microchemical journal*. **56**(1): p. 54-64.

42. Zinger, B. and Miller, L.L., 1984. Timed release of chemicals from polypyrrole films. *Journal of the American Chemical Society*. **106**(22): p. 6861-6863.

43. Kontturi, K., Pentti, P., and Sundholm, G., 1998. Polypyrrole as a model membrane for drug delivery. *Journal of Electroanalytical Chemistry*. **453**(1): p. 231-238.

44. Miller, L.L. and Zhou, X., 1987. Poly (N-methylpyrrolylium) poly (styrenesulfonate)-a conductive, electrically switchable cation exchanger that

cathodically binds and anodically releases dopamine. *Macromolecules*. **20**(7): p. 1594-1597.

45. Abidian, M.R., Kim, D.H., and Martin, D.C., 2006. Conducting-polymer nanotubes for controlled drug release. *Advanced Materials*. **18**(4): p. 405-409.

46. George, P.M., LaVan, D.A., Burdick, J.A., Chen, C.Y., Liang, E., and Langer, R., 2006. Electrically controlled drug delivery from biotin-doped conductive polypyrrole. *Advanced Materials*. **18**(5): p. 577-581.

47. Sun, Y.-x., Ren, K.-f., Zhao, Y.-x., Liu, X.-s., Chang, G.-x., and Ji, J., 2013. Construction of redox-ative multilayer film for electrochemically controlled release. *Langmuir*. **29**(35): p. 11163-11168.

48. Pyo, M. and Reynolds, J.R., 1996. Electrochemically stimulated adenosine 5'-triphosphate (ATP) release through redox switching of conducting polypyrrole films and bilayers. *Chemistry of Materials*. **8**(1): p. 128-133.

49. Svirskis, D., Wright, B.E., Travas-Sejdic, J., Rodgers, A., and Garg, S., 2010. Evaluation of physical properties and performance over time of an actuating polypyrrole based drug delivery system. *Sensors and Actuators B: Chemical*. **151**(1): p. 97-102.

50. Miller, L.L. and Zhou, X.Q., 1987. Poly (N-methylpyrrolylium) poly (styrenesulfonate)-a conductive, electrically switchable cation exchanger that cathodically binds and anodically releases dopamine. *Macromolecules*. **20**(7): p. 1594-1597.

51. Sharma, M., Waterhouse, G.I.N., Loader, S.W.C., Garg, S., and Svirskis, D., 2013. High surface area polypyrrole scaffolds for tunable drug delivery. *International journal of pharmaceutics*. **443**(1): p. 163-168.

52. Alizadeh, N. and Shamaeli, E., 2014. Electrochemically controlled release of anticancer drug methotrexate using nanostructured polypyrrole modified with cetylpyridinium: Release kinetics investigation. *Electrochimica Acta*. **130**: p. 488-496.

53. Deinhammer, R.S., Porter, M.D., and Shimazu, K., 1995. Retention characteristics of polypyrrole as a stationary phase for the electrochemically modulated liquid chromatographic (EMLC) separations of dansyl amino acids. *Journal of Electroanalytical Chemistry*. **387**(1): p. 35-46.

54. Teasdale, P. and Wallace, G., 1994. Characterising the chemical interactions that occur on polyaniline with inverse thin layer chromatography. *Polymer international*. **35**(2): p. 197-205.

55. Bossi, A., Piletsky, S.A., Turner, A.P., and Righetti, P.G., 2002. Repartition effect of aromatic polyaniline coatings on the separation of bioactive peptides in capillary electrophoresis. *Electrophoresis*. **23**(2): p. 203-208.

56. Robb, C.S., Yang, S.C., and Brown, P.R., 2002. Enhanced analysis of purine and pyrimidine bases by the use of double-strand polyaniline coatings in micellar electrokinetic capillary chromatography. *Electrophoresis*. **23**(12): p. 1900-1905.

57. Power, A., White, B., and Morrin, A., 2013. Microfluidic Thin-layer Flow Cell for Conducting Polymer Growth and Electroanalysis. *Electrochimica Acta*. **104**: p. 236-241.

58. Gorey, B., White, B., Smyth, M., and Morrin, A., 2014. Fabrication of homogenous three dimensionally ordered conducting polymer-polystyrene opal structures in microfluidic channels. *Journal of Materials Chemistry C*: p. DOI:10.1039/C1034TC00402G.

59. Gorey, B., Galineau, J., White, B., Smyth, M.R., and Morrin, A., 2012. Inverse-opal conducting polymer monoliths in microfluidic channels. *Electroanalysis*. **24**(6): p. 1318-1323.

60. Kaner, R.B., 2001. Gas, liquid and enantiomeric separations using polyaniline. *Synthetic Metals*. **125**(1): p. 65-71.

61. Chang, M.J., Liao, Y.H., Myerson, A.S., and Kwei, T., 1996. Gas transport properties of polyaniline membranes. *Journal of applied polymer science*. **62**(9): p. 1427-1436.

62. Anderson, M.R., Mattes, B.R., Reiss, H., and Kaner, R.B., 1991. Conjugated polymer films for gas separations. *Science*. **252**(5011): p. 1412-1415.

63. Illing, G., Hellgardt, K., Schonert, M., Wakeman, R., and Jungbauer, A., 2005. Towards ultrathin polyaniline films for gas separation. *Journal of Membrane Science*. **253**(1): p. 199-208.

64. Anderson, M.R., Kaner, R.B., Mattes, B.R., and Reiss, H., *Membranes having selective permeability*, 1994, Google Patents.

65. Alam, J., Dass, L.A., Alhoshan, M.S., and Mohammad, A.W., 2013. Advances in membrane development based on electrically conducting polymers. *Advances in Polymer Technology*. **32**(S1): p. E189-E197.

66. Sairam, M., Nataraj, S., Aminabhavi, T.M., Roy, S., and Madhusoodana, C., 2006. Polyaniline membranes for separation and purification of gases, liquids, and electrolyte solutions. *Separation & Purification Reviews*. **35**(4): p. 249-283.

67. Illing, G., Hellgardt, K., Wakeman, R., and Jungbauer, A., 2001. Preparation and characterisation of polyaniline based membranes for gas separation. *Journal of Membrane Science*. **184**(1): p. 69-78.

68. Pellegrino, J., 2003. The use of conducting polymers in membrane-based separations. *Annals of the New York Academy of Sciences*. **984**(1): p. 289-305.

69. Gupta, Y., Hellgardt, K., and Wakeman, R., 2006. Enhanced permeability of polyaniline based nano-membranes for gas separation. *Journal of Membrane Science*. **282**(1): p. 60-70.

70. Hasbullah, H., Kumbharkar, S., Ismail, A., and Li, K., 2011. Preparation of polyaniline asymmetric hollow fiber membranes and investigation towards gas separation performance. *Journal of Membrane Science*. **366**(1): p. 116-124.

71. Blinova, N. and Svec, F., 2014. Functionalized high performance polymer membranes for separation of carbon dioxide and methane. *Journal of Materials Chemistry A*. **2**(3): p. 600-604.

72. Liang, W. and Martin, C.R., 1991. Gas transport in electronically conductive polymers. *Chemistry of Materials*. **3**(3): p. 390-391.

73. Parthasarathy, R.V., Menon, V.P., and Martin, C.R., 1997. Unusual gas-transport selectivity in a partially oxidized form of the conductive polymer polypyrrole. *Chemistry of Materials*. **9**(2): p. 560-566.

74. Andreeva, D., Pientka, Z., Brozová, L., Bleha, M., Polotskaya, G., and Elyashevich, G., 2002. Effect of polymerization conditions of pyrrole on formation, structure and properties of high gas separation thin polypyrrole films. *Thin solid films*. **406**(1): p. 54-63.

75. Gulsen, D., Hacarloglu, P., Toppare, L., and Yilmaz, L., 2001. Effect of preparation parameters on the performance of conductive composite gas separation membranes. *Journal of Membrane Science*. **182**(1): p. 29-39.

76. Hasbullah, H., Kumbharkar, S., Ismail, A., and Li, K., 2012. Asymmetric hollow fibre membranes based on ring-substituted polyaniline and investigation towards its gas transport properties. *Journal of Membrane Science*. **397-398**: p. 38-50.

77. Guillen, G.R., Farrell, T.P., Kaner, R.B., and Hoek, E.M.V., 2010. Pore-structure, hydrophilicity, and particle filtration characteristics of polyaniline–polysulfone ultrafiltration membranes. *Journal of Materials Chemistry*. **20**(22): p. 4621-4628.

78. Zhao, S., Wang, Z., Wei, X., Zhao, B., Wang, J., Yang, S., and Wang, S., 2011. Performance improvement of polysulfone ultrafiltration membrane using PANi EB as both pore forming agent and hydrophilic modifier. *Journal of Membrane Science*. **385-386**(251-262).

79. Madaeni, S.S. and Molaeipour, S., 2010. Investigation of filtration capability of conductive composite membrane in separation of protein from water. *Ionics*. **16**(1): p. 75-80.

80. Fan, Z., Wang, Z., Duan, M., Wang, J., and Wang, S., 2008. Preparation and characterization of polyaniline/polysulfone nanocomposite ultrafiltration membrane. *Journal of Membrane Science*. **310**(1): p. 402-408.

81. Madaeni, S., 2006. Preparation and properties of composite membranes composed of non-conductive membranes and polypyrrole. *Indian journal of chemical technology*. **13**(1): p. 65-70.

82. Arthur, C.L. and Pawliszyn, J., 1990. Solid phase microextraction with thermal desorption using fused silica optical fibers. *Analytical Chemistry*. **62**(19): p. 2145-2148.

83. Liu, X., Wang, X., Tan, F., Zhao, H., Quan, X., Chen, J., and Li, L., 2012. An electrochemically enhanced solid-phase microextraction approach based on molecularly imprinted polypyrrole/multi-walled carbon nanotubes composite coating for selective extraction of fluoroquinolones in aqueous samples. *Analytica Chimica Acta*. **727**: p. 26-33.

84. Collins, C.J. and Arrigan, D.W.M., 2009. A review of recent advances in electrochemically modulated extraction methods. *Analytical and Bioanalytical Chemistry*. **393**(3): p. 835-845.

85. Du, W., Zhao, F., and Zeng, B., 2009. Novel multiwalled carbon nanotubes-polyaniline composite film coated platinum wire for headspace solid-phase microextraction and gas chromatographic determination of phenolic compounds. *Journal of Chromatography A*. **1216**(18): p. 3751-3757.

86. Wu, J. and Pawliszyn, J., 2001. Preparation and applications of polypyrrole films in solid-phase microextraction. *Journal of Chromatography A*. **909**(1): p. 37-52.

87. Ameli, A. and Alizadeh, N., 2011. Nanostructured conducting molecularly imprinted polymer for selective extraction of salicylate from urine and serum samples by electrochemically controlled solid-phase micro-extraction. *Analytica Chimica Acta*. **707**(1-2): p. 62-68.

88. Sahin, Y., Ercan, B., and Sahin, M., 2008. In situ electrochemical solid-phase extraction of anions and cations using polypyrrole and overoxidized sulfonated polypyrrole. *Talanta*. **75**(2): p. 369-375.

89. Perez-Gonzalez, V.H., Ho, V., Kulinsky, L., Madou, M., and Martinez-Chapa, S.O., 2013. PPyDEP: a new approach to microparticle manipulation employing polymer-based electrodes. *Lab on a Chip*. **13**(23): p. 4642-4652.

90. Ben-Yoav, H., Ofek Almog, R., Sverdlov, Y., Sternheim, M., Belkin, S., Freeman, A., and Shacham-Diamand, Y., 2012. Modified working electrodes for electrochemical whole-cell microchips. *Electrochimica Acta*. **82**: p. 109-114.

91. Henderson, R.D., Guijt, R.M., Andrewartha, L., Lewis, T.W., Rodemann, T., Henderson, A., Hilder, E.F., Haddad, P.R., and Breadmore, M.C., 2012. Lab-on-a-chip device with laser-patterned polymer electrodes for high voltage application and contactless conductivity detection. *Chemical Communications*. **48**(74): p. 9287-9289.

92. Henderson, R.D., Guijt, R.M., Haddad, P.R., Hilder, E.F., Lewis, T.W., and Breadmore, M.C., 2010. Manufacturing and application of a fully polymeric electrophoresis chip with integrated polyaniline electrodes. *Lab on a Chip*. **10**(14): p. 1869-1872.

93. Wang, J., Bunimovich, Y.L., Sui, G., Savvas, S., Wang, J., Guo, Y., Heath, J.R., and Tseng, H.-R., 2006. Electrochemical fabrication of conducting polymer nanowires in an integrated microfluidic system. *Chemical Communications,*(29): p. 3075-3077.

94. Florea, L., Diamond, D., and Benito-Lopez, F., 2013. Polyaniline coated micro-capillaries for continuous flow analysis of aqueous solutions. *Analytica Chimica Acta*. **759**: p. 1-7.

95. Ambrosi, A., Morrin, A., Smyth, M.R., and Killard, A.J., 2008. The application of conducting polymer nanoparticle electrodes to the sensing of ascorbic acid. *Analytica Chimica Acta*. **609**(1): p. 37-43.

96. Ge, D., Tian, X., Qi, R., Huang, S., Mu, J., Hong, S., Ye, S., Zhang, X., Li, D., and Shi, W., 2009. A polypyrrole-based microchip for controlled drug release. *Electrochimica Acta*. **55**(1): p. 271-275.

97. Beesabathuni, S., Stockham, J., Kim, J., Lee, H., Chung, J., and Shen, A., 2013. Fabrication of conducting polyaniline microspheres using droplet microfluidics. *RSC Advances*. **3**(46): p. 24423-24429.

98. Causley, J., Stitzel, S., Brady, S., Diamond, D., and Wallace, G., 2005. Electrochemically-induced fluid movement using polypyrrole. *Synthetic Metals*. **151**(1): p. 60-64.

99. Kim, J.H., Lau, K.T., Shepherd, R., Wu, Y., Wallace, G., and Diamond, D., 2008. Performance characteristics of a polypyrrole modified polydimethylsiloxane (PDMS) membrane based microfluidic pump. *Sensors and Actuators A: Physical*. **148**(1): p. 239-244.

100. Goodhew, P.J., Humphreys, J., and Beanland, R., *Electron microscopy and analysis*. 2000: CRC Press.

101. Reimer, L., *Scanning Electron Microscopy: Physics of Image Formation and Microanalysis: Ludwig Reimer*. 1985: Springer.

102. Andrade, C., Oliveira, M.D., Faulin, T., Hering, V., and Abdalla, D.S.P., 2011. Biosensors for detection of Low-Density Lipoprotein and its modified forms. *Intechopen*: p. 216-240.

103. Brett, C.M. and Brett, A.M.O., *Electrochemistry: principles, methods, and applications*. Vol. 4. 1993: Oxford university press Oxford.

104. Bard, A.J. and Faulkner, L.R., *Electrochemical methods: fundamentals and applications*. Vol. 2. 1980: Wiley New York.

105. Montenegro, M.I., Montenegro, I., Queirós, M.A., and Daschbach, J.L., *Microelectrodes: Theory and Applications: Theory and Applications*. Vol. 197. 1991: Springer.

106. Zhang, N., Li, J., Li, W., Ni, D., and Sun, K., 2012. High performance three-dimensionally ordered macroporous composite cathodes for intermediate temperature solid oxide fuels cells. *RSC Advances*. **2**(3): p. 802-804.

107. An, Y., Skinner, S.J., and McComb, D.W., 2009. Template assisted fabrication of macroporous thin films for solid oxide fuel cells. *Journal of Material Chemistry*. **20**(2): p. 248-254.

108. An, K., Alayoglu, S., Ewers, T., and Somorjai, G.A., 2011. Colloid chemistry of nanocatalysts: A molecular view. *Journal of Colloidal and Interface Science*. **373**(1): p. 1-13.

109. Cao, L., Shi, Y., Geng, J., and Yang, D., 2011. Fabrication of silica monolithic columns with ordered meso/macropore structure. *Materials Chemistry and Physics*. **130**(3): p. 1280-1286.

110. Innocenzi, P., Malfatti, L., and Soler-Illia, G.J.A.A., 2011. Hierarchical mesoporous films: From self-assembly to porosity with different length scales. *Chemistry of Materials*. **23**(10): p. 2501-2509.

111. Yang, Y. and Wang, C., 2009. Hierarchical construction of self-assembled low-dimensional molecular architectures observed by using scanning tunneling microscopy. *Chemistry Society Reviews*. **38**(9): p. 2576-2589.

112. Du, X. and He, J., 2011. Spherical silica micro/nanomaterials with hierarchical structures: Synthesis and applications. *Nanoscale*. **3**(10): p. 3984-4002.

113. Von Freymann, G., Kitaev, V., Lotsch, B.V., and Ozin, G.A., 2013. Bottom-up assembly of photonic crystals *Chemistry Society Reviews*. **42**(7): p. 2528-2554.

114. Stein, A., Li, F., and Denny, N.R., 2007. Morphological control in colloidal crystal templating of inverse opals, hierarchical structures, and shaped particles. *Chemistry of Materials*. **20**(3): p. 649-666.

115. Gorey, B., Galineau, J., White, B., Smyth, M.R., and Morrin, A., 2012. Inverse-opal conducting polymer monoliths in microfluidic channels. *Electroanalysis*. **24**(6): p. 1318-1323.

116. Wuhong, X., Jiupeng, Z., Yanbo, D., and Yao, L., 2011. Fabrication of 3-dimensionally ordered macroporous Ta_2O_5 films through aqueous organic gel process. *Applied Surface Science*. **257**(24): p. 10725-10728.

117. Yao, L., Wuhong, X., Jiupeng, Z., and Xiangdong, M., 2009. Fabrication and charaterisation of three-dimensionally ordered macroporous niobium oxide. *Solid State Sciences*. **11**(9): p. 1625-1630.

118. Zhao, B. and Collinson, M.M., 2012. Hollow silica capsules with well-defined asymmetric windows in the shell. *Langmuir*. **28**(19): p. 7492-7497.

119. Zhao, B. and Collinson, M.M., 2010. Well-defined hierarchical templates for multimodal porous material fabrication. *Chemistry of Materials*. **22**(14): p. 4312-4319.

120. Yan, Y. and Chen, Q., 2009. Rapid synthesis of monodispersed polystyrene microspheres and self-assembly of colloidal crystal on mica. *Journal of Dispersion Science and Technology*. **30**(4): p. 575-580.

121. Li, F., Wilker, M.B., and Stein, A., 2012. Simulation-aided design and synthesis of hierarchically porous membranes. *Langmuir*. **28**(19): p. 7484-7491.

122. Dhainaut, J., Dacquin, J.P., Lee, A.F., and Wilson, K., 2010. Hierarchical macroporous-mesoporous SBA-15 sulfonic acid catalysts for biodiesel synthesis. *Green Chemistry*. **12**(2): p. 296-303.

123. Dacquin, J.P., Dhainaut, J., Duprez, D., Royer, S., Lee, A.F., and Wilson, K., 2009. An efficient route to highly organized, tunable macroporous-mesoporous alumina. *Journal of the American Chemical Society*. **131**(36): p. 12896 - 12897.

124. Ganai, A.K., Kumari, S., Sharma, K.P., Panda, C., Kumaraswamy, G., and Gupta, S.S., 2012. Synthesis of functional hybrid silica scaffolds with controllable hierarchial porosity by dyanmic templating. *Chemical Communications*. **48**(43): p. 5292-5294.

125. Yuan, Z.Y. and Su, B.L., 2006. Insights into hierarchically meso-macroporous structured materials. *Journal of Material Chemistry*. **16**(7): p. 663-677.

126. Emoto, A., Uchida, E., and Fukuda, T., 2012. Fabrication and optical properties of binary colloidal crystal monolayers consisting of mirco- and nano-polystyrene spheres. *Colloid and Surfaces A: Physicochemical and Engineering Aspects*. **396**: p. 189-194.

127. Cai, Z., Teng, J., Wan, Y., and Zhao, X.S., 2012. An improved convective self-assembly method for the fabrication of binary colloidal crystals and inverse structures. *Journal of Colloidal Interferface Science*. **380**(1): p. 42-50.

128. Yang, L., Wang, J., Zhang, Y., Luo, Y., Li, D., and Meng, Q., 2012. In situ optical microspectroscopy monitoring of binary colloidal crsytal growth dynamics via evaporation-induced cooperative self-assembly. *Langmuir*. **28**(9): p. 4160-4167.

129. Wang, J., Ahl, S., Li, Q., Kreiter, M., Neumann, T., Burkert, K., Knoll, W., and Jonas, U., 2008. Structural and optical characterization of 3-dimensional binary colloidal crystal and inverse opal films perpared by direct co-deposition. *Journal of Material Chemistry*. **18**(9): p. 981-988.

130. Wang, Z., Liu, S., Wu, P., and Cai, C., 2009. Detection of glucose based on direct electron transfer reaction of glucose oxidase immobilized on highly ordered polyaniline nanotubes. *Analytical Chemistry*. **81**(4): p. 1638-1645.

131. Kuroda, Y., Sakamoto, Y., and Kuroda, K., 2012. Selective cleavage of periodic mesoscale structures: Two-dimensional replication of binary colloidal crystals into dimpled gold nanoplates. *Journal of the American Chemical Society*. **134**(20): p. 8684-8692.

132. Yu, J., Yan, Q., and Shen, D., 2010. Co-self-assembly of binary colloidal crystals at the air-water interface. *ACS Applied Materials and Interfaces*. **2**(9): p. 1922-1926.

133. Kitaev, V. and Ozin, G.A., 2003. Self-assembled surface patterns of binary colloidal crystals. *Advanced Materials*. **15**(1): p. 75-78.

134. Singh, G., Pillai, S., Arpanaei, A., and Kingshott, P., 2011. Electrostatic and capillary force directed tunable 3-dimensional binary micro- and nanoparticle assemblies on surfaces. *Nanotechnology*. **22**: p. 225601-225609.

135. Dai, Z., Li, Y., Duan, G., Jia, L., and Cai, W., 2012. Phase diagram, design of monolayer binary colloidal crystals, and their fabrication based on ethanol-

assisted self-assembly at the air/water interface. *ACS Nano*. **6**(8): p. 6706-6716.

136. Vogel, N., de Viguerie, L., Jonas, U., Weiss, C.K., and Landfester, K., 2011. Wafer-scale fabrication of ordered binary colloidal monolayers with adjustable stoichiometries. *Advanced Functional Materials*. **21**(16): p. 3064-3073.

137. Deegan, R.D., Bakajin, O., Dupont, T.F., Huber, G., Nagel, S.R., and Witten, T.A., 1997. Capillary flow as the cause of ring stains from dried liquid drops. *Nature*. **389**: p. 827-829.

138. Nair, R.V. and Vijaya, R., 2008. Structural and optical characterization of photonic crystals synthesized using the inward growing self-assembling method. *Applied Physics A*. **90**(3): p. 559-563.

139. Yan, Q., Zhou, Z., and Zhao, X., 2005. Inward-growing self-assembly of colloidal crystal films on horizontal substrates. *Langmuir*. **21**(7): p. 3158-3164.

140. Xu, X., Ma, L., Huang, D., Luo, J., and Guo, D., 2014. Linear growth of colloidal rings at the edge of drying droplets. *Colloids and Surfaces A: Physicochemical and Engineering Aspects*. **447**: p. 28-31.

141. Deegan, R.D., Bakajin, O., Dupont, T.F., Huber, G., Nagel, S.R., and Witten, T.A., 1997. Capillary flow as the cause of ring stains from dried liquid drops. *Nature*. **389**(6653): p. 827-829.

142. Liu, Z., Ya, J., Xin, Y., Ma, J., and Zhou, C., 2006. Assembly of polystyrene colloidal crystal templates by a dip-drawing method. *Journal of crystal growth*. **297**(1): p. 223-227.

143. Fu, Y., Jin, Z., Liu, Z., Liu, Y., and Li, W., 2008. Self-assembly of colloidal crystals from polystyrene emulsion at elevated temperature by dip-drawing method. *Materials Letters*. **62**(27): p. 4286-4289.

144. Ko, Y.G. and Shin, D.H., 2007. Effects of liquid bridge between colloidal spheres and evaporation temperature on fabrication of colloidal multilayers. *The Journal of Physical Chemistry B*. **111**(7): p. 1545-1551.

145. Fu, Y., Jin, Z., Liu, Z., and Li, W., 2007. Preparation of ordered porous SnO_2 films by dip-drawing method with PS colloid crystal templates. *Journal of the European Ceramic Society*. **27**(5): p. 2223-2228.

146. Shieh, J.-Y., Kuo, J.-Y., Weng, H.-P., and Yu, H.H., 2013. Preparation and Evaluation of the Bioinspired PS/PDMS Photochromic Films by the Self-Assembly Dip–Drawing Method. *Langmuir*. **29**(2): p. 667-672.

147. Chen, J., Dong, P., Di, D., Wang, C., Wang, H., Wang, J., and Wu, X., 2013. Controllable fabrication of 2D colloidal-crystal films with polystyrene nanospheres of various diameters by spin-coating. *Applied Surface Science*. **270**: p. 6-15.

148. Wang, D. and Möhwald, H., 2004. Rapid Fabrication of Binary Colloidal Crystals by Stepwise Spin-Coating. *Advanced Materials*. **16**(3): p. 244-247.

149. Arcos, C., Kumar, K., González-Viñas, W., Sirera, R., Poduska, K.M., and Yethiraj, A., 2008. Orientationally correlated colloidal polycrystals without long-range positional order. *Physical Review E*. **77**(5): p. 050402-050401 - 050402-050404.

150. Jiang, P., Prasad, T., McFarland, M.J., and Colvin, V.L., 2006. Two-dimensional nonclose-packed colloidal crystals formed by spincoating. *Applied Physics Letters*. **89**(1): p. 011908.

151. Gu, Z.-Z., Wang, D., and Möhwald, H., 2006. Self-assembly of microspheres at the air/water/air interface into free-standing colloidal crystal films. *Soft Matter*. **3**(1): p. 68-70.

152. Im, S.H., Lim, Y.T., Suh, D.J., and Park, O.O., 2002. Three-Dimensional Self-Assembly of Colloids at a Water–Air Interface: A Novel Technique for the Fabrication of Photonic Bandgap Crystals. *Advanced Materials*. **14**(19): p. 1367-1369.

153. Retsch, M., Zhou, Z., Rivera, S., Kappl, M., Zhao, X.S., Jonas, U., and Li, Q., 2009. Fabrication of Large-Area, Transferable Colloidal Monolayers Utilizing Self-Assembly at the Air/Water Interface. *Macromolecular Chemistry and Physics*. **210**(3-4): p. 230-241.

154. Gates, B., Qin, D., and Xia, Y., 1999. Assembly of nanoparticles into opaline structures over large areas. *Advanced Materials*. **11**(6): p. 466-469.

155. Míguez, H., Yang, S.M., and Ozin, G.A., 2003. Optical properties of colloidal photonic crystals confined in rectangular microchannels. *Langmuir*. **19**(8): p. 3479-3485.

156. von Freymann, G., Kitaev, V., Lotsch, B.V., and Ozin, G.A., 2013. Bottom-up assembly of photonic crystals. *Chemical Society Reviews*. **42**(7): p. 2528-2554.

157. Zhou, C., Han, J., and Guo, R., 2013. A facile strategy to colloidal crystals by drying condensed suspension droplets. *Journal of Colloidal and Interface Science*. **397**: p. 80-87.

158. Cong, H. and Cao, W., 2003. Colloidal crystallization induced by capillary force. *Langmuir*. **19**(20): p. 8177-8181.

159. Nagayama, K., 1996. Two-dimensional self-assembly of colloids in thin liquid films. *Colloid Surfaces A: Physiochemical and Engineering*. **109**: p. 363-374.

160. Cai, Z., Teng, J., Xiong, Z., Li, Y., Li, Q., Lu, X., and Zhao, X.S., 2011. Fabrication of TiO_2 binary inverse opals without overlayers via the aandwich-vacuum infiltration of precursor. *Langmuir*. **27**(8): p. 5157-5164.

161. Kim, M.H., Im, S.H., and Park, O.O., 2005. Fabrication and structural analysis of binary colloidal crystals with two-dimensional superlattices. *Advanced Materials*. **17**(20): p. 2501-2505.

162. Dai, Z., Li, Y., Duan, G., Jia, L., and Cai, W., 2012. Phase diagram, design of monolayer binary colloidal crystals, and their fabrication based on ethanol-assisted self-assembly at the air/water interface. *ACS. nano.* **6**(8): p. 6706.

163. Zhang, J.T., Wang, L., Lamont, D.N., Velankar, S.S., and Asher, S.A., 2012. Fabrication of large-area two-dimensional colloidal crystals. *Angewandte Chemie International Edition*. **51**(25): p. 6117-6120.

164. Zhang, J.T., Wang, L., Chao, X., Velankar, S.S., and Asher, S.A., 2013. Vertical spreading of two-dimensional crystalline colloidal arrays. *Journal of Materials Chemistry, C*. **1**(38): p. 6099.

165. Liu, Y., Guan, Y., and Zhang, Y., 2014. Facile assembly of 3D binary colloidal crystals from soft microgel spheres. *Macromolecular Rapid Communications*. **35**(6): p. 630-634.

166. Wallace, G.G., Teasdale, P.R., Spinks, G.M., and Kane-Maguire, L.A., *Conductive electroactive polymers: intelligent polymer systems*. 2008: CRC press.

167. Gvozdenović, M.M., Jugović, B.Z., Stevanović, J.S., Trišović, T.L., and Grgur, B.N., *Electrochemical polymerization of aniline*. Electropolymerization, ed. E. Schab-Balcerzak. 2011: Intech. 77-96.

168. Zhao, S., Wu, M., Zhao, F., and Zeng, B., 2013. Electrochemical preparation of polyaniline–polypyrrole solid-phase microextraction coating and its application in the GC determination of several esters. *Talanta*. **117**: p. 146-151.

169. Zeng, J., Zhao, C., Chong, F., Cao, Y., Subhan, F., Wang, Q., Yu, J., Zhang, M., Luo, L., and Ren, W., 2013. Oriented ZnO nanorods grown on a porous polyaniline film as a novel coating for solid-phase microextraction. *Journal of Chromatography A*. **1319**: p. 21-26.

170. Pan, L., Qiu, H., Dou, C., Li, Y., Pu, L., Xu, J., and Shi, Y., 2010. Conducting polymer nanostructures: Template synthesis and applications in energy storage. *International Journal of Molecular Sciences*. **11**(7): p. 2636-2657.

171. Cosnier, S. and Holzinger, M., 2011. Electrosynthesized polymers for biosensing. *Chemical Society Reviews*. **40**(5): p. 2146-2156.

172. Luo, X., Vidal, G.D., Killard, A.J., Morrin, A., and Smyth, M.R., 2007. Nanocauliflowers: A nanostructured polyaniline-modified screen-printed electrode with a self-assembled polystyrene template and its application in an amperometric enzyme biosensor. *Electroanalysis*. **19**(7-8): p. 876-883.

173. Dhand, C., Sumana, G., Datta, M., and Malhotra, B.D., 2010. Electrophoretically deposited nano-structured polyaniline film for glucose sensing. *Thin solid films*. **519**(3): p. 1145-1150.

174. Dhand, C., Das, M., Datta, M., and Malhotra, B.D., 2011. Recent advances in polyaniline based biosensors. *Biosensors Bioelectronics*. **26**(6): p. 2811-2821.

175. Luo, X. and Cui, X.T., 2009. Sponge-like nanostructured conducting polymers for electrically controlled drug release. *Electrochemical Communications*. **11**(10): p. 1956-1959.

176. Sirivisoot, S., Pareta, R.A., and Webster, T.J., 2011. A conductive nanostructured polymer electrodeposited on titanium as a controllable, local drug delivery platform. *Journal of Biomedical Materials and Research Part A*. **99A**(4): p. 586-597.

177. Bartlett, P.N., Birkin, P.R., Ghanem, M.A., and Toh, C.-S., 2001. Electrochemical syntheses of highly ordered macroporous conducting polymers grown around self-assembled colloidal templates. *Journal of Material Chemistry*. **11**(3): p. 849-853.

178. Xu, L., Wang, J., Song, Y., and Jiang, L., 2008. Electrically tunable polypyrrole inverse opals with switchable stopband, conductivity, and wettability. *Chemistry of Materials*. **20**(11): p. 3554-3556.

179. Ge, D., Yang, L., Tong, Z., Ding, Y., Xin, W., Zhao, J., and Li, Y., 2013. Ion diffusion and optical switching performance of 3D ordered nanostructured polyaniline films for advanced electrochemical/electrochromic devices. *Electrochimica Acta*. **104**: p. 191-197.

180. Tian, S., Wang, J., Jonas, U., and Knoll, W., 2005. Inverse opals of polyaniline and its copolymers prepared by electrochemical techniques. *Chemistry of Materials*. **17**(23): p. 5726-5730.

181. Santos, L., Martin, P., Ghilane, J., Lacaze, P.C., and Lacroix, J.C., 2013. Micro/Nano-Structured Polypyrrole Surfaces on Oxidizable Metals as Smart

Electroswitchable Coatings. *ACS Applied Materials and Interfaces*. **5**(20): p. 10159-10164.

182. Chowdhury, A.D., Gangopadhyay, R., and De, A., 2014. Highly sensitive electrochemical biosensor for glucose, DNA and protein using gold-polyaniline nanocomposites as a common matrix. *Sensors and Actuators B: Chemical*. **190**: p. 348-356.

183. Wang, X., Liu, W., Li, C., Chu, C., Wang, S., Yan, M., Yu, J., and Huang, J., 2013. Synthesis of polyaniline using electrochemical polymerization and application in a sensitive DNA biosensor with [Ru (bpy) 3] 2+ functionalized nanoporous gold composite as label. *Monatshefte für Chemie-Chemical Monthly*. **144**(12): p. 1759-1765.

184. Xue, C., Wang, X., Zhu, W., Han, Q., Zhu, C., Hong, J., Zhou, X., and Jiang, H., 2014. Electrochemical serotonin sensing interface based on double-layered membrane of reduced graphene oxide/polyaniline nanocomposites and molecularly imprinted polymers embedded with gold nanoparticles. *Sensors and Actuators B: Chemical*. **196**: p. 57-63.

185. Wei, H., Zhu, J., Wu, S., Wei, S., and Guo, Z., 2013. Electrochromic polyaniline/graphite oxide nanocomposites with endured electrochemical energy storage. *Polymer*. **54**(7): p. 1820-1831.

186. Wei, H., Gu, H., Guo, J., Wei, S., and Guo, Z., 2013. Electropolymerized polyaniline nanocomposites from multi-walled carbon nanotubes with tuned surface functionalities for electrochemical energy storage. *Journal of The Electrochemical Society*. **160**(7): p. G3038-G3045.

187. Masoumi, V., Mohammadi, A., Amini, M., Khoshayand, M.R., and Dinarvand, R., 2014. Electrochemical synthesis and characterization of solid-

phase microextraction fibers using conductive polymers: application in extraction of benzaldehyde from aqueous solution. *Journal of Solid State Electrochemistry*. **18**(6): p. 1763-1771.

188. Sarafraz-Yazdi, A., Rounaghi, G., Razavipanah, I., Vatani, H., and Amiri, A., 2014. New polypyrrole–carbon nanotubes–silicon dioxide solid-phase microextraction fiber for the preconcentration and determination of benzene, toluene, ethylbenzene, and o-xylene using gas liquid chromatography. *Journal of separation science*. **37**(18): p. 2605-2612.

189. Sapurina, I.Y. and Shishov, M., 2012. Oxidative Polymerization of Aniline: Molecular Synthesis of Polyaniline and the Formation of Supramolecular Structures.

190. Adams, P., Laughlin, P., Monkman, A., and Kenwright, A., 1996. Low temperature synthesis of high molecular weight polyaniline. *Polymer*. **37**(15): p. 3411-3417.

191. Li, X., Liu, Y., Guo, W., Chen, J., He, W., and Peng, F., 2014. Synthesis of spherical PANI particles via chemical polymerization in ionic liquid for high-performance supercapacitors. *Electrochimica Acta*. **135**: p. 550-557.

192. Li, Y., Zhao, X., Xu, Q., Zhang, Q., and Chen, D., 2011. Facile preparation and enhanced capacitance of the polyaniline/sodium alginate nanofiber network for supercapacitors. *Langmuir*. **27**(10): p. 6458-6463.

193. Liu, M., He, S., Fan, W., Miao, Y.-E., and Liu, T., 2014. Filter paper-derived carbon fiber/polyaniline composite paper for high energy storage applications. *Composites Science and Technology*.

194. Surya Murali, R., Padaki, M., Matsuura, T., Abdullah, M., and Ismail, A., 2014. Polyaniline in-situ modified halloysite nanotubes incorporated

asymmetric mixed matrix membrane for gas separation. *Separation and Purification Technology*.

195. Ramkumar, J. and Chandramouleeswaran, S., 2013. Separation of uranyl ion using polyaniline. *Journal of Radioanalytical and Nuclear Chemistry*. **298**(3): p. 1543-1549.

196. Anu Prathap, M.U., Thakur, B., Sawant, S.N., and Srivastava, R., 2011. Synthesis of mesostructured polyaniline using mixed surfactants, anionic sodium dodecylsulfate and non-ionic polymers and their applications in H_2O_2 and glucose sensing. *Colloids and Surfaces, B: Biointerfaces*. **89**: p. 108-116.

197. Milakin, K., Korovin, A., Moroz, E., Levon, K., Guiseppi-Elie, A., and Sergeyev, V., 2013. Polyaniline-Based Sensor Material for Potentiometric Determination of Ascorbic Acid. *Electroanalysis*. **25**(5): p. 1323-1330.

198. Liu, C., Gao, G., Zhang, Y., Wang, L., Wang, J., and Song, Y., 2012. The Naked-Eye Detection of NH_3–HCl by Polyaniline-Infiltrated TiO_2 Inverse Opal Photonic Crystals. *Macromolecular Rapid Communications*. **33**(5): p. 380-385.

199. Pahovnik, D., Žagar, E., Kogej, K., Vohlídal, J., and Žigon, M., 2013. Polyaniline nanostructures prepared in acidic aqueous solutions of ionic liquids acting as soft templates. *European Polymer Journal*. **49**(6): p. 1381-1390.

200. Pirhady Tavandashti, N., Ghorbani, M., and Shojaei, A., 2014. The Morphology Transition Control of Polyaniline from Nanotubes to Nanospheres in a Soft Template Method. *Polymer international*.

201. Olad, A., Ilghami, F., and Nosrati, R., 2012. Surfactant-assisted synthesis of polyaniline nanofibres without shaking and stirring: effect of conditions on morphology and conductivity. *Chemical Papers*. **66**(8): p. 757-764.

202. Zhou, D., Li, Y., Wang, J., Xu, P., and Han, X., 2011. Synthesis of polyaniline nanofibers with high electrical conductivity from CTAB–SDBS mixed surfactants. *Materials Letters*. **65**(23): p. 3601-3604.

203. Yang, L.Y. and Liau, W.B., 2007. Chemical synthesis of polyaniline inverse opals by templating colloidal crystals in the presence of dodecylbenzenesulfonic acid. *Macromolecular Chemistry and Physics*. **208**(9): p. 994-1001.

204. Yang, L.Y. and Liau, W.B., 2010. Optical responses of polyaniline inverse opals to chemicals. *Synthetic Metals*. **160**(17): p. 1809-1814.

205. Yang, L.Y. and Liau, W.B., 2010. Environmental responses of polyaniline inverse opals: Application to gas sensing. *Synthetic Metals*. **160**(7): p. 609-614.

206. Choi, S.W., Zhang, Y., and Xia, Y., 2010. Three-dimensional scaffolds for tissue engineering: the importance of uniformity in pore size and structure. *Langmuir*. **26**(24): p. 19001-19006.

207. Zhang, Y.S., Choi, S.W., and Xia, Y., 2013. Inverse opal scaffolds for applications in regenerative medicine. *Soft Matter*. **9**(41): p. 9747-9754.

208. áO'Connor, N.E., 2013. Dynamic pH mapping in microfluidic devices by integrating adaptive coatings based on polyaniline with colorimetric imaging techniques. *Lab on a Chip*. **13**(6): p. 1079-1085.

209. Zhao, S., Wang, Z., Wang, J., and Wang, S., 2014. The effect of pH of coagulation bath on tailoring the morphology and separation performance of

polysulfone/polyaniline ultrafiltration membrane. *Journal of Membrane Science*.

210. Mandić, Z., Roković, M.K., and Pokupčić, T., 2009. Polyaniline as cathodic material for electrochemical energy sources: The role of morphology. *Electrochimica Acta*. **54**(10): p. 2941-2950.

211. Desilvestro, J. and Scheifele, W., 1993. Morphology of electrochemically prepared polyaniline. Influence of polymerization parameters. *Journal of Material Chemistry*. **3**(3): p. 263-272.

212. Bubnova, O., Khan, Z.U., Wang, H., Braun, S., Evans, D.R., Fabretto, M., Hojati-Talemi, P., Dagnelund, D., Arlin, J.-B., and Geerts, Y.H., 2014. Semi-metallic polymers. *Nature materials*. **13**(2): p. 190-194.

213. Qiu, Y., Lu, S., Wang, S., Zhang, X., He, S., and He, T., 2014. High-performance polyaniline counter electrode electropolymerized in presence of sodium dodecyl sulfate for dye-sensitized solar cells. *Journal of Power Sources*. **253**: p. 300-304.

214. Khalid, M., Tumelero, M.A., Brandt, I.S., Zoldan, V.C., Acuña, J.J., and Pasa, A.A., 2013. Electrical Conductivity Studies of Polyaniline Nanotubes Doped with Different Sulfonic Acids. *Indian Journal of Materials Science*. **2013**.

215. Zhang, Z., Wei, Z., and Wan, M., 2002. Nanostructures of polyaniline doped with inorganic acids. *Macromolecules*. **35**(15): p. 5937-5942.

216. Rana, U., Mondal, S., Sannigrahi, J., Sukul, P.K., Amin, M.A., Majumdar, S., and Malik, S., 2014. Aromatic bi-, tri-and tetracarboxylic acid doped polyaniline nanotubes: effect on morphologies and electrical transport properties. *Journal of Materials Chemistry C*. **2**(17): p. 3382-3389.

217. Fan, H., Wang, H., Guo, J., Zhao, N., and Xu, J., 2014. SDBS-assisted preparation of novel polyaniline planar-structure: Morphology, mechanism and hydrophobicity. *Journal of colloid and interface science*. **414**: p. 46-49.

218. Geethalakshmi, D., Muthukumarasamy, N., and Balasundaraprabhu, R., 2014. Effect of dopant concentration on the properties of HCl-doped PANI thin films prepared at different temperatures. *Optik-International Journal for Light and Electron Optics*. **125**(3): p. 1307-1310.

219. Tohumcu, C., Taş, R., and Can, M., 2014. Increasing the crystallite and conductivity of polypyrrole with dopant used. *Ionics*: p. 1-6.

220. Leng, W., Zhou, S., Gu, G., and Wu, L., 2012. Wettability switching of SDS-doped polyaniline from hydrophobic to hydrophilic induced by alkaline/reduction reactions. *Journal of colloid and interface science*. **369**(1): p. 411-418.

221. Zhu, Y., Li, J., He, H., Wan, M., and Jiang, L., 2007. Reversible wettability switching of polyaniline-coated fabric, triggered by ammonia gas. *Macromolecular Rapid Communications*. **28**(23): p. 2230-2236.

222. Isaksson, J., Tengstedt, C., Fahlman, M., Robinson, N., and Berggren, M., 2004. A solid-state organic electronic wettability switch. *Advanced Materials*. **16**(4): p. 316-320.

223. Xu, L., Chen, W., Mulchandani, A., and Yan, Y., 2005. Reversible conversion of conducting polymer films from superhydrophobic to superhydrophilic. *Angewandte Chemie International Edition*. **44**(37): p. 6009-6012.

224. Sun, J. and Bi, H., 2012. Facile fabrication of superhydrophobic flower-like polyaniline architectures by using valine as a dopant in polymerization. *Applied Surface Science*. **258**(10): p. 4276-4282.

225. Zhu, Y., Li, J., Wan, M., and Jiang, L., 2008. 3D-boxlike polyaniline microstructures with super-hydrophobic and high-crystalline properties. *Polymer*. **49**(16): p. 3419-3423.

226. Zhu, Y., Hu, D., Wan, M., Jiang, L., and Wei, Y., 2007. Conducting and superhydrophobic rambutan-like hollow spheres of polyaniline. *Advanced Materials*. **19**(16): p. 2092-2096.

227. Madaeni, S.S., 2006. Preparation and properties of composite membranes composed of non-conductive membranes and polypyrrole. *Indian journal of chemical technology*. **13**(1): p. 65-70.

228. Peng, C.-W., Chang, K.-C., Weng, C.-J., Lai, M.-C., Hsu, C.-H., Hsu, S.-C., Hsu, Y.-Y., Hung, W.-I., Wei, Y., and Yeh, J.-M., 2013. Nano-casting technique to prepare polyaniline surface with biomimetic superhydrophobic structures for anticorrosion application. *Electrochimica Acta*. **95**: p. 192-199.

229. Deshpande, P.P., Jadhav, N.G., Gelling, V.J., and Sazou, D., 2014. Conducting polymers for corrosion protection: a review. *Journal of Coatings Technology and Research*. **11**(4): p. 473-494.

230. Kiefer, R., Temmer, R., Tamm, T., Travas-Sejdic, J., Kilmartin, P.A., and Aabloo, A., 2013. Conducting polymer actuators formed on MWCNT and PEDOT-PSS conductive coatings. *Synthetic Metals*. **171**: p. 69-75.

231. Xu, W., Tian, Y., Bisaria, H., Ahn, P., Choi, C.-H., and Yang, E.-H. *Transportation of a liquid droplet at ultra-low voltages by tunable wetting on conjugated polymer electrodes*. in *Solid-State Sensors, Actuators and*

Microsystems (TRANSDUCERS & EUROSENSORS XXVII), 2013 Transducers & Eurosensors XXVII: The 17th International Conference on. 2013. IEEE.

232. Darmanin, T. and Guittard, F., 2014. Wettability of conducting polymers: From superhydrophilicity to superoleophobicity. *Progress in Polymer Science*. **39**(4): p. 656-682.

233. Zhou, C., Han, J., and Guo, R., 2009. Synthesis of polyaniline hierarchical structures in a dilute SDS/HCl solution: nanostructure-covered rectangular tubes. *Macromolecules*. **42**(4): p. 1252-1257.

234. Mihi, A., Zhang, C., and Braun, P.V., 2011. Transfer of preformed three-dimensional photonic crystals onto dye-sensitized solar cells. *Angewandte Chemie*. **123**(25): p. 5830-5833.

235. Stein, A., Wilson, B.E., and Rudisill, S.G., 2013. Design and functionality of colloidal-crystal-templated materials-chemical applications of inverse opals. *Chemical Society Reviews*. **42**(7): p. 2763-2803.

236. Fang, B., Bonakdarpour, A., Kim, M.-S., Kim, J.H., Wilkinson, D.P., and Yu, J.-S., 2013. Multimodal porous carbon as a highly efficient electrode material in an electric double layer capacitor. *Microporous and Mesoporous Materials*. **182**: p. 1-7.

237. Fang, B., Bonakdarpour, A., Xing, Y., Yu, J.-S., and Wilkinson, D.P., 2014. Hierarchical nanostructured carbon materials for ultrahigh electrochemical energy storage. *ECS Transactions*. **58**(27): p. 13-19.

238. Qiu, S., Yin, H., Zheng, J., Jiang, B., Wu, M., and Wu, W., 2014. A biomimetic 3D ordered multimodal porous carbon with hydrophobicity for

oil-water separation. *Materials Letters*: p. DOI: 10.1016/j.matlet.2014.1006.1096.

239. Liu, X., Wang, X., Tan, F., Zhao, H., Quan, X., Chen, J., and Li, L., 2012. An electrochemically enhanced solid-phase microextraction approach based on molecularly imprinted polypyrrole/multi-walled carbon nanotubes composite coating for selective extraction of fluoroquinolones in aqueous samples. *Analytica Chimica Acta*.